

IN-35
48302
R 109

Liquid Crystal Point Diffraction Interferometer

Carolyn R. Mercer
Lewis Research Center
Cleveland, Ohio

May 1995



National Aeronautics and
Space Administration

(NASA-TM-106899) LIQUID CRYSTAL
POINT DIFFRACTION INTERFEROMETER
Ph.D. Thesis - Arizona Univ., 1995
(NASA- Lewis Research Center)
109 p

N95-26073
Unclassified

63/35 0048302

LIQUID CRYSTAL POINT DIFFRACTION INTERFEROMETER

by

Carolyn Regan Mercer

**A Dissertation Submitted to the Faculty of the
Committee on OPTICAL SCIENCES (GRADUATE)**

**In Partial Fulfillment of the Requirements
For the Degree of**

DOCTOR OF PHILOSOPHY

In the Graduate College

THE UNIVERSITY OF ARIZONA

LIQUID CRYSTAL POINT DIFFRACTION INTERFEROMETER

Carolyn Regan Mercer

A new instrument, the liquid crystal point diffraction interferometer (LCPDI), has been developed for the measurement of phase objects. This instrument maintains the compact, robust design of Linnik's point diffraction interferometer (PDI) and adds to it phase stepping capability for quantitative interferogram analysis. The result is a compact, simple to align, environmentally insensitive interferometer capable of accurately measuring optical wavefronts with very high data density and with automated data reduction.

This dissertation describes the theory of both the PDI and liquid crystal phase control. The design considerations for the LCPDI are presented, including manufacturing considerations. The operation and performance of the LCPDI are discussed, including sections regarding alignment, calibration, and amplitude modulation effects. The LCPDI is then demonstrated using two phase objects: a defocus difference wavefront, and a temperature distribution across a heated chamber filled with silicone oil. The measured results are compared to theoretical or independently measured results and show excellent agreement.

A computer simulation of the LCPDI was performed to verify the source of observed periodic phase measurement error. The error stems from intensity variations caused by dye molecules rotating within the liquid crystal layer. Methods are discussed for reducing this error. Algorithms are presented which reduce this error; they are also useful for any phase-stepping interferometer that has unwanted intensity fluctuations, such as those caused by unregulated lasers.

It is expected that this instrument will have application in the fluid sciences as a diagnostic tool, particularly in space based applications where autonomy, robustness, and compactness are desirable qualities. It should also be useful for the testing of optical elements, provided a master is available for comparison.

PRECEDING PAGE BLANK NOT FILMED

TABLE OF CONTENTS

1. LIST OF TABLES	6
2. LIST OF FIGURES.....	7
3. ABSTRACT	9
4. INTRODUCTION.....	11
4.1 Point Diffraction Interferometer	12
4.1.1 Description	12
4.1.2 Applications.....	14
4.1.2.1 Optical Testing.....	14
4.1.2.2 Flow Metrology	14
4.1.3 Interferogram analysis.....	15
4.2 Evolution of the PDI	17
4.3 Liquid crystal PDI	21
5. THEORY	22
5.1 Principle of the LCPDI.....	22
5.1.1 Ray Model.....	22
5.1.2 Wave Model	25
5.2 Principle of liquid crystal phase control.....	35
5.3 Phase calculation.....	42
5.3.1 Assumption violations.....	42
5.3.2 Algorithm modification.....	44
6. LCPDI DESIGN	45
6.1 Design parameters.....	47
6.1.1 Phase control.....	48
6.1.2 Amplitude control.....	48
6.2 Circuit design.....	49
6.3 System design	50
7. PHYSICAL DESCRIPTION.....	54
7.1 Materials.....	54
7.2 Dimensions	54
7.3 Optics	55
7.4 Electronics	55
7.5 Operation	56
7.5.1 Alignment.....	56
7.5.2 Phase stepping calibration.....	56
7.5.3 Object beam intensity determination.....	58
8. PERFORMANCE	60
8.1 Phase and Amplitude Modulation	60
8.2 Accuracy.....	63
8.2.1 Focus shift measurement.....	63
8.2.1.1 Experimental apparatus	63
8.2.1.2 Data acquisition	65

8.2.1.3 Data reduction	66
8.2.2 Theoretical calculation of focus shift.....	66
8.2.3 Results.....	66
8.3 Periodic error.....	68
8.3.1 Cause	68
8.3.2 Error reduction.....	71
9. APPLICATION: TEMPERATURE MEASUREMENT	78
9.1 Experimental apparatus	78
9.2 Data acquisition	81
9.2.1 LCPDI.....	81
9.2.2 Thermocouple	82
9.3 Data processing.....	82
9.4 Results	95
10. CONCLUSION	97
APPENDIX A:	99
APPENDIX B:	100
APPENDIX C:	101
REFERENCES	104

1. LIST OF TABLES

TABLE 1. Simulation Parameters.....	100
--	------------

2. LIST OF FIGURES

FIGURE 4.1, Point diffraction interferometer	13
FIGURE 5.1, Ray model of the PDI	23
FIGURE 5.2, Wave model of the PDI.....	26
FIGURE 5.3, Transmittance and phase delay of LCPDI filter.....	28
FIGURE 5.4, Effect of pinhole diameter on reference wave; smooth object wave.....	31
FIGURE 5.5, Effect of pinhole diameter on reference wave; irregular object wave.....	33
FIGURE 5.6, Effect of pinhole diameter on reference wave; very irregular object wave.....	34
FIGURE 5.7, Homogeneous, homeotropic, and twisted nematic cells in relaxed state.....	37
FIGURE 5.8, Homogeneous cells with applied voltages.....	37
FIGURE 5.9, Optical configuration for phase-only modulation	40
FIGURE 6.1, Liquid crystal point diffraction interferometer filter schematic.	46
FIGURE 6.2, Electronic circuit for phase control.....	51
FIGURE 6.3, Liquid crystal point diffraction interferometer system schematic.	52
FIGURE 7.1, Image plane for greatly defocused LCPDI showing microspheres.	57
FIGURE 8.1, Liquid crystal phase calibration curve.....	61
FIGURE 8.2, Liquid crystal intensity calibration curve.....	62
FIGURE 8.3, Optical configuration for defocus measurement.....	64
FIGURE 8.4, Wavefront difference measured with LCPDI.	67
FIGURE 8.5, Cross-sections of wavefront difference, computed with the 5-frame algorithm and theoretical equation.....	69
FIGURE 8.6, Wavefront difference obtained from computer simulation.	72
FIGURE 8.7, Cross-sections of wavefront difference, obtained from computer simulation and LCPDI data.	73
FIGURE 8.8, Wavefront measured at Position 2, computed with Equation (22).....	74
FIGURE 8.9, Wavefront measured at Position 2, computed with 5-frame algorithm.	75
FIGURE 8.10, Cross sections of wavefront differences computed from (a) 2-D polynomial curve fits, (b) 5-frame algorithm, (c) Equation 22, and (d) Equation 23.	77
FIGURE 9.1, Experimental apparatus for temperature measurement.....	80
FIGURE 9.2, Raw, masked interferograms: (a) before and (b) after heat applied to top chamber plate.....	83
FIGURE 9.3, Normalized masked interferograms: (a) before and (b) after heat applied to top chamber plate.	86
FIGURE 9.4, Wavefronts measured with the LCPDI with the top chamber plate at (a) 23.4 °C and (b) 25.4 °C	88
FIGURE 9.5, Difference between wavefronts measured with isothermal and heated oil chamber.	90
FIGURE 9.6, Temperature measurement data.....	92

FIGURE 9.7, Interferogram with thermocouple probe inserted into chamber.	93
FIGURE 9.8, Plot of temperature across chamber, measured with LCPDI and traversing thermocouple.....	94

3. ABSTRACT

A new instrument, the liquid crystal point diffraction interferometer (LCPDI), has been developed for the measurement of phase objects. This instrument maintains the compact, robust design of Linnik's point diffraction interferometer (PDI) and adds to it phase stepping capability for quantitative interferogram analysis. The result is a compact, simple to align, environmentally insensitive interferometer capable of accurately measuring optical wavefronts with very high data density and with automated data reduction.

This dissertation describes the theory of both the PDI and liquid crystal phase control. The design considerations for the LCPDI are presented, including manufacturing considerations. The operation and performance of the LCPDI are discussed, including sections regarding alignment, calibration, and amplitude modulation effects. The LCPDI is then demonstrated using two phase objects: a defocus difference wavefront, and a temperature distribution across a heated chamber filled with silicone oil. The measured results are compared to theoretical or independently measured results and show excellent agreement.

A computer simulation of the LCPDI was performed to verify the source of observed periodic phase measurement error. The error stems from intensity variations caused by dye molecules rotating within the liquid crystal layer. Methods are discussed for reducing this error. Algorithms are presented which reduce this error; they are also useful for any phase-stepping interferometer that has unwanted intensity fluctuations, such as those caused by unregulated lasers.

It is expected that this instrument will have application in the fluid sciences as a diagnostic tool, particularly in space based applications where autonomy, robustness, and compactness are desirable qualities. It should also be useful for the testing of optical elements, provided a master is available for comparison.

4. INTRODUCTION

The point diffraction interferometer (PDI) has long been used for the measurement of optical wavefronts for lens testing and fluid flow diagnostics. It was invented by Linnik,¹ and reinvented by Smartt.^{2,3} Linnik's original paper is in Russian; an English translation is included as an appendix in a paper by Speer et. al.⁴

The PDI's primary advantage is its common-path design. An interferogram can be formed using only a single laser beam rather than the two beams required for Mach-Zender or Michelson interferometers. This is especially important when measuring large objects like wind tunnel flows where the optical paths are very long and air turbulence must be minimized along the paths. A single beam is also advantageous when the size of the instrument must be kept small, such as in microgravity experiments that must be contained in small packages for flight aboard the Space Shuttle or in drop tower containers. Lens testing interferometers also benefit from small packaging when they need to be used in industrial shop floors where space is at a premium.

The common-path design has other advantages because relatively few optical elements are required. The cost, size, and weight of the instrument are low. Alignment is simple, which is useful when working with invisible wavelengths; the PDI has been adapted for use in the UV and soft X-ray,⁴ and the IR.⁵ These features also make the instrument attractive for remote applications like those found on SpaceLab.

Although the PDI is a common-path interferometer, air turbulence in the object beam will affect the results, as will relative motion of the filter relative to the optical train. Therefore care must still be taken to provide a stable environment for operating the PDI.

The usefulness of the PDI has been primarily limited to qualitative interferogram analysis because its common path design precludes easy implementation of phase shifting interferometry. This document describes a new interferometer that retains the common path design of the PDI but permits automated, quantitative, interferogram interpretation by phase shifting. It uses a liquid crystal filter to introduce arbitrary phase shifts between the object and reference beams. A microsphere embedded within the liquid crystal layer provides a locally generated reference beam. The object beam is phase shifted by modulating the voltage across the liquid crystals, altering the refractive index of the birefringent nematic liquid crystals.

4.1 Point Diffraction Interferometer

4.1.1 Description

The PDI is elegantly simple. It is made from a neutral density filter with a pinhole in it, shown schematically in Figure 4.1. Collimated light is first reflected off or transmitted through an object of interest, and then brought to a focus onto the pinhole. The pinhole diameter is smaller than the focused spot, and so a spherical wave is generated by diffraction. The portion of the incident light unaffected by the pinhole is transmitted through and attenuated by the neutral density filter. Information contained in the incident wave is retained in the attenuated beam but filtered out of the diffracted wave. The two components of the transmitted wave are therefore referred to as the object and reference waves, respectively. They both travel coincidentally behind the PDI filter, and when combined coherently produce an interferogram whose appearance depends on the information in the incident wave of light. Good contrast is achieved by attenuating the object beam such that the relative intensities of the object and reference beams are similar.

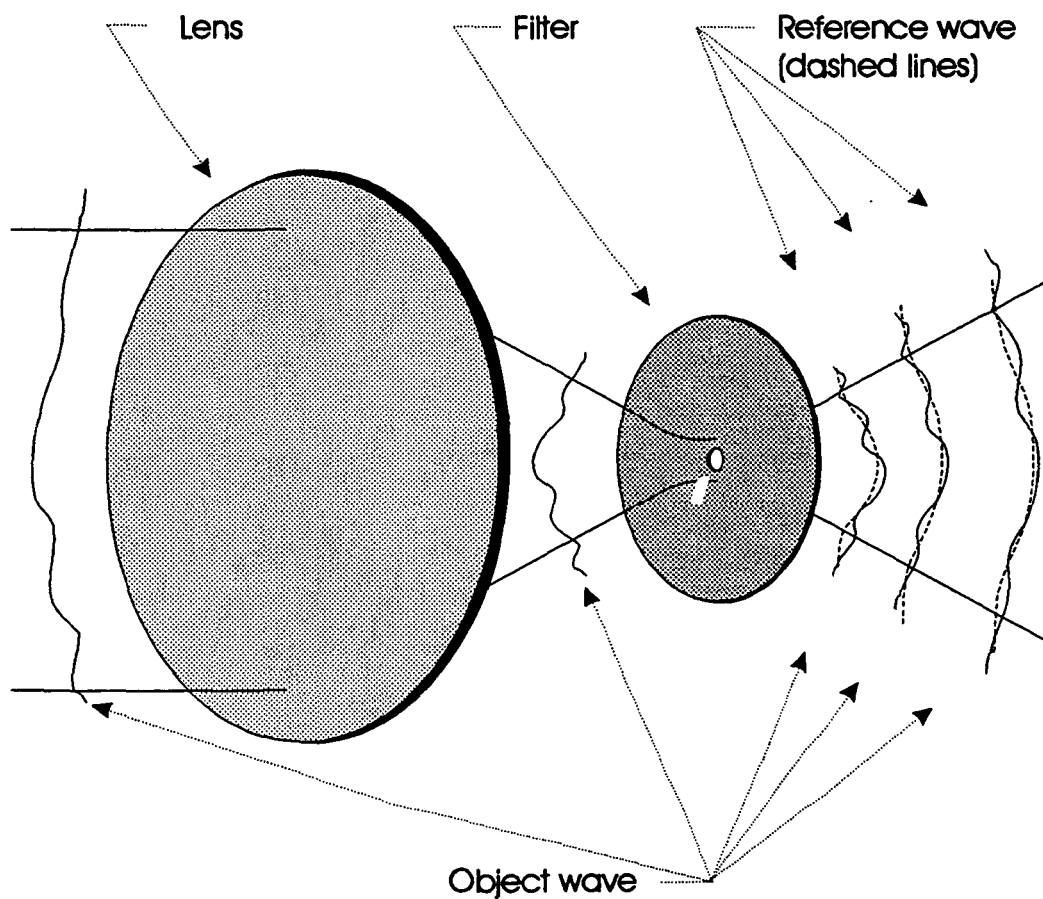


FIGURE 4.1, Point diffraction interferometer.

4.1.2 Applications

4.1.2.1 Optical Testing

The PDI has been used to test a wide variety of optical elements. Speer et. al.⁴ found that the PDI is well suited for the measurement of steep aspheric surfaces such as toric surfaces used for microscopy. Marioge et. al.⁶ have also used the PDI for measuring toric surfaces.

Harris et. al.⁷ used a Linnik line diffraction interferometer (LDI) to measure the quality of a monochromator grating used at UV and soft-X-ray wavelengths. The principle of the LDI is identical to the PDI, but a line is used rather than a pinhole to locally generate a cylindrical rather than a spherical reference wave.

4.1.2.2 Flow Metrology

Although Linnik¹ implied in the 1930's that the PDI would be useful for fluid studies, it wasn't until the 1980's that this application was demonstrated, by Aggarwal and Kaura.⁸ They deposited mercury droplets on glass-backed film emulsion, and then painstakingly exposed the film and removed the mercury to produce their PDI plates. They visualized fluid disturbances around a soldering iron using their PDI.

The PDI was one of several instruments selected for use in the International Microgravity Lab 2, flown aboard the Space Shuttle in July of 1994. It was chosen because of its compactness and inherent stability, critical factors for space experiments. The PDI that was flown was designed by an Italian company, Alenia Spazio, for the European Space Agency. They performed ground tests showing the feasibility of measuring refractive index variations in water as it was heated, and as alcohol was injected into it.^{9,10} Their work was strictly qualitative. An interesting aspect to their system was an automatic tilt

mechanism that kept the pinhole aligned on a bright spot in the focal plane regardless how aberrated the beam became. As successful as the ground tests were, the flight tests were a complete failure. No data was collected with the PDI. The interferograms had poor contrast and were very jittery. A mechanical mounting problem is suspected but has not yet been confirmed.

4.1.3 Interferogram analysis

Like any interferometer, the interferograms produced by the PDI must be interpreted to extract information about the object wavefront. This can be done visually by trained personnel, and this is common practice at many optical fabrication shops. The interferometric "fringes" assume characteristic shapes depending on the type of aberration present in the test optic, and corrective actions can be taken to modify the optical element until the desired fringe pattern is obtained.

For flow metrology however, the standard Seidel aberrations are virtually never the dominant aberrations forming the fringe pattern and so classical interferogram interpretations are inappropriate. Qualitative information regarding the flow can be seen by visual inspection, but typically more quantitative analysis is required.

One method that is sometimes found is manual fringe counting. This method is tedious, labor intensive, and subject to error, and so is not widely used.

Fringe-following software is available to automate this task. It works on the same principle as manual fringe counting: peaks or valleys of continuous interference fringes are identified. These lines represent lines of constant phase on the object beam wavefront.

The wavefront is reconstructed successively adding or subtracting 2π radians to each line, and interpolating between lines. The accuracy of this method is limited by the ability to find the true peaks and valleys of the fringe. This task is difficult because the slope of a cosine at its peaks and valleys is zero.

The sign of the aberration can not be determined from a single interferogram. The PDI plate must be moved relative to the focused beam and the fringe motion observed to determine the sign. Speer et. al.⁴ show this procedure graphically.

The most accurate and effective way to measure both the magnitude and the sign of wavefront aberrations is to use phase shifting interferometry (PSI).¹¹ The recorded interference pattern is an array of intensities that is related to the object wavefront $W(x,y)$ by:

$$I(x,y) = \bar{I}(x,y) \left\{ 1 + \eta(x,y) \cos \left[\frac{2\pi}{\lambda} W(x,y) + \Delta\phi \right] \right\} \quad (1)$$

where I is the recorded intensity, \bar{I} is the average intensity, η is the fringe visibility, and $\Delta\phi$ is a fixed phase difference. The designation (x,y) refers to individual pixels in the recorded interferogram. It can be seen that there are far more unknowns than equations, precluding a closed-form solution for the wavefront $W(x,y)$ from a single interferogram. However, the wavefront $W(x,y)$ can be explicitly solved for by recording n interferograms with judiciously chosen values for $\Delta\phi_n$:

$$I_n(x,y) = \bar{I}(x,y) \left\{ 1 + \eta(x,y) \cos \left[\frac{2\pi}{\lambda} W(x,y) + \Delta\phi_n \right] \right\} \quad (2)$$

The minimum number of frames, n , required is 3, but more frames will improve the measurement by reducing the sensitivity to phase stepping errors. Grievenkamp and

Bruning¹² describe standard algorithms for $n = 3, 4, 5$, and 6 . There are several assumptions common to all of these algorithms, namely that the values of \bar{I} , η , and W at each pixel do not vary from frame to frame, and that $\Delta\phi_n$ does not vary across the detector.

The phase at each point in the interferogram is calculated independently, producing a phase map with at least as much spatial resolution as there are pixels in the recording device. To use this technique, the interferometer must provide control over the relative phase of the object and reference beams.

4.2 Evolution of the PDI

Modifications to the PDI fall into three classifications: variations in the diffracting element, variations in the filter, and phase stepping modifications. These modifications are summarized here; additionally, instruments that are similar in purpose are discussed.

Smartt¹³ recognized that the PDI could be fabricated using a dark spot rather than a pinhole because of Babinet's principle, and Speer et. al.⁴ built a PDI that operated in reflection rather than transmission. They also combined the filter with the imaging optic for an even more compact instrument.

Wang et. al.¹⁴ used a linear polarizer rather than a neutral density filter to improve the fringe contrast, and James and Hariharan¹⁵ used a variable density filter for their LDI for the same reason.

The PDI is robust because of its common path design, but this same feature makes it difficult to shift the phase of one beam relative to the other to employ phase shifting techniques. Underwood et. al.¹⁶ added phase stepping to a reflection PDI. They forced the object and reference beams to have orthogonal polarizations, and used an electro-optic modulator to phase shift one relative to the other. The system used several extra optical elements, and had a very low optical throughput efficiency.

A variation of the PDI developed by Kwon¹⁷ used a specially fabricated diffraction grating to produce three phase shifted interferograms simultaneously. The wavefront phase can be determined from these interferograms, but three area detectors are required and the relative phase is fixed once the grating has been fabricated. This device is useful for high speed applications because time delays are not required between the acquisition of each interferogram.

Kadono et. al.¹⁸ also added phase stepping to the PDI by using a sequence of polarizing optics. A linear polarizer with a pinhole was followed by a quarter wave plate, half wave plate, and second linear polarizer. Phase stepping is accomplished by rotating the half-wave plate about the optical axis. The technique was demonstrated to have an accuracy of $\lambda/40$, but is limited to the measurement of small objects or very slow lenses because the incident light must be nearly normal to the polarizer. The intensity of the light was modulated as well as the phase.

The Zernike phase contrast method is very similar to the PDI; the primary difference is the phase and size of the diffracting element.¹⁹ The Zernike filter consists of a glass substrate with a small transparent dot coated on it. The dot retards the phase of the focused light by

either $\pi/2$ or $3\pi/2$ radians to shift the DC component of the object wave by a quarter wave. This produces an image whose intensity variation has an AC component that varies linearly with the phase of the object wave, provided the object wave deviates only slightly from spherical.²⁰ In practice, the Zernike diffracting aperture is larger than that used in the PDI, typically around 100 microns for the former and 5 microns for the latter. The larger aperture does not generate a truly spherical wave because low spatial frequency light passes through it; the Zernike phase contrast method is therefore used to see the high spatial frequency information in phase objects. It has application in biology²¹ and flow visualization.²²

Quercioli and Molesini²³ produced a Zernike interferometer by using a diffraction grating instead of a neutral density filter. They then used a grating with the same frequency but phase shifted by π radians in the small diameter central circular region. They selected the frequency so that the diffracted orders were separated behind the plate, and the first order was complementary to the zeroth order.

Another version of the Zernike interferometer was recently developed by Kadono et. al.²¹ Their device is very similar to the LCPDI. Both instruments use a thin liquid crystal layer to phase shift one beam relative to another, but they differ in the generation of the second beam. Instead of a microsphere diffracting a spherical wave, their device uses an etched circle in the electrodes to prevent molecular rotation in a cylindrical region nominally 100 microns in diameter. The relatively large size of the "hole" causes their device to act as a Zernike phase contrast interferometer rather than a PDI. The lower limit on their hole diameter is limited by electric field ringing across the edges; they show data indicating that

the ringing extends in about 10 microns, permitting a minimum hole diameter of about 20 microns.

Another instrument similar to the PDI was developed by both Linnik and Howes. Linnik used his PDI to measure wavefronts emitted by a pulsed ruby laser. He found that the high energy pulses tended to burn the pinhole edges, enlarging the hole with each use. He switched to a different system using a similar principle. He split the focused beam in two, reduced the intensity of each, and spatially filtered one of them to form a spherical reference beam.²⁴ The two beams were then recombined in a Mach-Zender configuration to form the interferogram. Howes reinvented this system²⁵ for use in flow visualization. Although this instrument isn't fully common path, it is substantially more robust than traditional interferometers in industrial environments. Phase stepping could easily have been added to this system by mounting one of the Mach-Zender mirrors on a piezo-electrically controlled stage.

A common-path phase-shifting interferometer was developed by Iwata and Nishikawa²⁶ based on polarization optics. Their device relies on a calcite lens to focus only the one polarization component of collimated incident light, passing the other polarization unaffected. The relative phase of these two beams is controlled with a Soleil compensator. While this instrument is similar to the LCPDI in that it is a phase-stepped common-path interferometer, the LCPDI is used to measure phase objects while Iwata's device is for the measurement of opaque surfaces.

Another common-path diffraction interferometer was recently invented by Churin and Sedukhin.²⁷ A Fresnel zone plate is used to split collimated light into the first and zeroth

diffracted orders. The first order is focused onto a planar phase object and used as a reference beam, while the zeroth order becomes the object beam. A modulated zone plate re-collimates the reference beam, but also alters its phase distribution to produce circular, radial, or straight line fringes. This versatility increases the range of objects that can be measured, but the instrument is limited to the measurement of planar phase objects.

Finally, Wanzhi and Zhenwu²⁸ developed a holographic version of the PDI. However, their system is not common-path because a reference beam is required for holographic recording and reconstruction, and aberrations from a beam splitter and a mirror can not be distinguished from aberrations in the test lens.

4.3 Liquid crystal PDI

This dissertation describes a new modification to the classic PDI. The modification consists of replacing the neutral density filter with a liquid crystal layer to control the phase of the object beam. Phase modulation is achieved by manipulating the orientation of the individual molecules to control the refractive index of the liquid crystal layer. The phase of light passing through a hole in the layer will not be affected, so the phase difference between the object and reference beams can be controlled. This allows completely flexible phase stepping interferometry capability while retaining the full common-path optical design.

The theory, design, manufacture, performance, and application of the LCPDI will be described in the following sections.

5. THEORY

5.1 Principle of the LCPDI

The LCPDI works in the same way as the classic PDI. Light is brought to a focus on and is filtered by the PDI plate. The central portion of the incident wave is diffracted to form a spherical reference wave, while the remainder of the light is attenuated and forms the object wave. Aberrations in the incident wave are indicated by the resultant interferogram.

The differences between the LCPDI and the PDI lie in the physical differences in the filter. The PDI uses a neutral density filter with a pinhole; the LCPDI uses a liquid crystal layer with an embedded microsphere. In both cases, the principle behind the formation of the interferogram can be understood by considering the light passing through the interferometer as either rays or waves. While the wave model is more representative of the physical situation, the ray model is much simpler and provides good insight.

5.1.1 Ray Model

A ray model of the LCPDI is shown in Figure 5.1. The LCPDI filter is represented by a liquid crystal layer of thickness t sandwiched between two glass plates, each of thickness t_g . The object beam is modeled as rays intersecting at a single point within the filter; the reference beam is modeled as a ray fan originating from this point. A point on the surface of the liquid crystal layer was chosen instead of the mid-point to simplify the equations; this choice does not fundamentally affect the results of the model. The phase difference between the waves represented by these rays in a plane behind the LCPDI is given by:

$$\Delta\phi(x, y) = \phi_{obj}(x, y) + \frac{2\pi}{\lambda} L(x, y)(n_{LC} - n_{sphere}) + \phi_0 \quad (3)$$

where $\phi_{obj}(x, y)$ represents the phase distribution of the object rays at the front of the liquid crystal layer, ϕ_0 represents a fixed phase difference, $L(x, y)$ represents the physical

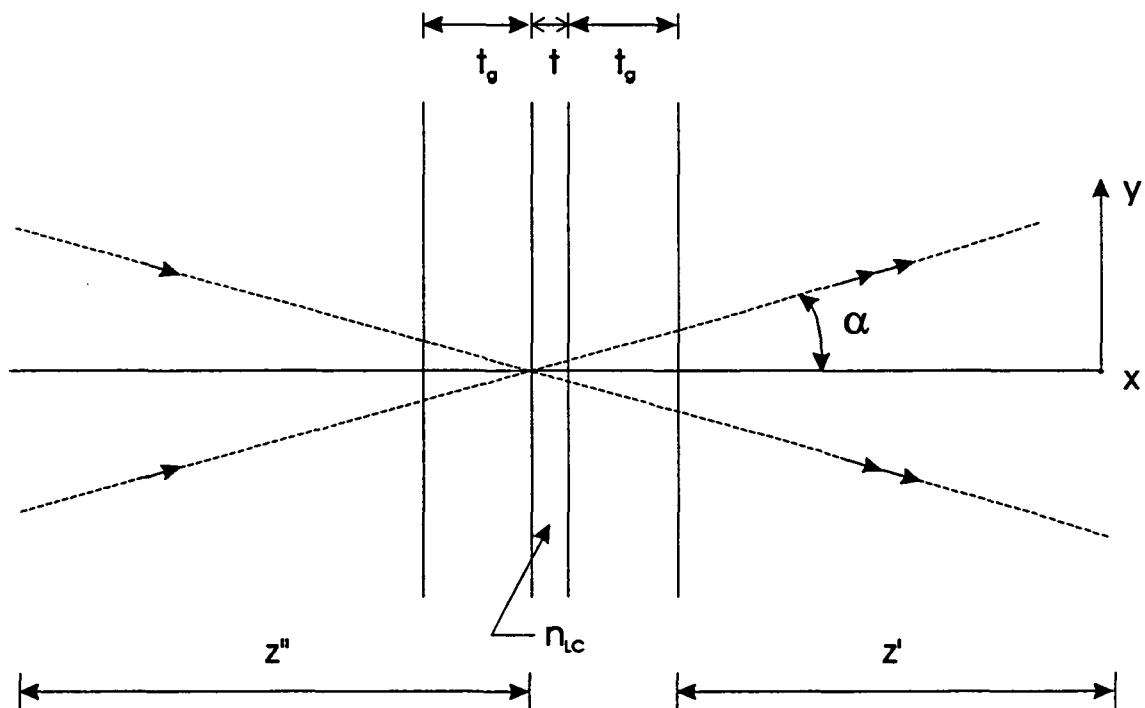


FIGURE 5.1, Ray model of the PDI.

length of the rays within the liquid crystal layer, and n_{LC} and n_{sphere} represent the refractive indices of the liquid crystal layer and microsphere, respectively. This length varies with the angle α between the incident ray and the optic axis according to the following relationship:

$$L(x, y) = \frac{t}{\cos[\alpha(x, y)]} \quad (4)$$

where t represents the thickness of the liquid crystal layer. This factor introduces a geometrical phase difference that has a maximum value between the marginal and chief rays. This maximum value is equal to:

$$\Delta L_{max} = t \left\{ 1 - 1 / \cos \left[\tan^{-1} \left(\frac{1}{2f\#} \right) \right] \right\} \quad (5)$$

where $f\#$ refers to the ratio of the focal length to the diameter of the focusing lens. For a liquid crystal layer thickness of 9 microns, this path difference is equal to 2.1 wavelengths at f/1, 0.28 waves at f/2.8, and only 0.06 waves at f/6. Therefore this term can be ignored for optics slower than about f/2.8. Even for faster optics, the effect of this error can be minimized by using the correct phase extraction algorithm.²⁹ For completeness though, the angle α is related to the image coordinates by the following expression:

$$\alpha(x, y) = \tan^{-1} \left(\frac{\sqrt{x^2 + y^2}}{z'} \right) \quad (6)$$

where z' is the distance between the rear face of the LCPDI plate and the viewing screen and (x, y) is the position on the screen. Combining equations 3, 4, and 6 to describe the phase variation $\Delta\phi(x, y)$ across the detector array yields:

$$\Delta\phi(x, y) = \phi_{obj}(x, y) + \frac{2\pi}{\lambda} \frac{t(n_{LC} - n_{sphere})}{\cos \left[\tan^{-1} \left(\frac{\sqrt{x^2 + y^2}}{z'} \right) \right]} + \phi_0 \quad (7)$$

which can be approximated by:

$$\Delta\phi(x, y) \approx \phi_{obj}(x, y) + \frac{2\pi}{\lambda} t(n_{LC} - n_{sphere}) \quad (8)$$

for nearly all cases, as qualified above. This expression relates the phase detected at a plane behind the LCPDI to the phase distribution of the original object wave. This phase distribution can then be stepped or ramped by varying the refractive index of the liquid crystal layer.

Finally, note that $\phi_{Obj}(x, y)$ is related to the phase distribution W of the object beam in front of the LCPDI plate a distance z'' by:

$$\phi_{obj}(x, y) = \frac{2\pi}{\lambda} W(x, y) + \frac{2\pi}{\lambda} \frac{z'' + t_g}{\cos(\alpha)} \quad (9)$$

where t_g is the thickness of the front glass plate. Note that this correction becomes a simple piston shift if the angle α is less than about 5 degrees.

5.1.2 Wave Model

Following the procedure used in Reference [5], Fourier theory can be used to analyze the PDI. Figure 5.2 shows PDI system schematic, with the planes used in the analysis indicated. The interferogram is imaged onto a camera, and the object and reference waves in the image plane are determined using Fourier analysis.

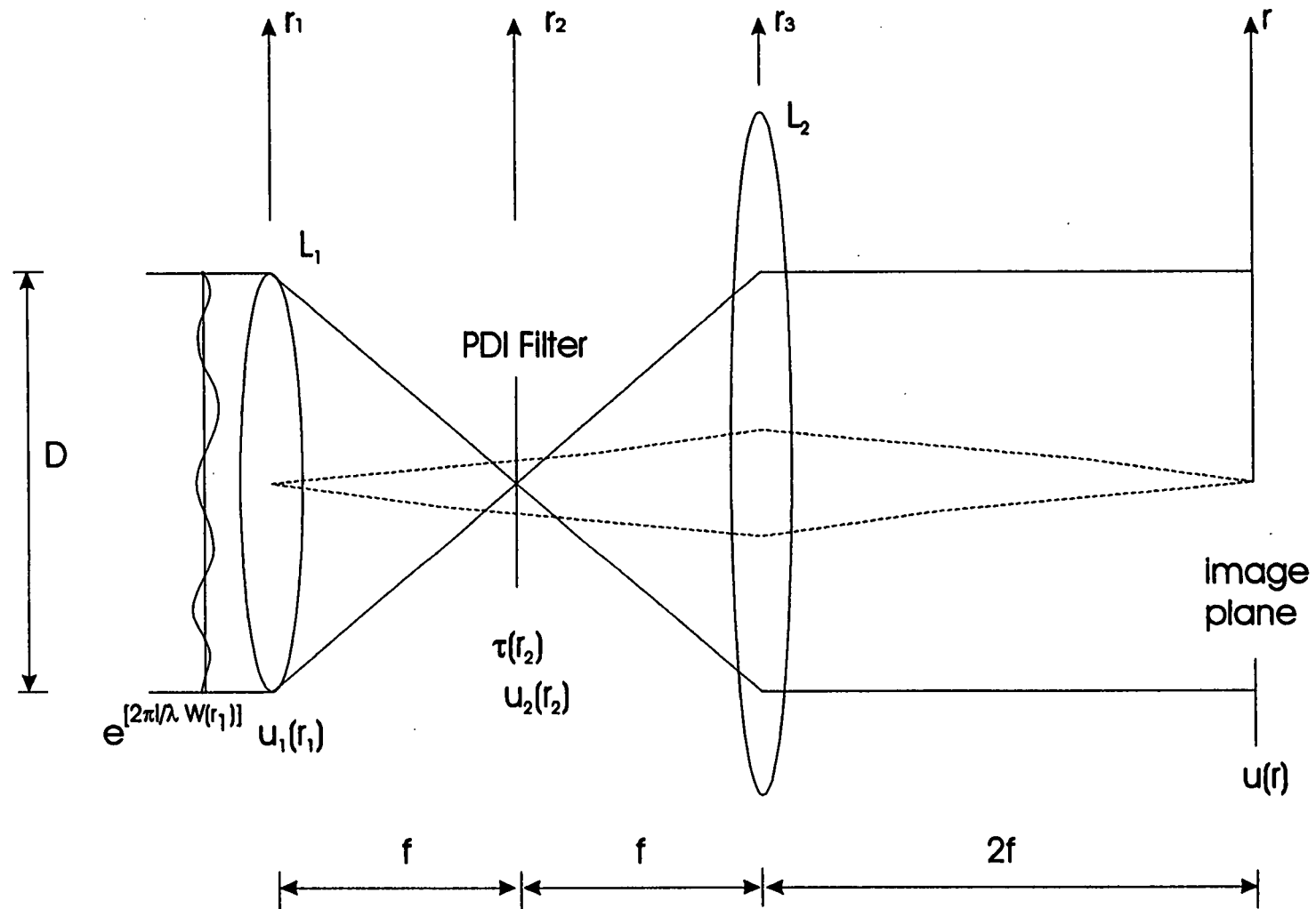


FIGURE 5.2, Wave model of the PDI.

A unit-amplitude plane wave, with wavelength λ and aberration $W(r_1)$ superimposed, is incident on aberration-free thin lens L_1 having diameter D and focal length f . The optical field just behind L_1 is described by the product of the initial wave and the lens pupil function:

$$u_1(r_1) = cyl\left(\frac{r_1}{D}\right) \exp\left[\frac{2\pi i}{\lambda} W(r_1)\right] \quad (10)$$

The cylinder function, $cyl(r_1/D)$, represents a function equal to zero everywhere except for $r_1 < D/2$, where the function equals one.³⁰ This field propagates to the focal plane, where it is described by its Fourier transform, $U_1(r_2)$, where the transform is evaluated at the spatial frequency $\rho = r_2/\lambda f$. At the focal plane the field is multiplied by the transmittance of the PDI plate $\tau(r_2)$, given by:

$$\tau(r_2) = \left[\tau_b + (1 - \tau_b) cyl\left(\frac{r_2}{d}\right) \right] \exp\left\{ i \left[\phi_b + (\phi_0 - \phi_b) cyl\left(\frac{r_2}{d}\right) \right] \right\} \quad (11)$$

where τ_b and ϕ_b are the transmittance of and phase delay caused by the background plate, d is the pinhole diameter, and ϕ_0 is the phase delay of the pinhole. The pinhole transmittance is 1. This plate is shown graphically in Figure 5.3.

The optical field just behind the pinhole is then described by:

$$u_2(r_2) = \tau(r_2) U_1(r_2) \quad (12)$$

Lens L_2 images the field at plane 1 through the filter and onto the image plane. The effect of the filter can be understood by considering instead an effective wavefront emerging from lens L_1 and passing through no filter. In order to create the known wavefront just behind the focal plane given by Equation (12), the effective wavefront behind L_1 must equal the inverse Fourier transform of u_2 . The image then becomes a scaled copy of this

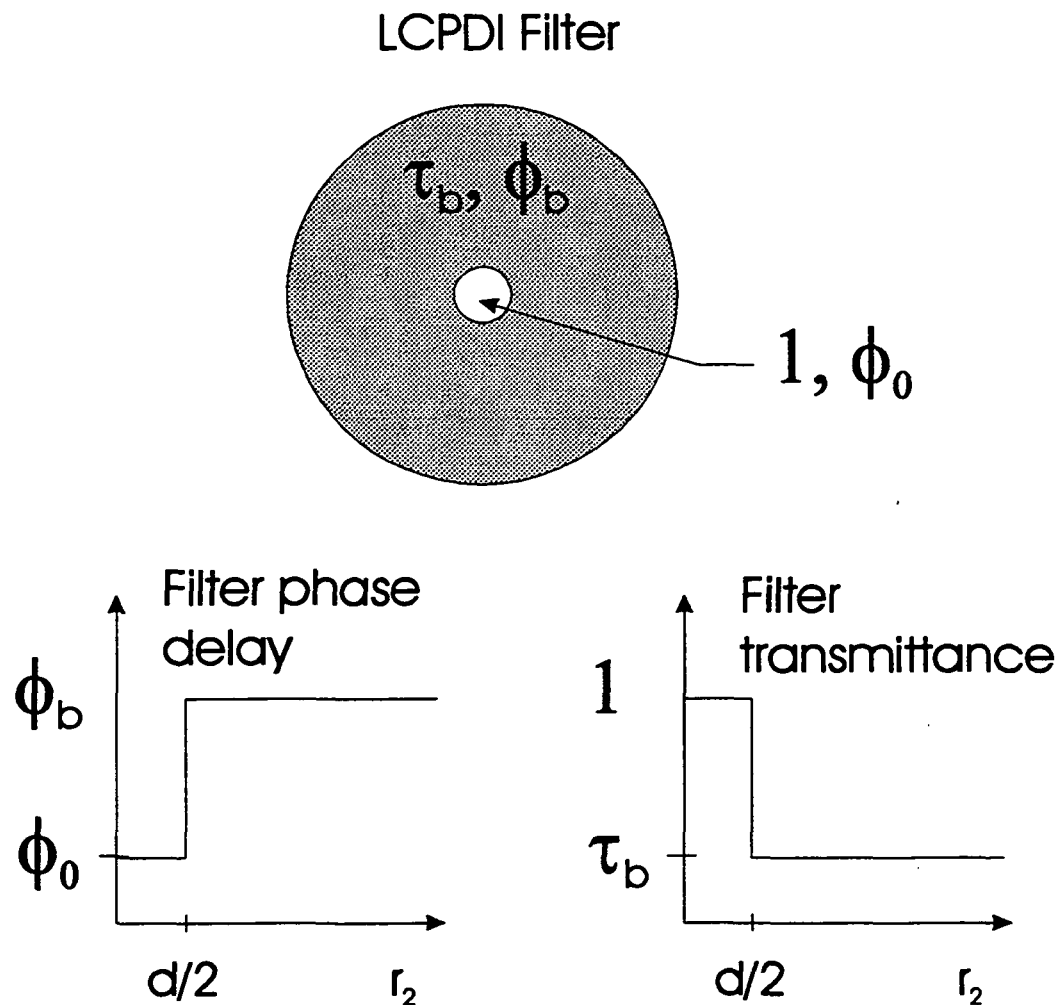


FIGURE 5.3, Transmittance and phase delay of LCPDI filter.

effective wave convolved with the imaging lens' impulse response function. For a high quality, thin spherical lens used paraxially, this function is a sombrero function that smoothes the image; for the purpose of this discussion it will be assumed to be a delta function. This is the limiting form of the function as the lens diameter becomes very large and the lens becomes very thin. Assuming unit magnification, a focused beam centered on the pinhole, and neglecting the Petzval curvature across the image and a complex proportionality constant, the field in the image plane is described by:

$$u(r) = T(r) \ast\ast u_1(r) \quad (13)$$

where the symbol $\ast\ast$ represents a two-dimensional convolution, and $T(r)$ is the Fourier transform of $\tau(r_2)$, given by:

$$T(r) = [\exp(i\phi_0) - \tau_b \exp(i\phi_b)] \frac{\pi d^2}{4\lambda f} \text{somb}\left(\frac{dr}{\lambda f}\right) + \tau_b \exp(i\phi_b) \delta\left(\frac{r}{\lambda f}\right) \quad (14)$$

where $\delta(\)$ is the two-dimensional Dirac delta function; and the sombrero function³⁰, $\text{somb}(cr)$, is given by $2 J_1(\pi cr) / (\pi cr)$, where c is a constant and $J_1(x)$ is a first order Bessel function of the first kind. The optical field at the image plane is then:

$$\begin{aligned} u(r) = & \tau_b \exp(i\phi_b) \text{cyl}\left(\frac{r}{d}\right) \exp\left[\frac{2\pi i}{\lambda} W(r)\right] + \\ & [\exp(i\phi_0) - \tau_b \exp(i\phi_b)] \frac{\pi d^2}{4\lambda f} \text{somb}\left(\frac{dr}{\lambda f}\right) \ast\ast \text{cyl}\left(\frac{r}{d}\right) \exp\left[\frac{2\pi i}{\lambda} W(r)\right] \end{aligned} \quad (15)$$

where the complex constant of proportionality has been dropped. The derivations for these expressions are given in Appendix C. This equation shows that the interferogram is formed by the coherent addition of the attenuated aberrated wavefront and a reference wavefront formed by the convolution of the aberrated wavefront with the Fourier transform of the central portion of the PDI plate. These object and reference waves are

the first and second terms in this equation, respectively. The reference wavefront is a smoothed version of the object wave.

In the limit as the pinhole diameter approaches infinity, the sombrero function approaches a Dirac delta function and the reference wave becomes an attenuated copy of the object wave:

$$u_{ref} \lim d \rightarrow \infty = [\exp(i\phi_0) + \tau_b \exp(i\phi_b)] \frac{(\pi d)^2}{2\lambda f} cyl\left(\frac{r}{d}\right) \exp\left[\frac{2\pi i}{\lambda} W(r)\right] \quad (16)$$

At the other extreme, as the pinhole diameter approaches zero, the sombrero function approaches a constant, and the reference wave becomes an integrated version of the object wave, i.e., a smooth continuous function:

$$u_{ref} \lim d \rightarrow 0 = [\exp(i\phi_0) + \tau_b \exp(i\phi_b)] \frac{(\pi d)^2}{2\lambda f} \int_0^{r-D/2} \exp\left[\frac{2\pi i}{\lambda} W(r-r')\right] r' dr' \quad (17)$$

Note that this is not independent of the object wave, but for relatively slowly varying functions $W(r)$ the reference wave becomes spherical.

Figure 5.4 shows the effect of the pinhole size on the generated reference wave. A cross section of the original wavefront is shown in plot (a), followed by plots (b) through (h) showing corresponding cross sections in the image plane of reference beams generated by pinholes of increasing size. The pinhole diameters in these plots are equal to 0.1, 1, 3, 10, 33, 100, and 1000 times the unaberrated Airy disk radius, respectively. In each of the latter plots, the portion of the focused beam intersected by the pinhole is shown on the left, and the reference beam generated by that pinhole is shown on the right. The abscissa is scaled by the lens diameter D , but the focused beam plot is magnified in the x-axis by d/D for clarity. Plots (b) and (c) show that pinholes smaller than the Airy disk generate

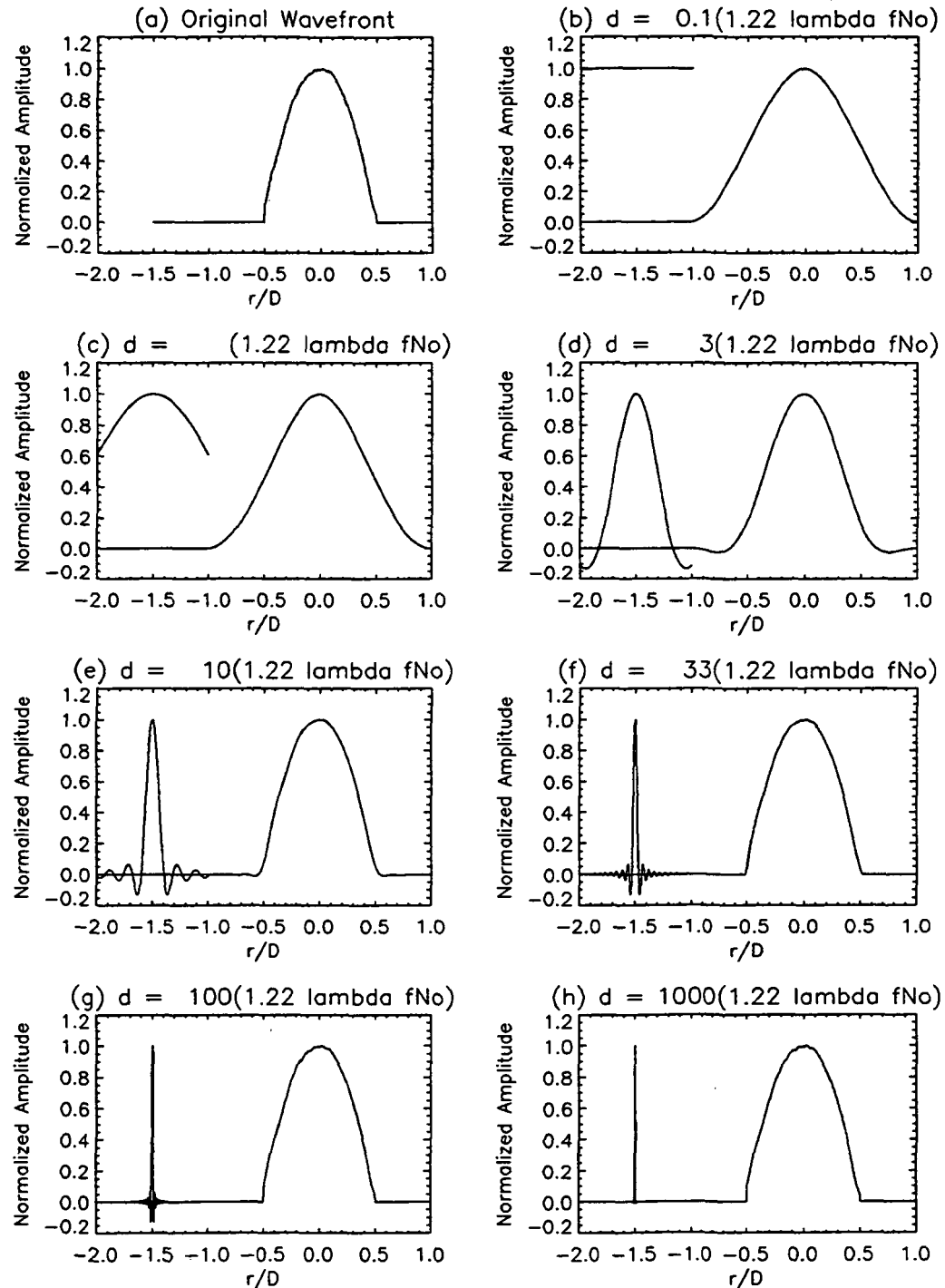


FIGURE 5.4, Effect of pinhole diameter on reference wave; smooth object wave.

spherical reference waves as described in Sections 4.1.1 and 5.1. Note that the pinhole diameter equal to one-half the Airy disk diameter is shown in plot (c); this is the recommended pinhole size given by Koliopoulos et. al.⁵

Figures 5.5 and 5.6 show the same trend for increasingly irregular object wavefronts. These figures show that even a pinhole one-tenth the size of the Airy disk radius does not generate a spherical wave when the object wave is highly aspheric. A pinhole three times larger than the Airy disk radius still filters out most of the object wave, but the object wave structure is noticeable at 10 times and pronounced at 33 times the recommended size. By the time the pinhole is 1000 times the Airy disk radius, the entire object wave is transmitted. This sequence of figures shows that the correct size for the diffracting element depends on the spatial frequency content in the object wave. For highly irregular object waves like those created by fluids experiments, a diffracting element with a diameter of about three times larger than the Airy disk radius is acceptable. For nearly spherical waves like those created by high quality optical elements, the diffracting element should be kept smaller than one Airy disk radius.

Note that apertures used for Zernike's phase contrast method typically are about 33 times the Airy disk radius,²⁰ corresponding to panels (f) in Figures 5.4 - 5.6. Clearly only the high frequency content of the object wave can be discriminated by this method. The data to be presented in Sections 8 and 9 of this dissertation were obtained with a diffracting element three times the Airy disk radius, corresponding to panel (d) in Figures 5.4 - 5.6.

Equation (15) shows that the phase difference between the object and reference waves can be varied by controlling either ϕ_0 or ϕ_b . Conventional PDIs have both ϕ_0 and ϕ_b set to

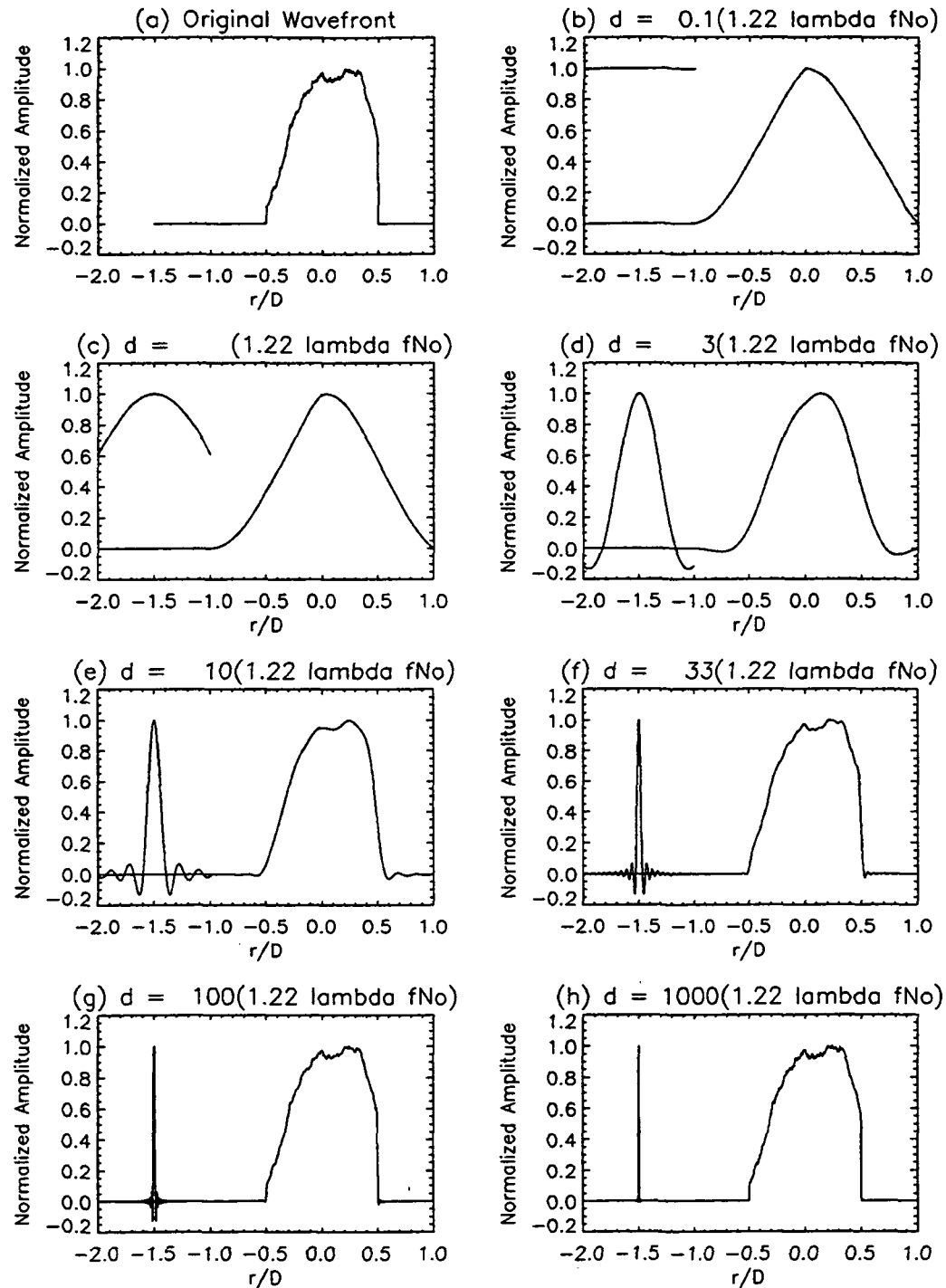


FIGURE 5.5, Effect of pinhole diameter on reference wave; irregular object wave.

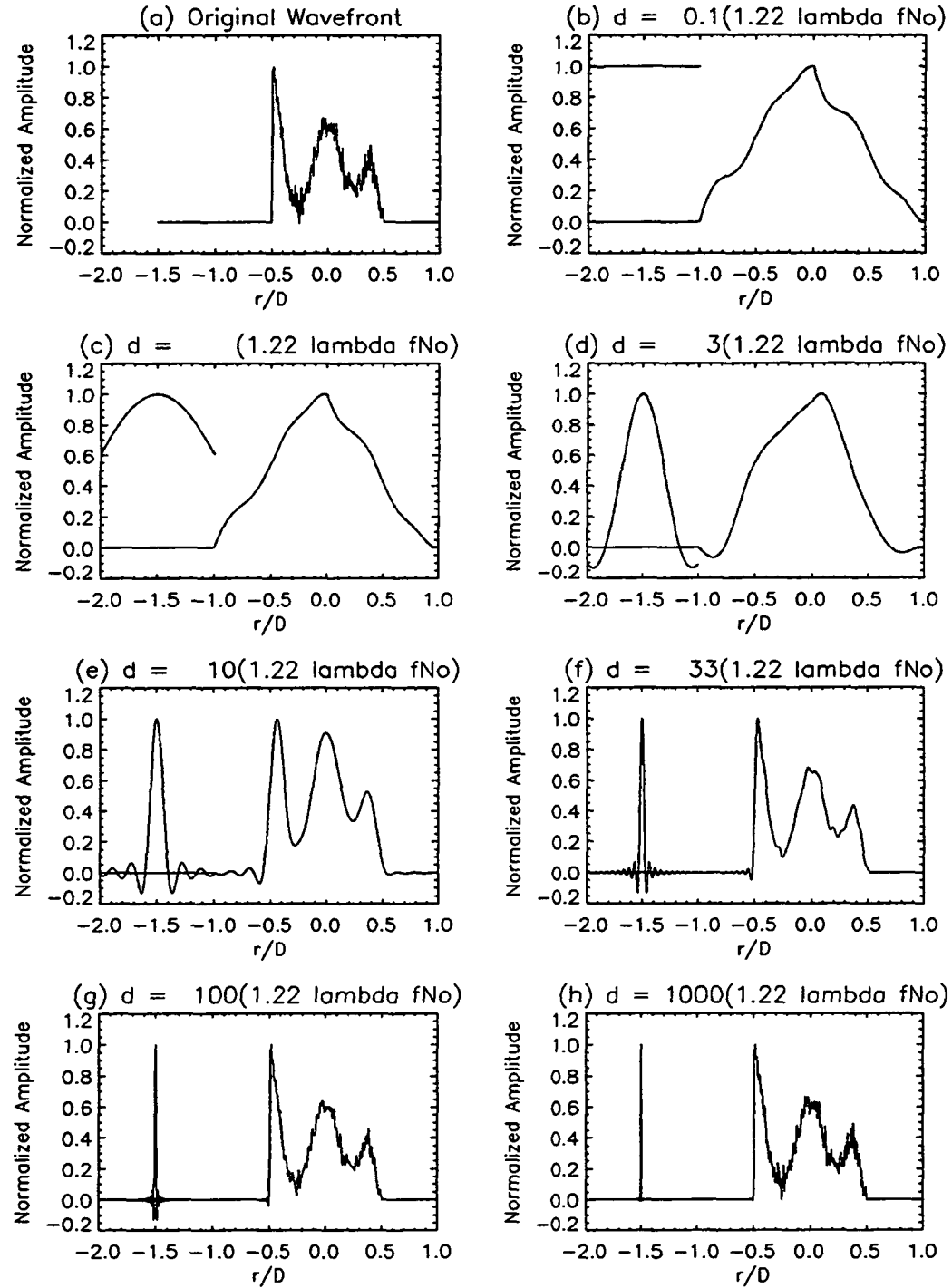


FIGURE 5.6, Effect of pinhole diameter on reference wave; very irregular object wave.

fixed values. It will be shown that the LCPDI provides control of the background phase delay ϕ_b , permitting the use of phase shifting interferometry.

Finally, note that by Babinet's principle it is equivalent to use a hole or a spot to form the diffracted reference beam. It is also equivalent to use a sphere rather than a hole. This simplifies the manufacturing process for the LCPDI because it is easier to embed a sphere in a liquid crystal layer than to produce a very small hole in it.

5.2 Principle of liquid crystal phase control

Liquid crystals can be used to control the optical phase of light transmitted through them. Various types of liquid crystals were considered for use in the LCPDI. A discussion of these types follows, showing why the particular type of liquid crystal that was used in the LCPDI was chosen.

Liquid crystals are a state of matter; their molecules have some orientational order like a solid, but are free to move relative to each other like a liquid. Thermotropic liquid crystals occur naturally in either nematic or discotic forms. Nematic liquid crystals have long, thread-like molecules, while the discotic molecules are shaped like disks. The long axis of a nematic liquid crystal molecule is called its director. Both forms are known as thermotropic liquid crystals because their liquid crystal phase is temperature dependent.

Both nematic and discotic liquid crystals are birefringent. The refractive index of the material is a function of the molecular orientation. The molecules are electric dipoles, and so this orientation can be manipulated by external electric fields.

Ferroelectric liquid crystals are a common discotic form. Their principle advantage is the speed with which their orientation can change, but this orientation can only assume two positions, allowing only two discrete phase steps per liquid crystal layer. While these layers can be stacked to provide the sequence of phase steps required for phase shifting interferometry, this approach was not taken for the LCPDI and discotic liquid crystals were not considered further.

Nematic liquid crystals can be operated so that their refractive index varies continuously between the ordinary and extraordinary index of refraction. Therefore nematic liquid crystals were chosen for the LCPDI.

There are three orientations for thin nematic liquid crystals layers: Homogeneous, homeotropic, and twisted. The difference among these three types is the initial orientation of the molecules. Sketches of the three types are shown in Figure 5.7. In each case the liquid crystal layer is sandwiched between two glass plates. The homogeneous and twisted nematic orientations are produced by coating the glass plates with a plastic layer, rubbing a cloth across the plastic to create micro grooves, and then polymerizing the plastic to fix the grooves. The homogeneous orientation is produced by aligning the coated glass plates so that their micro grooves are parallel; one plate is rotated by ninety degrees from the other to produce a twisted nematic cell. Homeotropic liquid crystals are aligned perpendicular to the glass plate. This is accomplished by coating the plates with a chemical that repels one end of the liquid crystal molecules.

The response of a thin homogeneous nematic liquid crystal layer to an externally applied electric field is shown in Figure 5.8. Three values of electric field amplitude are depicted.

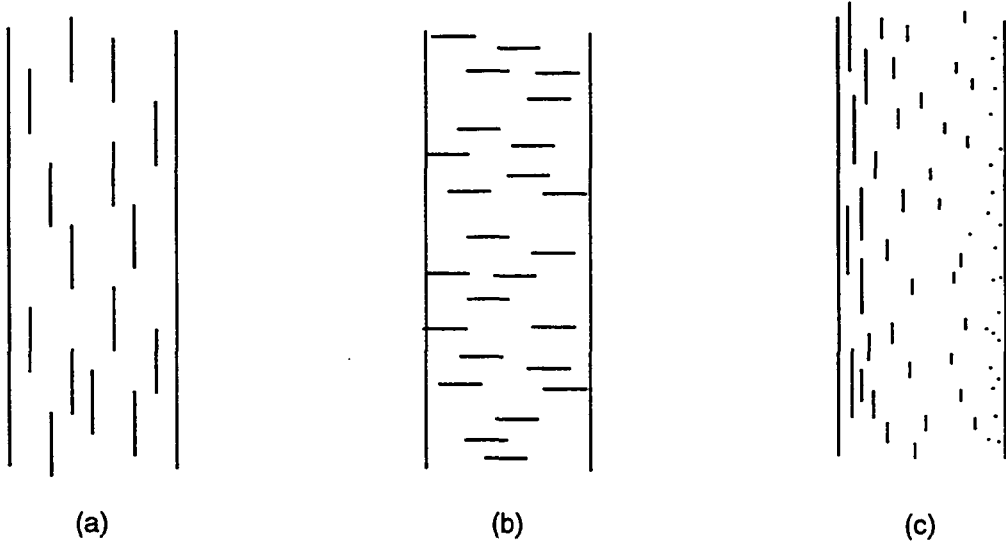


FIGURE 5.7, Homogeneous, homeotropic, and twisted nematic cells in relaxed state.

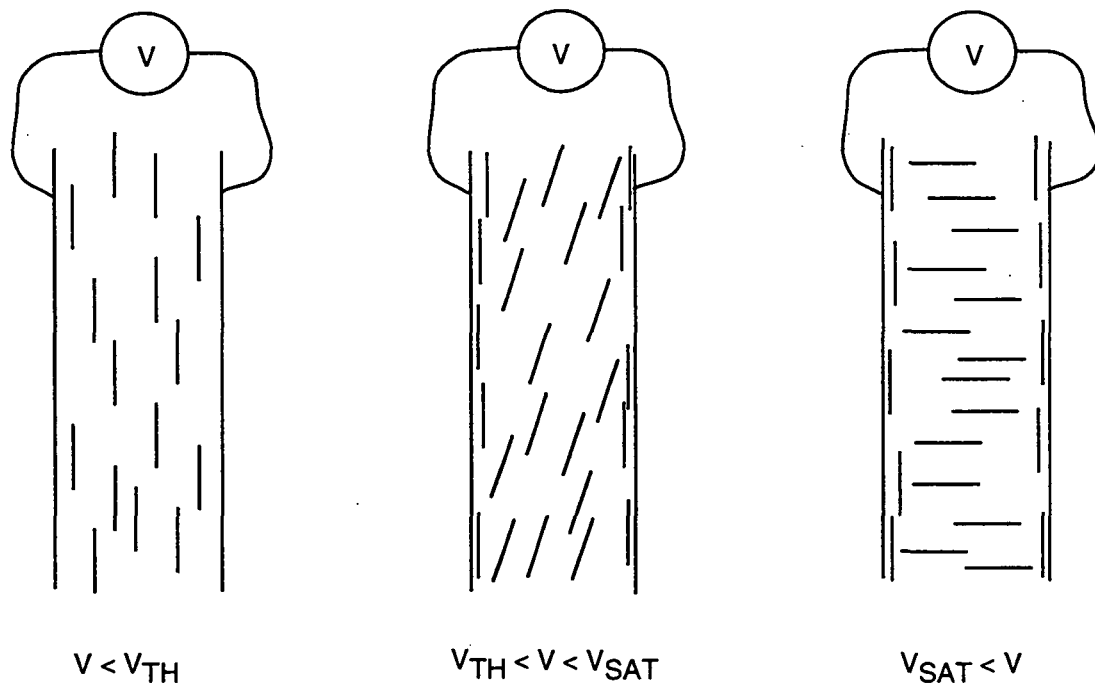


FIGURE 5.8, Homogeneous cells with applied voltages.

V1 below threshold, V2 above threshold and below saturation, V3 above saturation.

Except for the molecules immediately adjacent to the glass plates, the directors realign themselves along the electric field. The boundary layer molecules remain oriented with the grooves in the glass. The reorientation does not occur until a certain threshold value of the electric amplitude is reached. The sudden response of the molecules to the applied field is known as the Freedericksz transition. Above this threshold, the directors rotate ever closer to the optic axis with increasing electric field strength, until they are parallel with the optic axis. Increased field strength above this point has no effect until the liquid crystals break down and short the circuit. As long as the electric field is kept below the damage threshold, weak electrical forces will return the molecules to their original orientations when the field is removed. This realignment occurs because the molecules immediately next to the glass plates do not rotate with the applied field, and each molecule is an electric dipole.

Twisted nematic liquid crystals are reoriented in the same way when an electric field is applied across the layer. Homeotropic liquid crystals require an electric field applied parallel to the glass plates to effect an orientational change. This is difficult to do and so a homeotropic orientation was not used for the LCPDI.

Twisted nematic liquid crystals are the type commonly found in clocks and computer screens. The twist in the orientation of the molecules makes this arrangement optically active. Light linearly polarized parallel to the grooves in the first plate has its polarization rotated by ninety degrees by the liquid crystal molecules. An applied electric field will destroy this polarization rotation, thereby destroying the optical activity of the layer. By placing this layer between crossed polarizers, the light incident on the final polarizer can

be alternately absorbed or transmitted by applying an external electric field and then removing it.

Parallel nematic liquid crystals are also used for amplitude modulation, using selective interference. Light polarized at 45 degrees to the liquid crystal directors is passed through the liquid crystal layer and through a crossed polarizer. If the thickness of the liquid crystal layer is such that the extraordinary beam is retarded by one-half of a wavelength relative to the ordinary beam, the liquid crystals act as a half-wave plate and all the light is transmitted through the second polarizer. An applied electric field thwarts the phase delay, and the light is blocked. This device is very sensitive to wavelength, thickness, and incidence angle, but the molecules can be switched slightly faster than in the twisted configuration.³¹

Phase modulation has recently been demonstrated using both twisted and homogeneous nematic liquid crystals.^{32,33,34} The optical system required for phase-only modulation is shown in Figure 5.9. Linear polarized light is incident on a homogeneous nematic liquid crystal layer. The polarization direction is parallel to the grooves in the glass plates. The second polarizer is parallel to the first. These polarizers are used to select the desired polarization state for the incident light, and to discard the small component of light that is depolarized from molecular scattering. In the absence of an applied electric field, the directors are aligned parallel to the polarization direction and the material's refractive index is equal to the extraordinary index of refraction. As the strength of an applied electric field increases above the value required for the Freedericksz transition , the directors rotate towards the optic axis, and the refractive index shifts towards the ordinary index of refraction until the directors are parallel to the optic axis and the refractive index

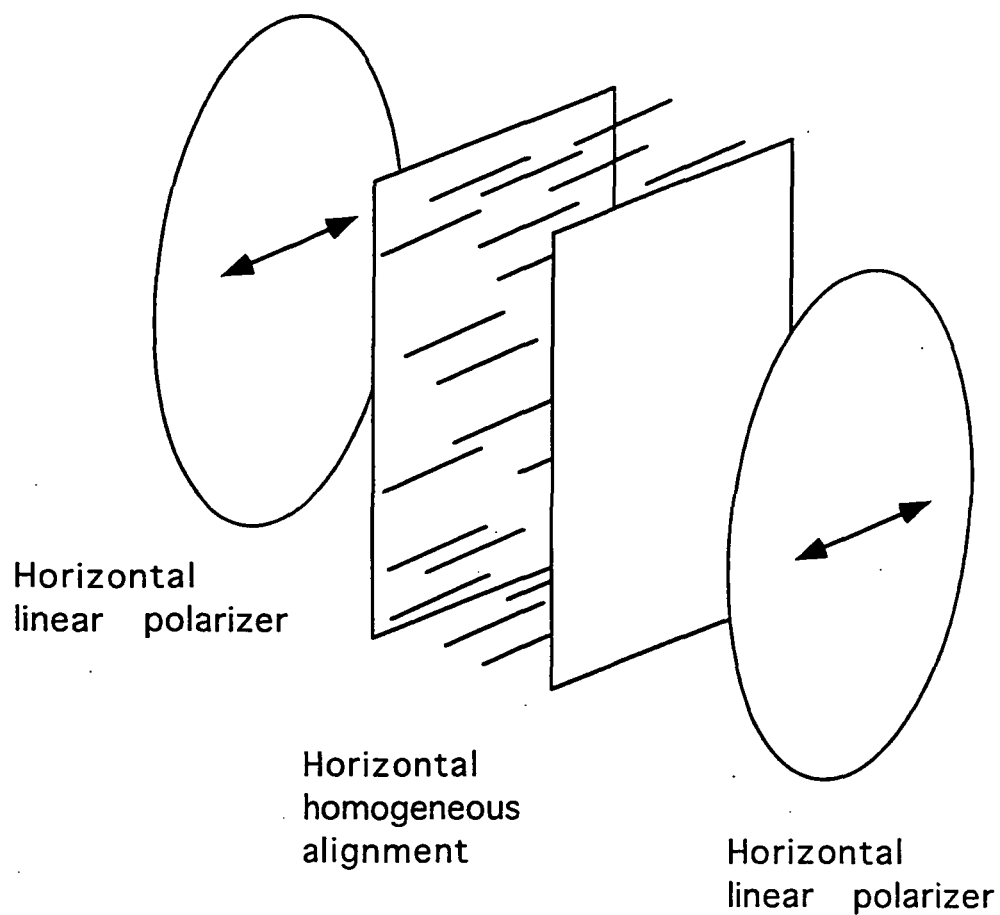


FIGURE 5.9, Optical configuration for phase-only modulation.

equals the ordinary index. This process works for twisted nematic cells too, but the second polarizer must be perpendicular to the first and the amplitude of the applied voltage must be above the Fredericksz value but must not exceed the optical threshold. Within this range the directors will realign themselves with the electric field, but not lose their twist. Above the optical threshold the optical activity of the cell is affected and the amplitude will be modulated as well.³³

Alternating current is required to reorient the liquid crystal molecules. The molecules will not oscillate with the field provided the electric field frequency is at least 1 kHz. A direct current will damage the device by burning the electrodes.

Homogeneous nematic cells produce more phase shift for a given thickness than do equivalent twisted cells,³² but the twisted cells add the ability to modulate either the phase, or the amplitude, or both. This latter feature is not an advantage for the LCPDI so parallel nematic liquid crystals were chosen for this application.

One final possible orientation is the anti-parallel nematic liquid crystal. The grooves in the glass plates are parallel to each other, but one plate is rotated by 180 degrees after assembly so that the molecular orientation also rotates 180 degrees across the layer thickness. Anti-parallel cells require a higher electric field strength for a given phase shift as compared to a parallel cell, and so anti-parallel cells were not used for the LCPDI. A common technique used in liquid crystal devices is the application of a relatively high voltage across the electrodes when the device is turned on. This high voltage, about 40 VAC for anti-parallel and 15 VAC for parallel nematic liquid crystals, overcomes the weak

electric forces between the molecules, making the molecules more responsive to subsequent, lower voltage, applied fields.

5.3 Phase calculation

The information from the previous two sections can be combined to create a phase shifted LCPDI. Equation (8) becomes:

$$\Delta\phi_j(x, y) = \phi_{obj}(x, y) + \frac{2\pi}{\lambda} t(n_{LC_j} - n_{sphere}) \quad (18)$$

where the symbols are the same as those used for Equation 8. To provide phase stepped interferograms, voltage steps are applied across the liquid crystal layer to produce values for n_{LC_j} such that $\Delta\phi_{j+1}(x, y) - \Delta\phi_j(x, y) = \beta$, where β is the desired phase step. The wavefront phase W can then be calculated using the algorithms referenced in Section 4.1.3, provided that the assumptions implicit in those equations are met.

5.3.1 Assumption violations

As stated in section 4.1.3, there are two assumptions that must be satisfied to use the standard phase extraction algorithms. One assumption is that the phase steps must be uniform across the interferogram, the other is that neither the object nor the reference beam intensities vary from frame to frame.

Errors caused by the non-uniform phase shifts will manifest themselves as a phase measurement error that occurs at twice the spatial frequency of the interference fringes. Errors caused by the intensity variations will appear as phase errors occurring at the same frequency as the fringes. It will be shown that this latter error is the dominant source of error in the LCPDI, and the former is negligible. This negligible phase error caused by phase shifting a convergent beam is consistent with the qualifications stated in Section

5.1.1, namely, that the path length through the liquid crystal layer can be considered constant for all angles of incidence.

The first requirement, that $\Delta\phi_{j+1}(x,y) - \Delta\phi_j(x,y) = \beta$, clearly can not hold for each pixel because $(n_{LC})_j$ is a constant across the entire layer and $L(x,y)$ is not a constant.

Therefore, the expression is in fact:

$$\Delta\phi_{j+1}(x,y) - \Delta\phi_j(x,y) = \beta - \varepsilon(x,y) \quad (19)$$

where $\varepsilon(x,y)$ represents the phase stepping error at pixel (x,y) . This error arises directly from the geometry described in Section 5.1.1 and is given by:

$$\varepsilon(x,y) = \beta \{1 - 1/\cos[\alpha(x,y)]\} \quad (20)$$

Since there is an inherent error in the phase steps, Hariharan's 5-frame algorithm³⁵ is useful for minimizing the final measurement error. Five phase values are required with the following sequence:

$$\Delta\phi = -2\beta - \varepsilon, \quad -\beta - \varepsilon, \quad -\varepsilon, \quad \beta - \varepsilon, \quad 2\beta - \varepsilon \quad (20)$$

The measurement error from phase shifting a convergent beam will then be:³⁵

$$W(x,y) - W_{meas}(x,y) = \frac{\varepsilon(x,y)^2}{4} \sin[2W(x,y)] \quad (21)$$

As previously described, the error ε is generally quite small, and so the measurement error is also negligible.

Another, more serious violation of the assumptions is the variation of the object beam intensity from frame to frame. It will be shown that this effect is caused by rotation of the dye molecules, and that the variation is substantial. Therefore the standard algorithms must be modified to reduce errors caused by this effect.

5.3.2 Algorithm modification

If the object beam intensity can be determined independently, then the algorithms can be modified in two ways. The first is to solve for the phase using the object beam intensity distributions explicitly; the second is to simply normalize each interferogram by its corresponding object beam intensity distribution. The latter method works best if the object beam intensity is much stronger than the reference beam.

The first way to calculate the wavefront phase ϕ is to use the following equation:

$$\tan(\phi) = \left(\frac{\Delta I_3 - \Delta I_1}{\Delta I_0 + \Delta I_4 - 2\Delta I_2} \right) \left[\frac{\sqrt{I_0^{\text{obj}}} + \sqrt{I_4^{\text{obj}}} + 2\sqrt{I_2^{\text{obj}}}}{\sqrt{I_3^{\text{obj}}} + \sqrt{I_1^{\text{obj}}}} \right] \quad (22)$$

where $I_j^{\text{obj}} = I_j^{\text{obj}}(x, y)$, the j^{th} object beam intensity distribution, and $\Delta I_j = I_j - I_j^{\text{obj}}$. This equation is exact, provided that the reference beam intensity remains constant from frame to frame.

For the second compensation method, each interferogram I_j is divided by the appropriate normalization frame, then used in the 5-frame algorithm as follows:

$$\tan(\phi) = \frac{2 \left(\frac{I_3}{I_3^{\text{obj}}} - \frac{I_1}{I_1^{\text{obj}}} \right)}{\left(\frac{I_0}{I_0^{\text{obj}}} + \frac{I_4}{I_4^{\text{obj}}} - 2 \frac{I_2}{I_2^{\text{obj}}} \right)} \quad (23)$$

This equation is not exact, and works best if $I_j^{\text{obj}} \gg I_j^{\text{ref}}$ so that $I_j^{\text{obj}} + I_j^{\text{ref}}$ is approximately equal to I_j^{obj} .

6. LCPDI DESIGN

The LCPDI is shown schematically in Figure 6.1. Nematic liquid crystals (LC) are sandwiched between two glass plates (G). Nine micron diameter cylindrical rods (R) are placed at the edges of the plates to serve as spacers. Transparent plastic microspheres (M), nominally 9 microns in diameter, are scattered throughout the liquid crystal layer. Each microsphere replaces a small volume of liquid crystals as the filler between the glass plates.

Dye is added to the liquid crystals to attenuate the object beam to roughly the same intensity as the reference beam. This improves the fringe contrast, but the dye molecules rotate with the liquid crystal molecules causing an unwanted intensity modulation when the phase is shifted.

The glass plates in the LCPDI are prepared so that the nematic liquid crystals are homogeneously aligned as described in Section 5.2. Transparent electrodes (E) are deposited on plates' inner surfaces, and leads (L) are soldered onto the electrodes so that an alternating current can be applied across the liquid crystal. When the field is applied, the dipoles realign themselves so that they rotate away from the plates. Most of the molecules realign themselves in this way, but surface effects prevent reorientation of the molecules immediately next to the glass walls.

The birefringent liquid crystal is uniaxial. Light polarized parallel to the director sees the extraordinary refractive index n_e ; the perpendicular polarization sees the ordinary index n_o . Therefore, for incident light polarized parallel to the glass grooves, the refractive index of the liquid crystal layer will be n_e when the applied electric field strength is below the threshold required for the Freedericksz transition. As the amplitude of the voltage

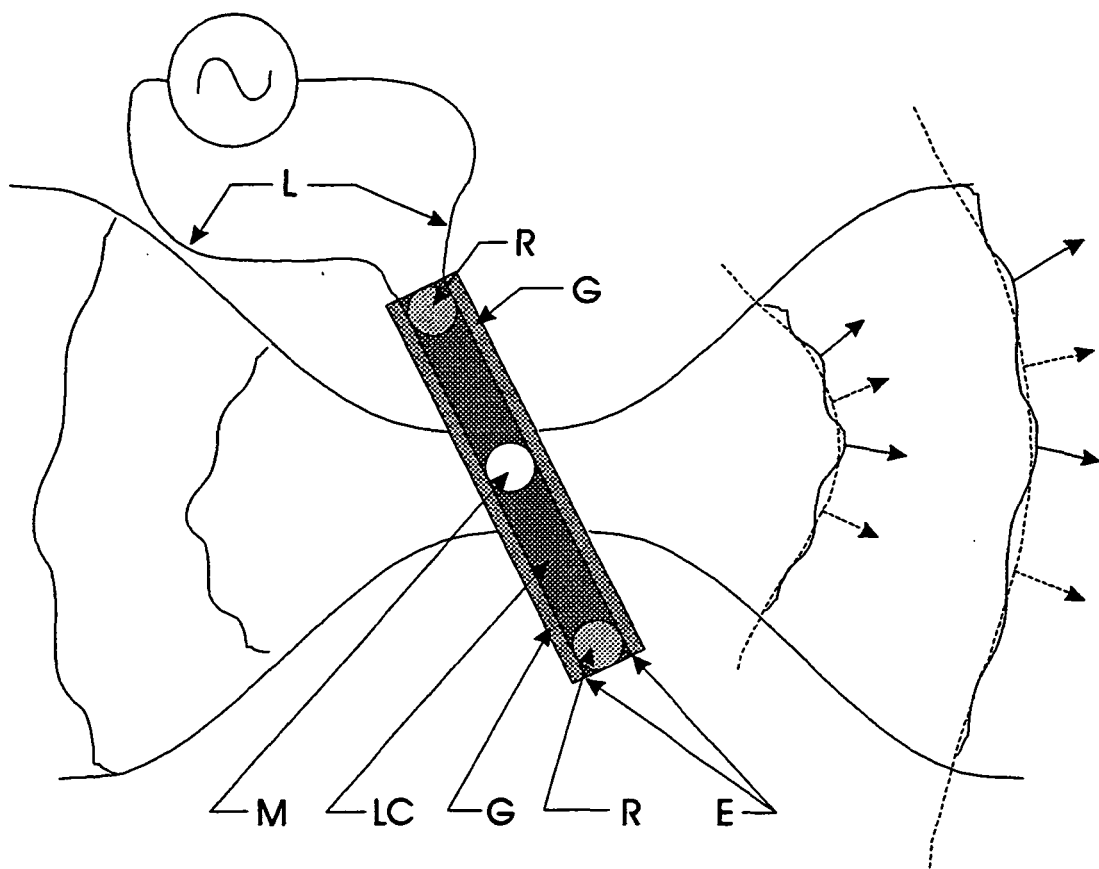


FIGURE 6.1, Liquid crystal point diffraction interferometer filter schematic.

Dashed lines indicate reference wave, solid lines indicate object wave.

increases to the saturation voltage, the molecules will realign themselves until they are perpendicular to the walls. The index of refraction at that point will be n_0 . The refractive index will monotonically vary between the two extremes at each intermediate electric field amplitude.

This refractive index modulation shifts the optical phase of light passing through the liquid crystal because of the relationship between phase and index:

$$\phi = \frac{2\pi}{\lambda} L n + \phi_0 \quad (24)$$

where L is the physical path length through the liquid crystal, λ is the wavelength of the incident light, and ϕ_0 is an arbitrary constant phase.

The LCPDI is tilted about the horizontal axis to minimize secondary fringes caused by multiple reflections from the glass plates. Anti-reflection coatings on each glass surface can be used in place of this tilt. The LCPDI itself introduces aberrations into the interferograms because the filter is a tilted, plane parallel plate placed in a converging beam. These aberrations must be subtracted from the measured wavefront. This correction will occur automatically if the device is used to measure an initial wavefront subtracted from an altered wavefront such as is the case in fluid studies.

6.1 Design parameters

The most important parameters to consider are the thickness and attenuation of the liquid crystal layer. The thickness needs to be large enough to ensure a wide range of phase control, but, since the microsphere diameter must be nominally the same as the thickness, this value must be small enough to provide good fringe contrast for reasonable f-numbers.

The attenuation must be chosen to complement the microsphere diameter and the expected amount of aberration.

6.1.1 Phase control

The thickness of the liquid crystal layer must be chosen to provide the required phase shift Φ between fully parallel and fully perpendicular molecule alignment. Therefore

$$t > \frac{\Phi}{2\pi} \frac{\lambda}{\Delta n} \quad (25)$$

where t is the liquid crystal layer thickness and $\Delta n = n_e - n_o$. The layer thickness must be greater than this value, not equal to it, because wall effects preclude full realignment of the liquid crystal molecules.

Since the microsphere diameter must be nearly equal to the liquid crystal layer thickness, larger values for Δn will permit the use of smaller microspheres, allowing good performance for fast (low f-number) optical systems.

6.1.2 Amplitude control

As described in Section 5.1.2, the microsphere diameter should be less than the Airy disk radius produced by an unaberrated optic to ensure a good approximation to a spherical reference beam. That is,

$$D_{\text{microsphere}} \leq 1.22 \lambda f \# \quad (26)$$

However, the microsphere diameter must also be approximately equal to the liquid crystal layer thickness to ensure no phase modulation in the reference beam. Therefore,

$$D_{\text{microsphere}} \approx t \quad (27)$$

where t is given by Equation (25). The optimum speed of the system optics can be found from combining these two equations:

$$f\# \geq \frac{t}{1.22 \lambda} \quad (28)$$

The optical density of the dye is chosen to attenuate the object beam to roughly the same intensity as the reference beam. For an ideal system with the microsphere centered on the focused spot, the diffracted beam will contain one-half of the energy in the Airy disk. Since the central disk contains about 84% of the total energy of the unaberrated beam, the intensity of the reference beam will be about one-quarter of this, or 21% of the incident intensity, leaving about 79% for the object beam. An optical density of -0.58 will produce the required object beam attenuation.

However, this calculation assumes no aberrations in the beam. The spot size will be larger if aberrations are present, allowing less light in the reference beam and therefore requiring more object beam attenuation. Also, if optics faster than recommended for the microsphere size are used, the LCPDI can be translated along the optic axis to increase the diameter D_{spot} of the focused Gaussian beam:³⁶

$$D_{spot} = 2 \sqrt{W_0^2 + \frac{z\lambda}{\pi}} \quad (29)$$

where W_0 is the beam waist radius at the focal point and z is the distance of the LCPDI from the focal point.

6.2 Circuit design

Phase shifting is accomplished by varying the amplitude of an alternating current applied across the liquid crystals. The applied voltage must have no DC component that would permanently distort the liquid crystals. A circuit was built based on an Exar XR2206 sine

wave generator integrated circuit chip. An LM310N operational amplifier was added to filter out the DC component. The circuit is shown schematically in Figure 6.2. The circuit produces a 5 kHz sine wave whose amplitude can be varied between 0 and 5 VAC.

A DC voltage was used as an input to the circuit in order to vary the amplitude of the generated AC signal. This DC input was generated by a digital-to-analog converter in an SR530 lock-in amplifier, and computer controlled over an IEEE-488 communications bus. This permits computer coordination of the phase stepping and image acquisition.

6.3 System design

A schematic of the LCPDI system is shown in Figure 6.3. The system consists of a laser (LASER), collimating optics (COLL), horizontal polarizer (P), test object (OBJ), focusing lens (L1), LCPDI plate (LCPDI), viewing screen (SCR), camera (CAM), frame grabber (FG), computer (COMP), programmable sine-wave generator (SINE GEN), and data transfer bus (GPIB).

The camera and phase-stepping electronics are synchronized by a computer code that communicates to the required elements over the GPIB bus. This code must be tailored to the specific camera used.

Additional system considerations include temperature control and vibration control. The refractive index of the liquid crystals depends roughly linearly with temperature, with a slope of about $-0.0014 \text{ } ^\circ\text{C}^{-1}$ over the range $0 - 38^\circ\text{C}$. To keep Δn within 1% of its value, the temperature of the LCPDI should be maintained within $2 \text{ } ^\circ\text{C}$. Also, although the common-path design makes this interferometer more stable than most, vibrations of the

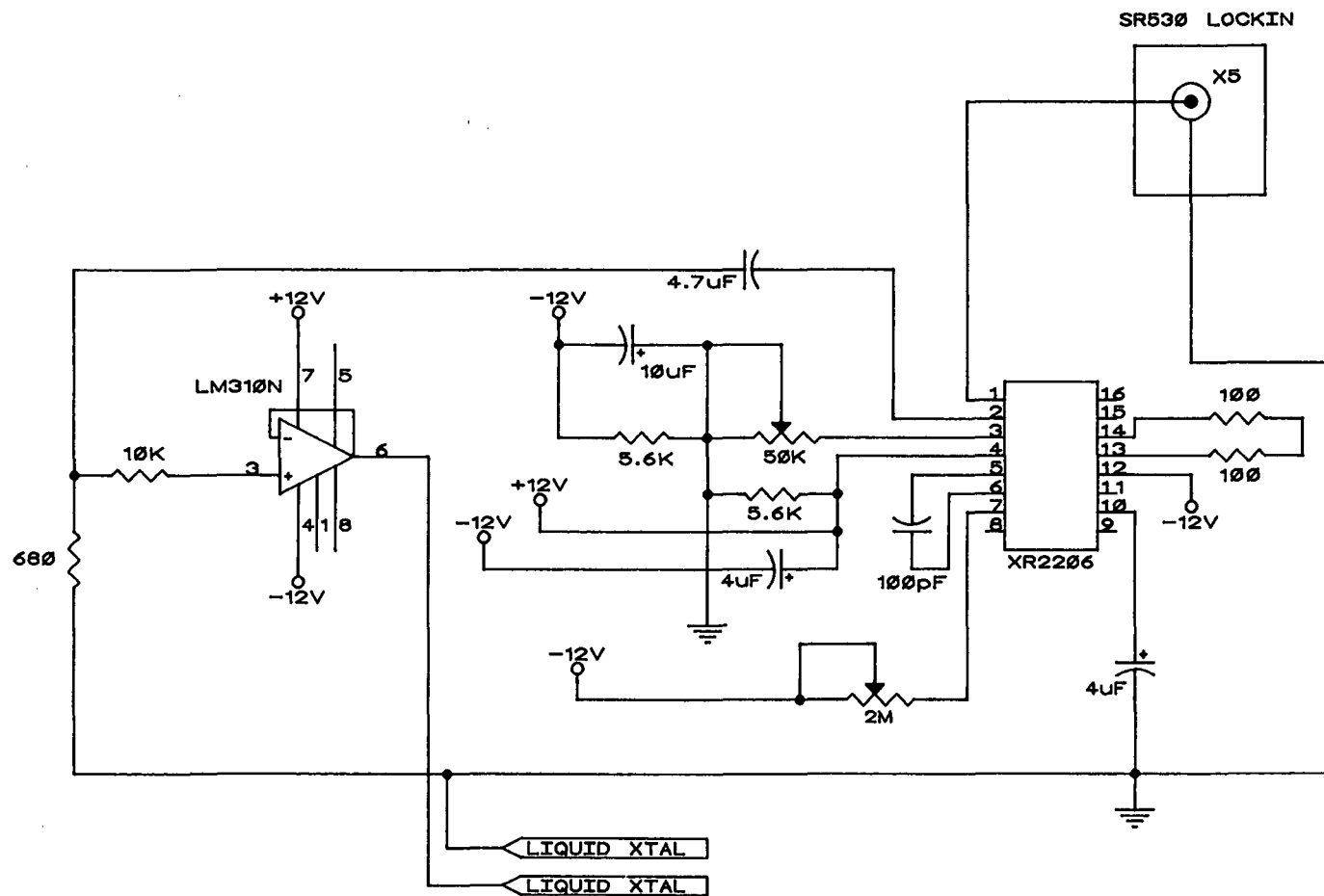


FIGURE 6.2, Electronic circuit for phase control.

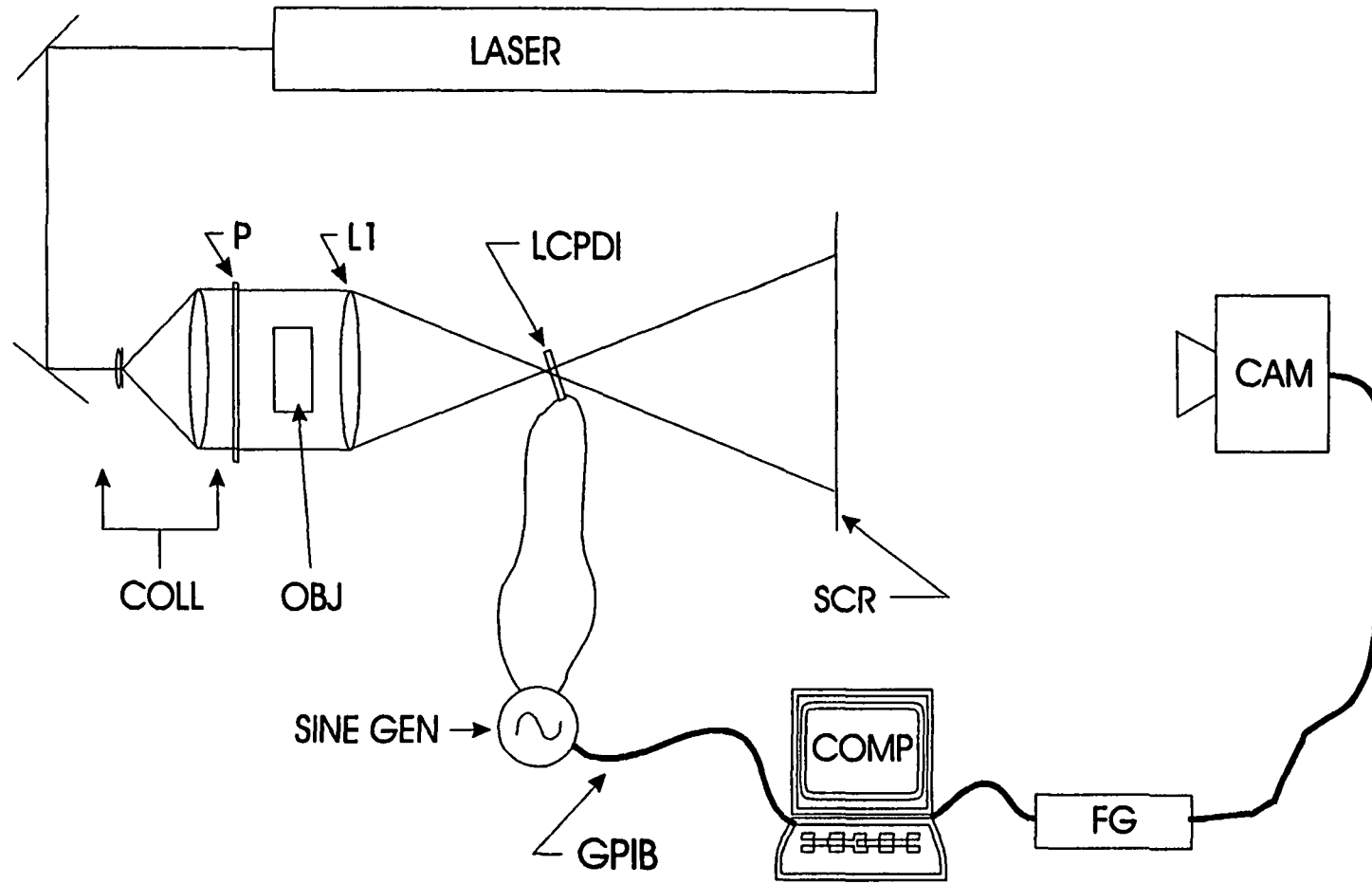


FIGURE 6.3, Liquid crystal point diffraction interferometer system schematic.

focusing lens, LCPDI, viewing screen and camera should still be minimized.

Typically, nematic liquid crystals have response times of 10 to 100 milliseconds, but these values are limited by the time required to restore the liquid crystal molecules to their relaxed state. This consideration is important for amplitude modulators, but the LCPDI requires switching from one intermediate state to another. Electrically driving the molecular orientation is much faster than waiting for full relaxation; typical response times for this process are only 0.5 - 2 milliseconds, and perhaps as fast as 10 - 50 microseconds.³⁷ No attempt was made to increase the data acquisition speed for this dissertation.

7. PHYSICAL DESCRIPTION

7.1 Materials

Merck E7 nematic liquid crystals were selected for their ability to hold dye and for their large difference between the ordinary and extraordinary refractive indices. The ordinary and extraordinary refractive indices are 1.5305 and 1.7718, respectively, at 514.5 nm and 20 °C. These values are obtained by linearly interpolating the manufacturer's data.

The dye chosen was designated M-370; it's a 4% solution of ZLI-1840. Its optical density is 1.4 when the dye molecules are oriented parallel to the incident light polarization. This is about 2.4 times darker than the ideal case described in Section 6.1.2. The high optical density was chosen to produce good contrast interferograms even for highly aberrated beams, such as those expected in fluid measurements.

The glass plates were coated with transparent Indium Tin Oxide electrodes. A thin polyamide plastic layer was used for initial molecular alignment as described in Section 5.2. The microspheres are optically clear plastic, and the micro cylinders are quartz.

7.2 Dimensions

The difference between the ordinary and extraordinary refractive indices of the chosen liquid crystal is 0.2414. This very large birefringence permits a 2π phase change using a very thin liquid crystal layer. If edge effects were not important, Equation (25) shows that a 2.1 micron layer would be sufficient. A 4.3 micron layer would permit a full 4π phase change, allowing the use of 6-step algorithms. However, edge effects reduce the full range of phase delay.³⁸ The thickness was therefore set using 9 micron cylindrical rods, leaving a comfortable safety margin for a full 4π phase change. The microsphere

diameters were chosen to be nominally 8.7 microns. Equation (28) shows that this permits optimum performance at about f/15.

Glass plates nominally 0.5 millimeter thick and 3.0 x 3.5 centimeter were used, and the liquid crystal layer filled the central 3.0 x 2.5 centimeter area. The plates were offset from each other by about 2 millimeter to allow soldering room for the leads onto the electrodes.

7.3 Optics

The diverging lens in the collimating optics was selected so that the diverging beam greatly overfilled the collimating lens. This ensures that the illumination through the test object and on the focusing lens has an intensity distribution that is nearly constant. This is the condition that was assumed in Section 5.1.2.

The LCPDI was set up using a 400 millimeter lens stopped down to 65 millimeter, producing an f/6.18 beam. This system is faster than the optimum f/15 described in the previous section, so the LCPDI was defocused slightly. Equation (29) shows that a 0.47 millimeter shift from the focal point along the optic axis increases the beam diameter to roughly twice the microsphere diameter.

7.4 Electronics

A voltage sequence ranging from 1.0 to 1.7 VAC is required to produce a sequence of six $\pi/2$ radian phase steps. A circuit was built to generate this signal (Figure 6.2), but commercially available function generators are also available.

The liquid crystal manufacturer recommends that a relatively high voltage, about 15 VAC, be applied across the liquid crystal layer before each use to overcome the initial inertia in the molecular response. The home-built circuit was limited to 5 VAC, so a high voltage amplifier was used for amplification.

7.5 Operation

7.5.1 Alignment

The optical alignment of the LCPDI is the same as that for a conventional point diffraction interferometer. Collimated light passes through the test object, then is focused onto or near the PDI plate. Rather than centering the focused spot onto the pinhole of the conventional PDI, though, the spot must be centered near a microsphere, and the chosen microsphere must not be near other microspheres whose diffraction patterns would interfere. Individual microsphere locations are easily seen by greatly defocusing the LCPDI and looking at the viewing screen. The LCPDI can then be translated left-to-right and up-and-down until an isolated, circular microsphere is found. Then the LCPDI is focused to ensure that the selected microsphere produces high contrast, circular fringes and that neighboring microspheres are not interfering. Figure 7.1 shows a sequence of images showing the microsphere identification process. The images are recorded from the viewing screen as the LCPDI is first defocused, then focused onto a "good" microsphere.

7.5.2 Phase stepping calibration

Phase stepping calibration was performed manually. A sharp pointer was placed in the center of a dark interference fringe on a viewing screen behind the LCPDI after the beam had been focused near a good microsphere. The amplitude of the applied voltage was increased from 0.5 VAC in increments of 0.5 VAC until the fringes shifted. It was found that the Freederickz transition occurred between 1.0 and 1.5 VAC. Voltage steps were

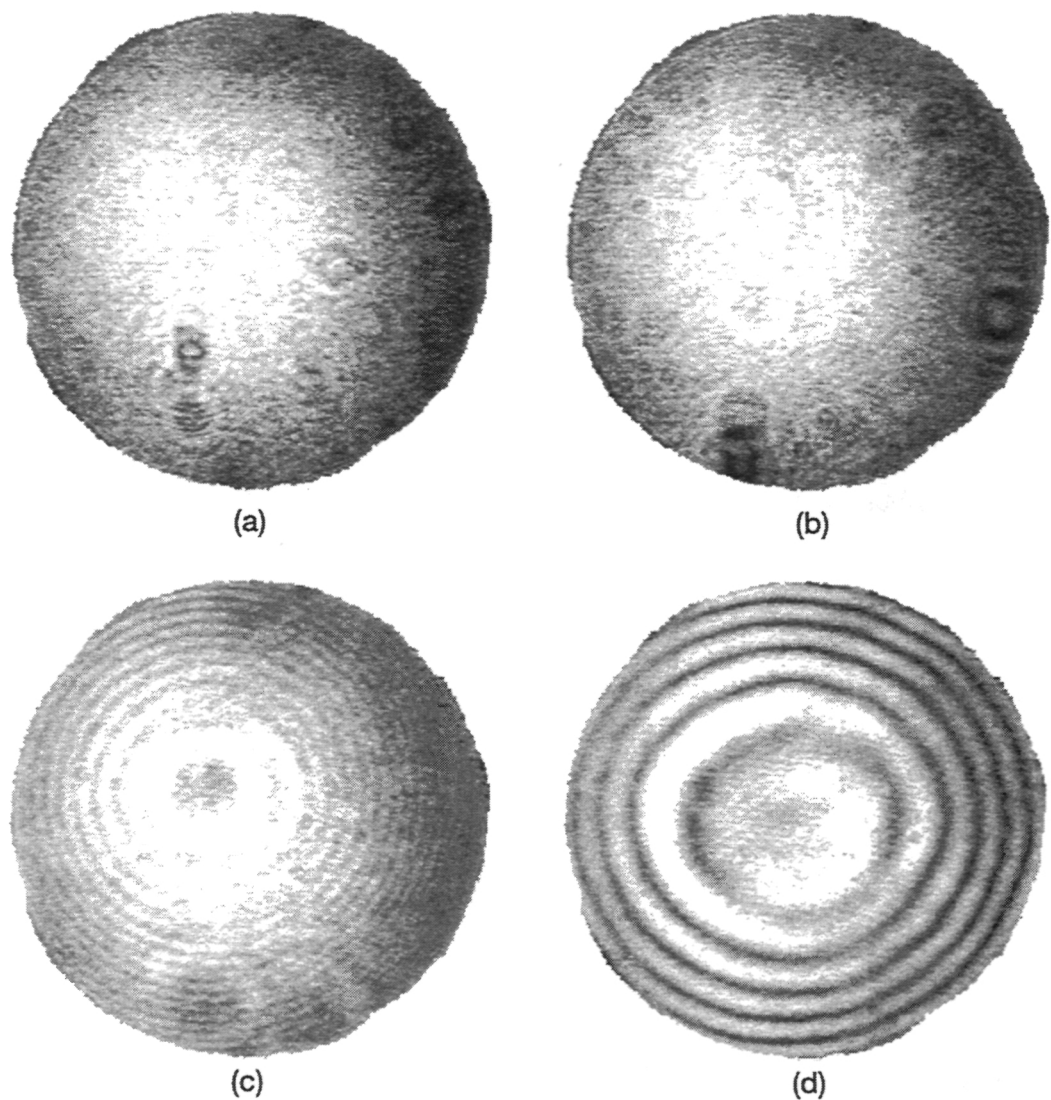


FIGURE 7.1, Image plane for greatly defocused LCPDI showing microspheres.

Relative defocus positions: (a) 7.85 mm, (b) 6.42 mm, (c) 1.27 mm, (d) 0 mm.

applied in this range in finer and finer increments until it was determined that 1.05 VAC was the threshold voltage, and therefore an appropriate value for the first phase step. The amplitude of the voltage was then increased and the fringe behind the pointer was observed. By trial and error, the appropriate voltages were found to step the fringe by ninety degree increments. Although this calibration procedure is tedious, it only needs to be performed once for a given liquid crystal device. Recalibration is not required after system realignment, test object changes, moving to a different microsphere, or moderately changing the tilt angle.

7.5.3 Object beam intensity determination

In order to use the modified phase extraction algorithms described in Section 5.3.2, the intensity distribution of the object beam must be obtained. This is not trivial because the object and reference beams are difficult to separate in a common-path interferometer.

There are four ways that this information can be obtained. The first is from an intensity calibration curve, which will be described in the following section. The peak values of the object beams at each phase step can be obtained from the calibration curve. The shape of the distribution must be estimated though; a Gaussian distribution is a reasonable assumption, but there is little information available for choosing the Gaussian width.

The second way to get the object beam intensity is to translate the LCPDI perpendicularly to the optic axis to let the focused beam pass through the instrument without hitting a microsphere. No reference beam will be generated, so the light incident on the viewing screen is from the object beam alone. This light can be recorded for each of the phase steps.

The third way is to fit two-dimensional polynomials to the object beam distributions obtained by translating the LCPDI, rather than using the recorded intensity distributions directly. This effectively smoothes out speckles and imperfections in the viewing screen.

The final way to get the data is to fit a polynomial to each interferogram, rather than each object beam distribution. This yields the average intensity across the detector; the incoherent sum between the object and reference beams. This is more appropriate for use in Equation 23 than the object beam alone. This technique has the advantage that no calibration is necessary, the LCPDI need not be moved, and fewer frames of data are required.

8. PERFORMANCE

8.1 Phase and Amplitude Modulation

The liquid crystal cell was placed in a collimated beam of light in one arm of a Twyman-Green interferometer to calibrate the phase shift of the on-axis beam. The LCPDI was perpendicular to the optic axis. A photodetector was placed in a wide fringe and the detector's output was recorded as the amplitude of the applied voltage was varied. A plot of detected intensity versus applied voltage is shown in Figure 8.1. From this plot the electric field amplitude values for ninety degree phase shifts were chosen to be 1.04, 1.25, 1.35, 1.45, and 1.55 volts AC.

The absorptance of the liquid crystal layer was calibrated by passing a horizontally polarized collimated beam through the LCPDI and recording the transmitted intensity as the voltage was varied across the electrodes. The LCPDI was tilted by 27° relative to the optic axis, and the relaxed liquid crystal molecules were parallel to the incident polarization. The intensity as a function of applied voltage is plotted in Figure 8.2. The plot shows that the absorption of the dye varies strongly with the orientation of the liquid crystals, with the attenuation decreasing as the molecules are rotated farther from their initial state. This behavior is the same as that observed by Heilmeier et. al.;³⁹ they demonstrated that the attenuation variation is caused by asymmetric dye molecules rotating with the liquid crystals.

The variation shown in the plot is non-linear but is repeatable; two sequences of 100 measurements are shown superimposed on each other. The lower horizontal line represents 100 sequential measurements of the transmitted intensity with no applied voltage; the upper horizontal line is 100 points of measured intensity with the LCPDI completely removed from the beam. The lower line is nearly flat, indicating that the

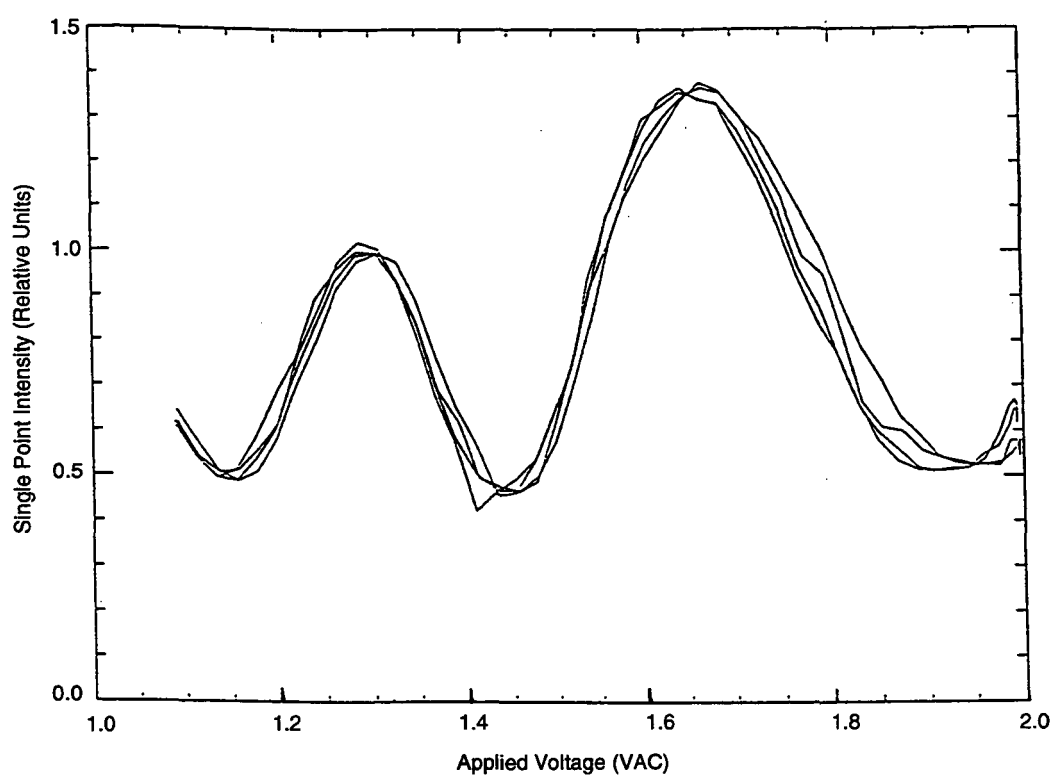


FIGURE 8.1, Liquid crystal phase calibration curve.

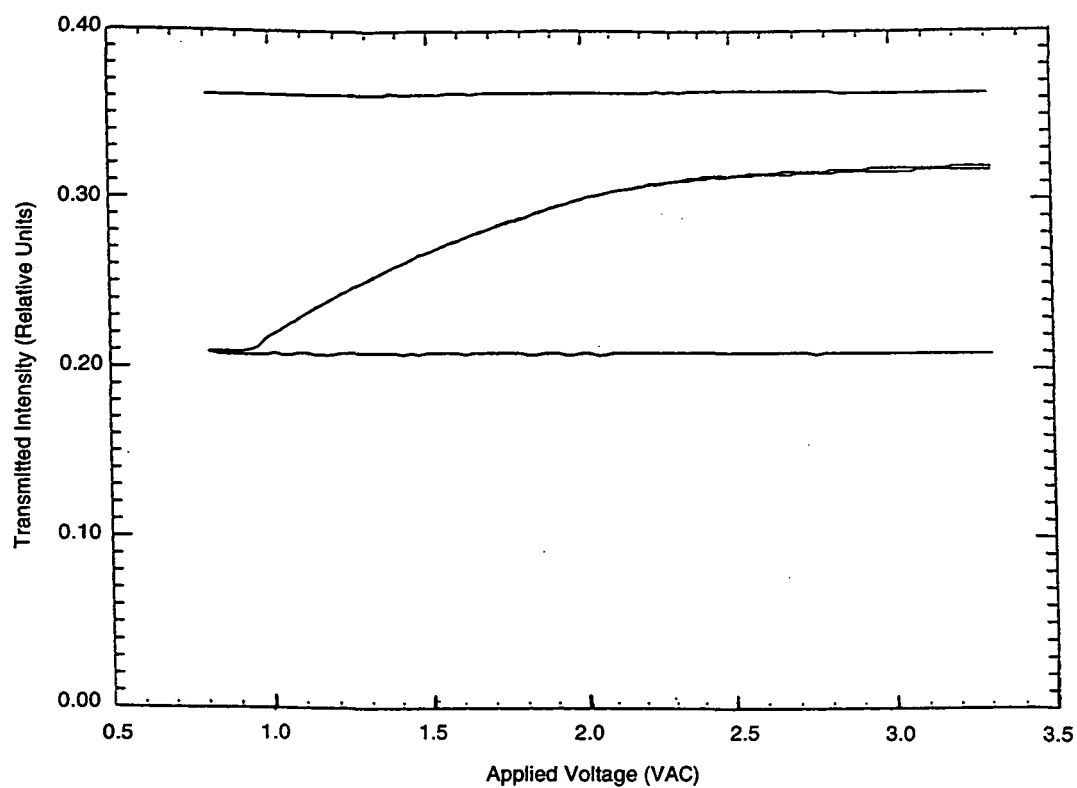


FIGURE 8.2, Liquid crystal intensity calibration curve.

intensity through the LCPDI is constant over time; slight deviations are caused by laser fluctuations as indicated by the upper line.

From this plot, the relative intensity of the object beam at each applied voltage can be determined. For the five voltages listed above, the relative intensities are: 0.21, 0.59, 0.74, 0.88, and 1.00, where the DC level is set to zero.

8.2 Accuracy

8.2.1 Focus shift measurement

8.2.1.1 Experimental apparatus

The optical system used for this experiment is shown schematically in Figure 6.3. An Argon ion laser operating in single-mode in the 514.5 nm line, equipped with a closed-loop controller for constant intensity operation and an opto-isolator to prevent back reflections feeding back into the laser cavity was used as the light source. The laser was operated at 50 mW, and a neutral density filter attenuated the beam so that only 2 mW was incident on the LCPDI. The collimating optics (COLL) consisted of a 40X microscope objective to expand the beam, a 10 micron pinhole to filter the beam, and finally, to collimate the beam, a 50 millimeter focal length Nikkor lens stopped down to a 16.2 millimeter diameter aperture was used. A linear polarizer (P) ensured that the collimated light was horizontally polarized. A 100 millimeter Cooke triplet lens (L1) brought the beam to a focus, forming an f/6.2 cone of light. Figure 8.3 shows an expanded view of the optical system near the LCPDI filter. The filter was mounted on a three-axis positioner placed near the focused spot and finely positioned using the method described in Section 7.5.1. A second horizontally oriented linear polarizer (P2) was placed behind the filter to remove depolarized light scattered from the liquid crystal molecules. A ground glass screen (SCR) placed 40 centimeter behind the focal spot

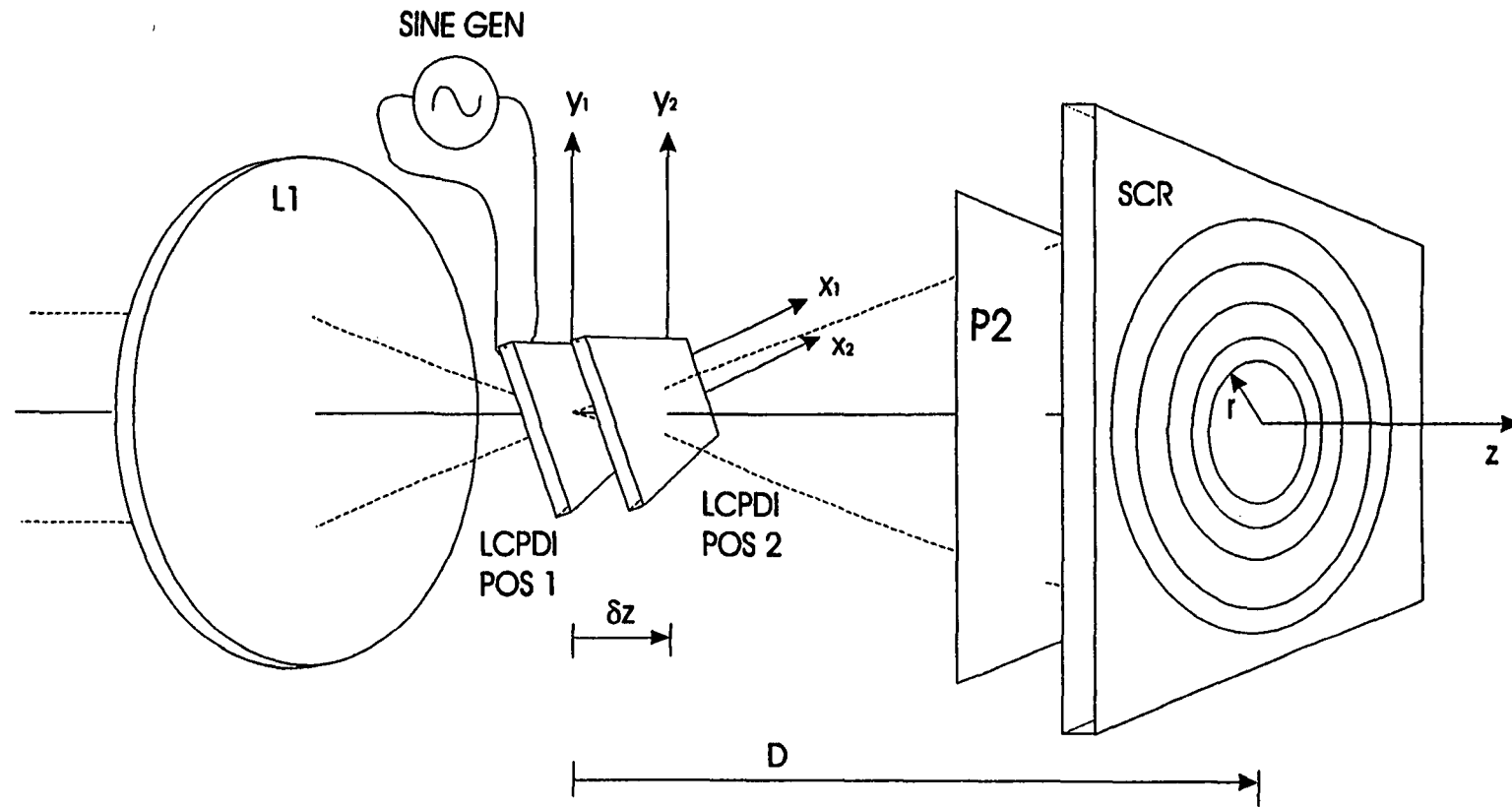


FIGURE 8.3, Optical configuration for defocus measurement.

rendered the interferogram visible, and a 50 millimeter Nikkor lens at f/2.8 imaged the interferogram onto a Videk Megaplus charge-coupled device camera (CAM). The detector plane was 66 centimeter behind the ground glass screen.

The camera was operated in low-resolution mode, producing 8-bit images with 640 x 480 pixels covering a screen area 64.8 x 48.6 millimeter. Each pixel measured 6.8 x 6.8 microns, spaced on 13.6 micron centers in both directions.

The LCPDI was tilted by about 20° to decrease multiple interference effects off the uncoated glass surfaces. The wires soldered to the electrodes were hooked up to the circuit described in Section 6.2.

8.2.1.2 Data acquisition

Phase shifts of $j\pi/2$ radians (where $j = 0, 1, 2, 3, 4$) are added to the object beam by applying a voltage sequence of 1.04, 1.25, 1.35, 1.45, 1.55 VAC using the circuit described in Section 6.2. The interferogram produced after each phase shift was recorded by the camera, then acquired and stored on a personal computer by an Epix 4Meg frame grabber.

To measure the intensity distribution of the object beam alone, the LCPDI plate was translated by 0.75 millimeter along the x1-axis (Figure 8.3) so that the focused beam did not pass through any microspheres. The light incident on the screen was recorded for each applied voltage.

The amount of defocus was then increased by moving the LCPDI along the optical axis by $\delta z = 0.34$ millimeter. Slight in-plane adjustments were made to center the new interference

pattern on the CCD. Again, the interferograms were recorded, and the LCPDI plate was translated to record the object beam alone. This amount of defocus changed the beam diameter on the plate from roughly 18 microns to about 23 microns, roughly a 30% change. The fringe contrast was, however, good at both positions.

8.2.1.3 Data reduction

The wavefronts for both positions of the LCPDI were computed using Hariharan's standard 5-frame algorithm on the raw interferograms. This algorithm was chosen because of its robustness in the presence of phase stepping error. The wavefront difference was obtained by subtracting the two calculated wavefronts.

Two-dimensional polynomials were fitted to the two calculated wavefronts, and the difference between these two polynomials was also found. This difference shows the underlying shape of the measured wavefront difference.

8.2.2 Theoretical calculation of focus shift

The difference in the optical phase between the wavefronts at each LCPDI position can be calculated from:

$$\Delta\phi_{th}(r, \delta z) = \frac{2\pi}{\lambda} \left\{ \sqrt{D^2 + r^2} - \sqrt{[(D - \delta z)^2 + r^2]} - \delta z \right\} \quad (30)$$

where D is the distance from the LCPDI to the ground glass viewing screen, δz is the axial distance between the two positions of the LCPDI, and r is the radial distance from the center of the interferogram.

8.2.3 Results

Figure 8.4 shows the wavefront difference computed using the standard 5-frame

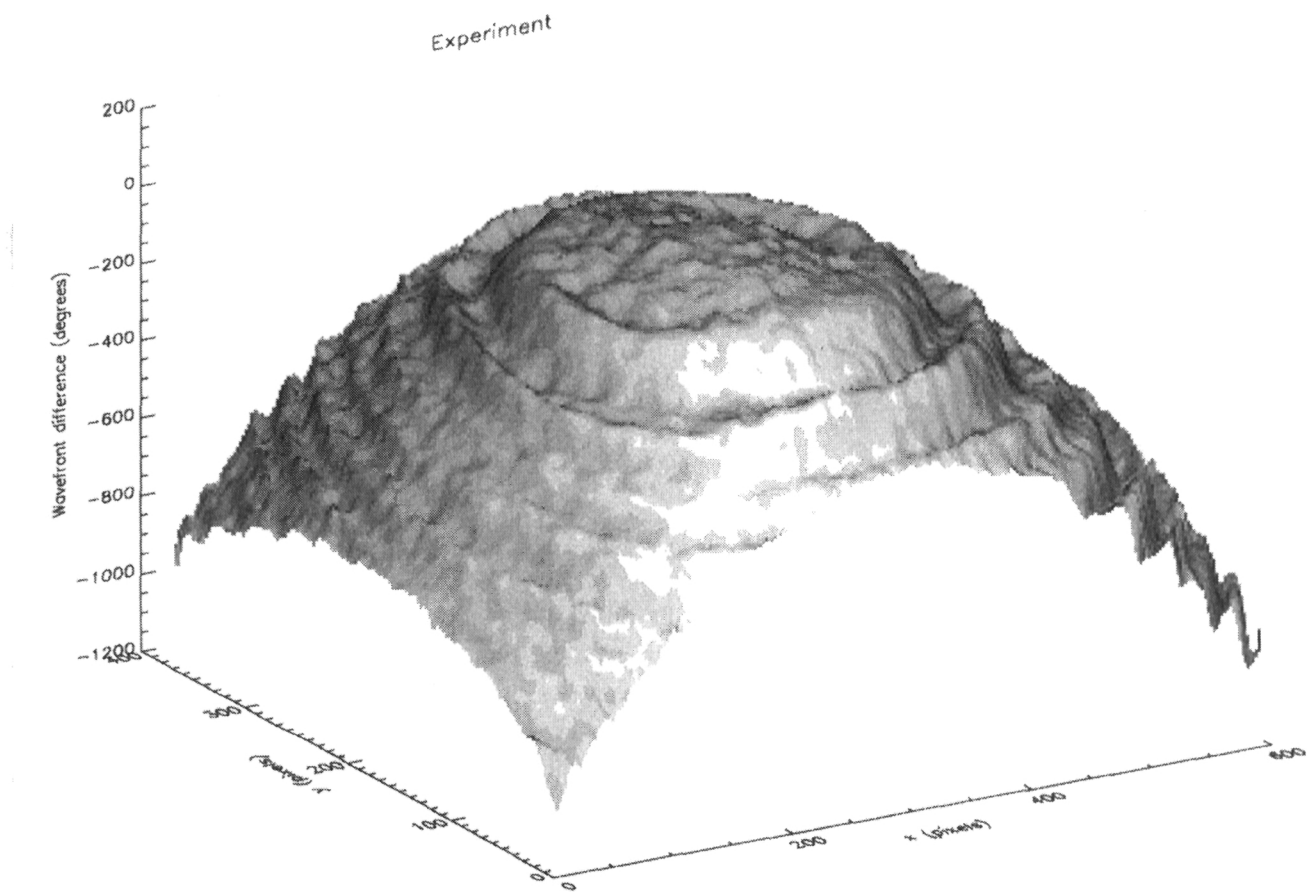


FIGURE 8.4, Wavefront difference measured with LCPDI.

algorithm. The shape is generally paraboloidal, but significant periodic error is present. Figure 8.5 shows a cross section of this data and the corresponding cross section of the wavefront difference found by using Equation (30). This plot shows that the underlying shapes of each of these curves are the same, and therefore the LCPDI is accurately measuring the wavefront difference, albeit with substantial periodic error. The cause of and methods for reducing this error are presented in the following sections.

8.3 Periodic error

8.3.1 Cause

It was stated in Section 5.3.1 that phase measurement errors occurring at the same frequency as the interference fringes are caused by intensity variations from frame to frame, and that these variations were caused by the dye molecules in the liquid crystal layer rotating with the applied voltage. To verify that the observed periodic measurement error can in fact be caused by this, a computer program was written to simulate the performance of the LCPDI in the presence of the known intensity variation with phase shift.

The software modeled each interferogram as the coherent sum between Gaussian object and reference functions. The width, peaks, and minimum values needed to describe these Gaussian functions are listed in Table 1. Random noise in the interferogram that appeared to be normally distributed was modeled by generating an array of normally distributed random numbers, scaling the array in x and y to model the size, and scaling the value of each array element to model the intensity. These parameters were combined to form the modeled object and reference beams using the following equations:

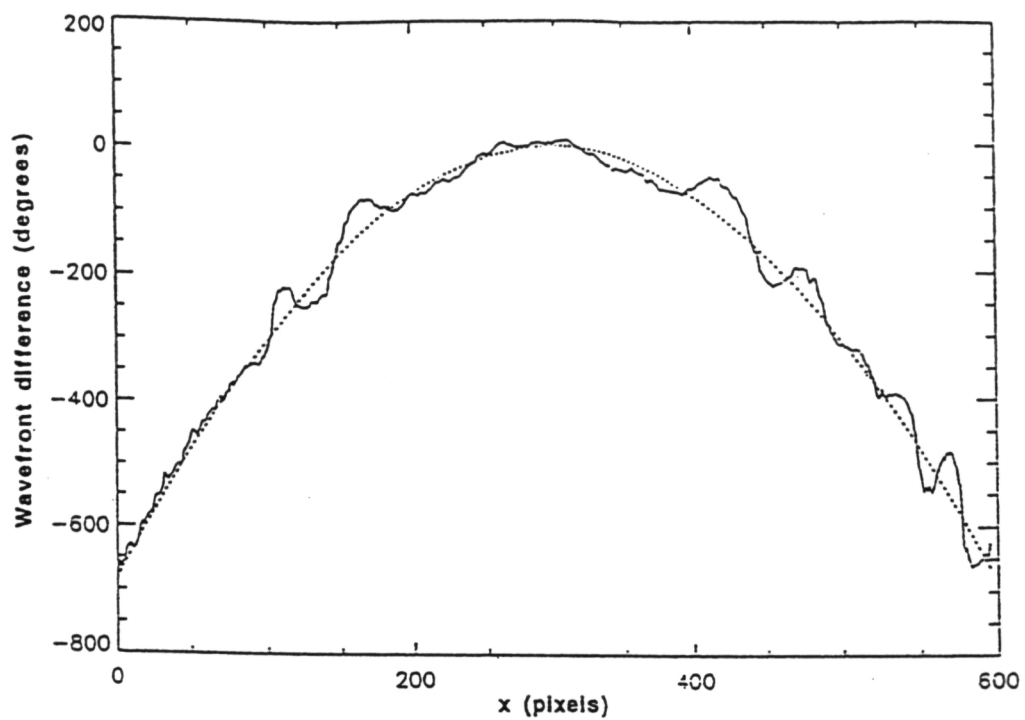


FIGURE 8.5, Cross-sections of wavefront difference, computed with the 5-frame algorithm and theoretical equation.

$$I^{ref}(x, y) = \bar{I}^{ref} \exp \left\{ - \left[\left(\frac{x}{\sigma} \right)^2 + \left(\frac{y}{\sigma_y} \right)^2 \right] \right\} + dc^{ref} \quad (31)$$

$$I_j^{obj}(x, y) = \alpha_j \left[\bar{I}^{obj} + N(0, 10) \right] \exp \left[- \left(\frac{x^2 + y^2}{\sigma^2} \right) \right] + dc^{obj} \quad (32)$$

where $N(0, 10)$ represents a normally distributed random variable with a mean value of zero and a standard deviation of 10.

Five interferograms were created for the two positions of the LCPDI in the defocus experiment by the coherent addition of the object and reference functions:

$$I_{n,j}(x, y) = I^{ref}(x, y) + I_j^{obj}(x, y) + 2\sqrt{I^{ref}(x, y)I_j^{obj}(x, y)} \cos[W_n(x, y) + \phi_j] \quad (33)$$

The subscript $n = 1, 2$ and denotes the two positions of the LCPDI shown in Figure 8.3. The wavefronts W_n were obtained by fitting sixth-order polynomials to the experimentally obtained wavefronts at LCPDI positions 1 and 2. The Gaussian beam width σ , the relative object intensities $\alpha_j \bar{I}^{obj}$, and the dc offset dc^{obj} were chosen iteratively so that the modeled object beam intensity distributions closely resembled each corresponding frame of experimental data. Note that the final ratios of the object beam intensities are nearly identical to the ratios obtained from the calibration curve in Section 8.1. The Gaussian width σ_y was chosen so that the overall intensity distribution of the interferograms resembled the experimental interferograms. The reference beam intensity \bar{I}^{ref} was selected to match the fringe visibility, and dc offset dc^{ref} was chosen to ensure that the reference beam remained non-zero. Normally distributed random noise was added to each simulated object beam; the mean value of the added noise was zero, the standard deviation was 10, and the noise had a characteristic length of 4 pixels.

The simulated wavefronts W_{sim_1} and W_{sim_2} were found using the 5-frame algorithm, and then the simulated wavefront difference is obtained from $\Delta W_{\text{sim}} = W_{\text{sim}_2} - W_{\text{sim}_1}$. This difference is shown in Figure 8.6. Comparison with Figure 8.4 shows that the simulated wavefront difference is virtually identical to the measured wavefront difference, indicating that all significant features of the LCPDI have been correctly modeled and that the source of the periodic measurement error is intensity variation in the object beam. Cross sections of the wavefront differences obtained from the simulation and the corresponding LCPDI data are shown in Figure 8.7, again showing excellent agreement. Since the object beam intensity used for the simulation is substantially larger than the reference beam intensity, the use of Equation (23) for phase extraction is justified.

8.3.2 Error reduction

Both approaches described in Section 5.3.2 were used to compensate for the intensity variation. Each frame of object beam intensity data was smoothed with a boxcar average over 25 pixels to decrease the randomly distributed noise and multiple beam interference effects in the frames. A two-dimensional sixth-order polynomial was fitted to each smoothed intensity frame to form normalization frames I_j^{obj} , where $j = 0, 1, 2, 3, 4$. The wavefronts at both LCPDI positions were calculated using Equations 22 and 23, and the differences taken to obtain the wavefront difference using both methods.

The wavefront differences computed from the two methods were compared, and very little difference was found. This is because the object beam was much stronger than the reference beam. The wavefront obtained with the LCPDI in the second position, calculated using Equation (22), is shown in Figure 8.8. Comparing this to the same wavefront calculated with the standard 5-frame algorithm shown in Figure 8.9, clearly the

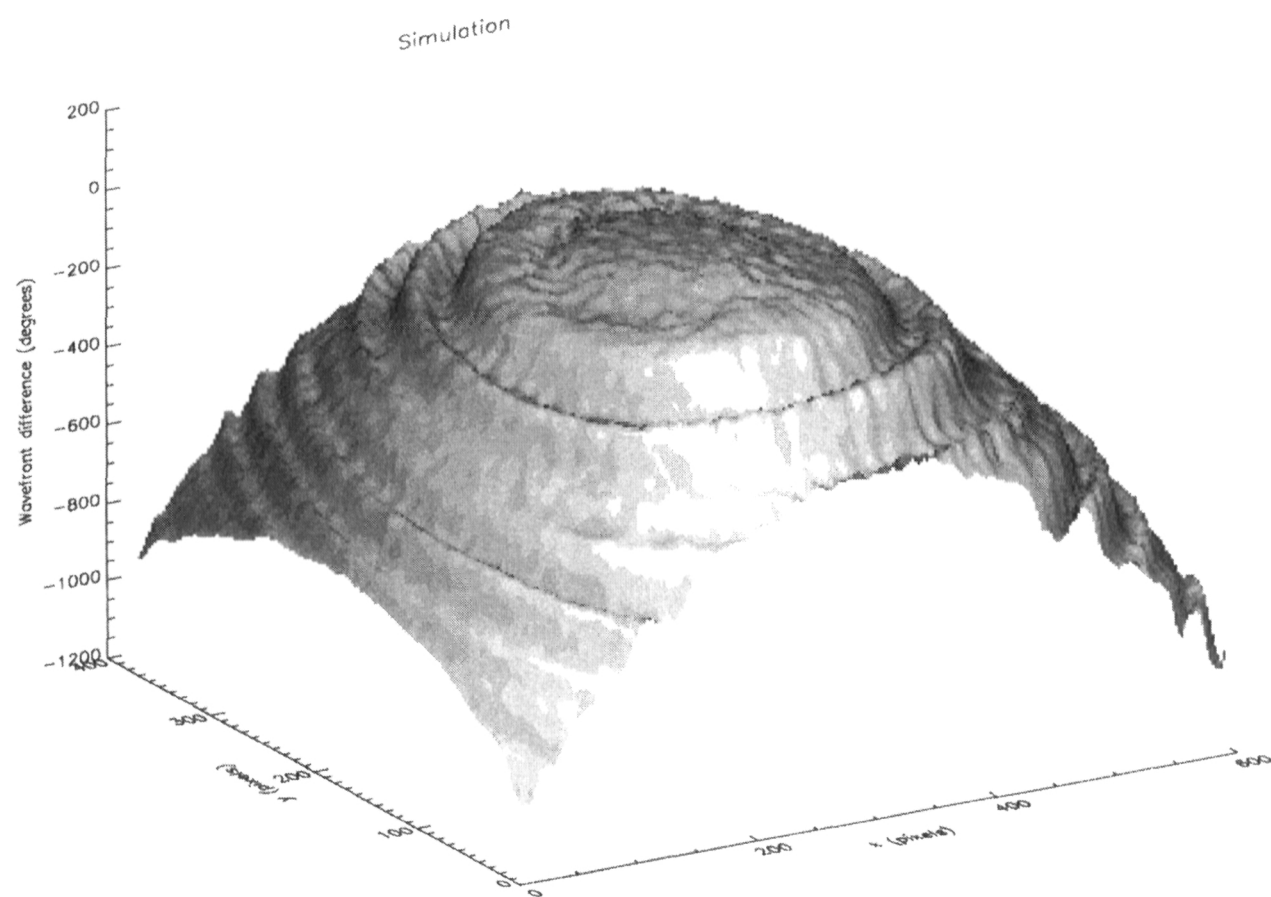


FIGURE 8.6. Wavefront difference obtained from computer simulation.

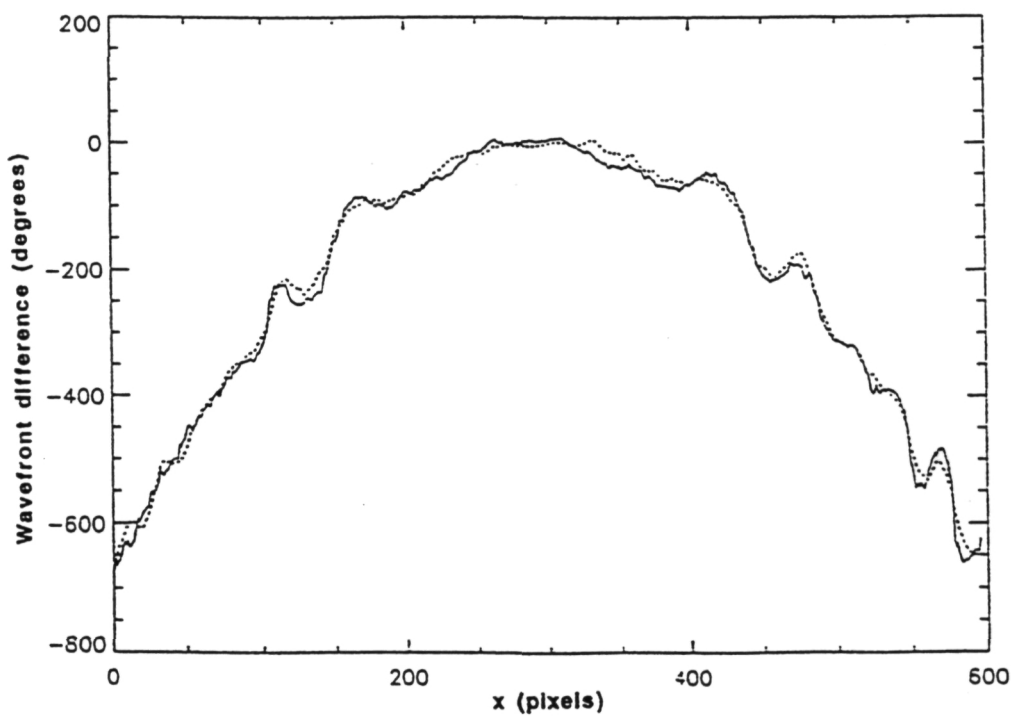


FIGURE 8.7, Cross-sections of wavefront difference, obtained from computer simulation and LCPDI data.

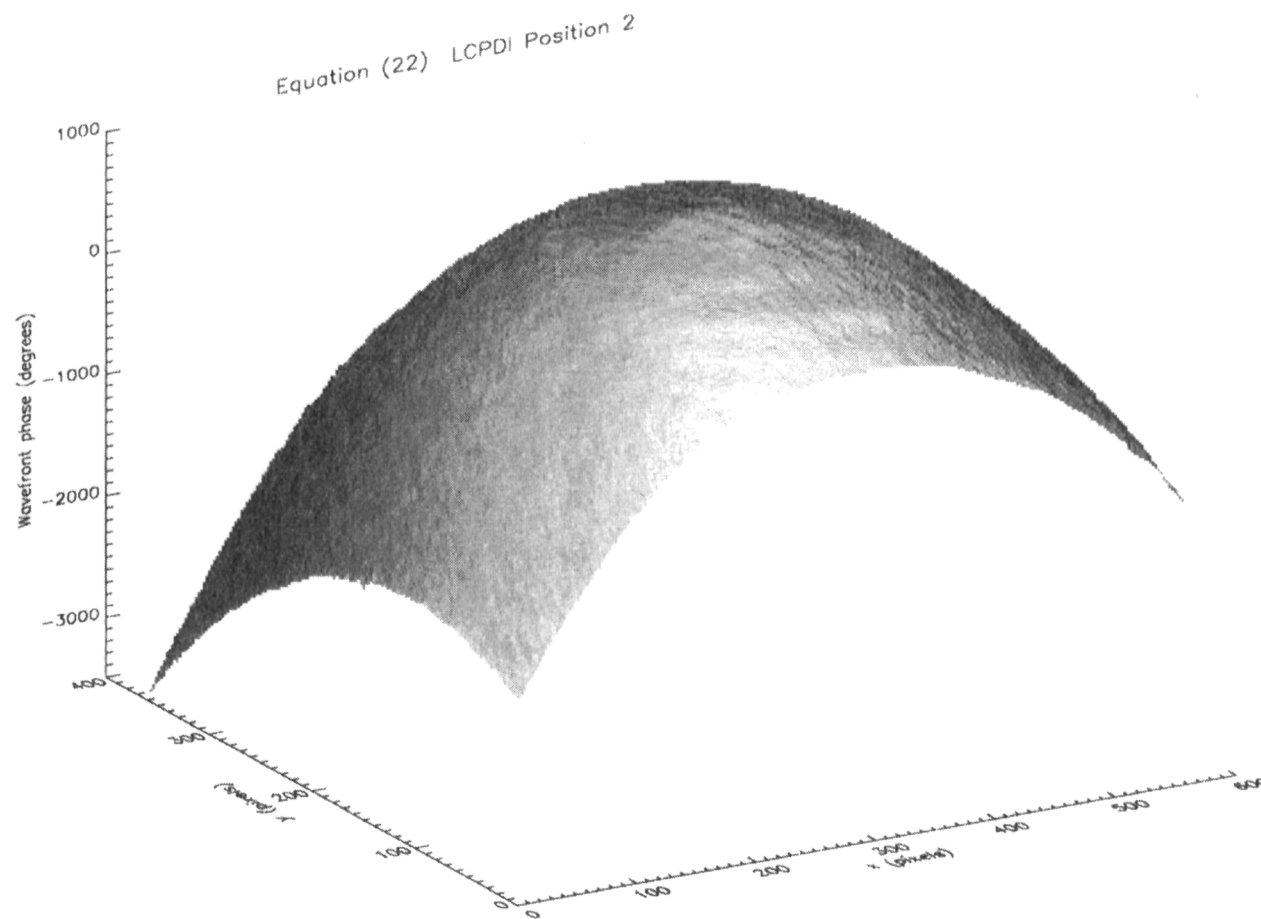


FIGURE 8.8, Wavefront measured at Position 2, computed with Equation (22).

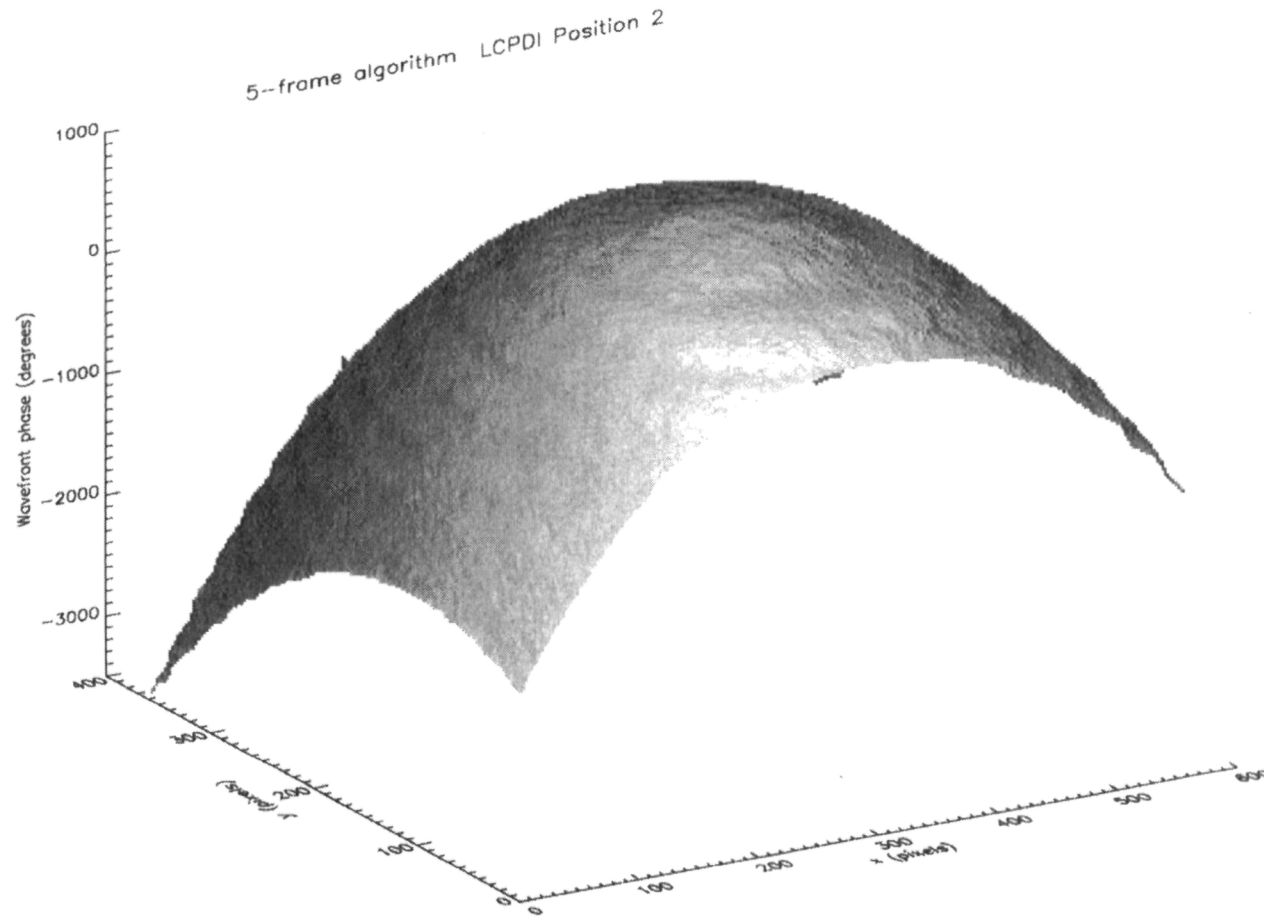


FIGURE 8.9, Wavefront measured at Position 2, computed with 5-frame algorithm.

modified algorithm is much better at reducing the periodic error.

Figure 8.10 shows horizontal cross sections from the wavefront differences computed using each of the methods described above together with the corresponding cross section from the theoretical wavefront difference calculated from Equation (23). It can be seen that in each case the wavefront difference is accurately measured. The standard deviations from the theoretical wavefront for each of the computed wavefront differences are 5.1, 25.4, 14.1, and 14.9 degrees for the wavefront differences computed from: polynomial fits to the wavefronts computed from the 5-frame algorithm, the 5-frame algorithm, Equation (22), and Equation (23), respectively. Equations (22) and (23) produce similar results and provide significant improvement over the standard 5-frame algorithm. The amount of periodic error is reduced by these intensity compensation algorithms but not eliminated. The frequency of the error is the same as the spatial frequency of the interferogram fringes, indicating that the intensity variations have not yet been completely compensated.

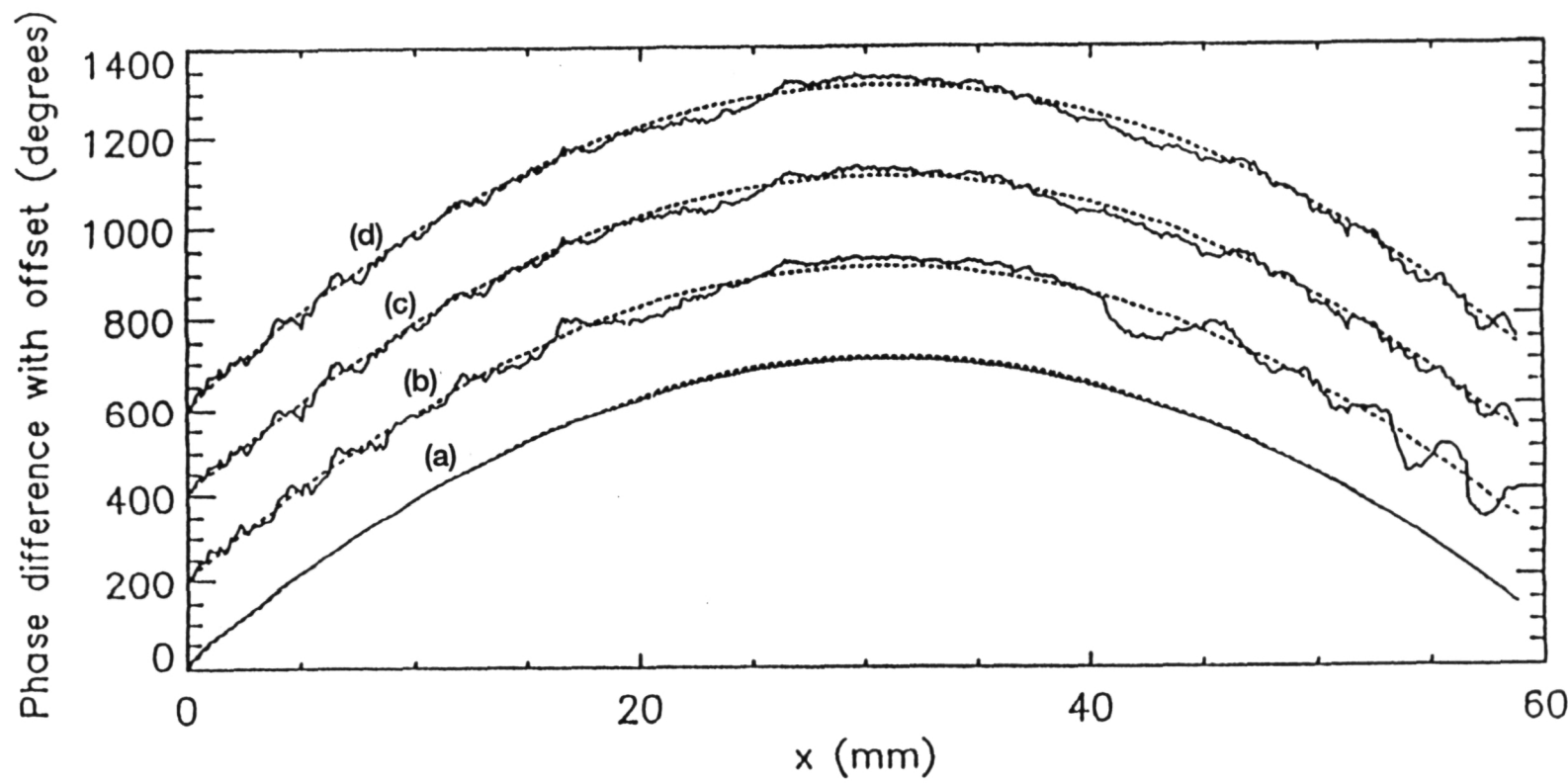


FIGURE 8.10, Cross sections of wavefront differences computed from (a) 2-D polynomial curve fits, (b) 5-frame algorithm, (c) Equation 22, and (d) Equation 23. Dashed lines indicate theoretical value.

9. APPLICATION: TEMPERATURE MEASUREMENT

Fluid scientists are interested in the mechanics of diffusion in the absence of gravity. It is hoped that these studies will lead to improved understanding of the fundamental processes of solidification, chemical transport, combustion, and turbulence, ultimately leading to better material processing systems, drug delivery, and engine designs. A typical experiment involves the suspension of a bubble or drop in oil. The diffusion across the boundary is studied as an oil property, such as temperature, is changed systematically. A standard piece of experimental equipment is a rectangular chamber filled with oil, with two temperature controlled sides. Windows in the other four sides allow observation of the oil. A syringe inserted into a small port allows the injection of a drop of fluorine or a bubble of air into the oil.

The LCPDI was used to measure the temperature distribution across the chamber, before the addition of a drop or a bubble. This experiment demonstrates the ability of the LCPDI to measure fluid properties of interest to microgravity researchers.

9.1 Experimental apparatus

The chamber used for this experiment was constructed of four Lexan double walls, each 45 x 45 x 60 millimeter. Circular fused silica windows were inserted in the center of two opposing walls to provide a high quality viewing port. The windows were 30 millimeter in diameter, 6 millimeter thick, and polished to a one-tenth wave finish.

The top and bottom of the chamber were hollow rectangular boxes made from anodized aluminum. A recirculating water bath was connected to each box, allowing water to pass through an external heating or cooling element and then through the box. The system could maintain a water temperature stability of 0.01 °C. However, the chamber was not

insulated, and variations in the ambient room temperature affected the temperature of the chamber surfaces. K-type thermocouples in the inner surfaces of the top and bottom chamber walls monitored the temperatures at those surfaces. The electronic readout of these thermocouples had a resolution of 0.1 °C.

The chamber was filled with polydimethylsiloxane, otherwise known as silicone oil. Its Dow Corning designation is "200 fluid at 50 centistokes." Its refractive index at 25 °C is 1.4022, and the coefficient of thermal expansion for this index is $\beta = 0.00104 \text{ cc}/(\text{cc } ^\circ\text{C})$.

The experimental equipment is shown schematically in Figure 9.1. A collimated beam of 514.5 nm laser light was passed through the windows of the chamber. The light was generated by an Argon ion laser operated without an etalon, without a prism, and without a constant intensity feedback mechanism. The multiline output intensity was nominally 120 mW, but fluctuated about 20% from this value. Two external prisms and a beam stop were used to select the 514 nm line, and beam steering mirrors brought the light up to the windows' height. A 40X microscope and a 10 micron pinhole were used with a 50 millimeter Nikkor lens to produce a 24 millimeter diameter collimated beam with a power density of nominally 1.5 mW/cm^2 , or 6.8 mW total power. The horizontally polarized light traveled through the test chamber windows. A 16 millimeter diameter aperture behind the last window sharply truncated the beam. A 100 millimeter Cooke triplet lens focused the light, forming an f/6.3 beam. The LCPDI was oriented with the relaxed liquid crystal molecules lying horizontally, was mounted on a 3-axis positioner, and was placed just behind the focused spot. A ground glass screen was placed 21 centimeter behind the LCPDI, and a 50 millimeter Nikkor lens at f/5.8 imaged the interferogram onto a CCD detector array.

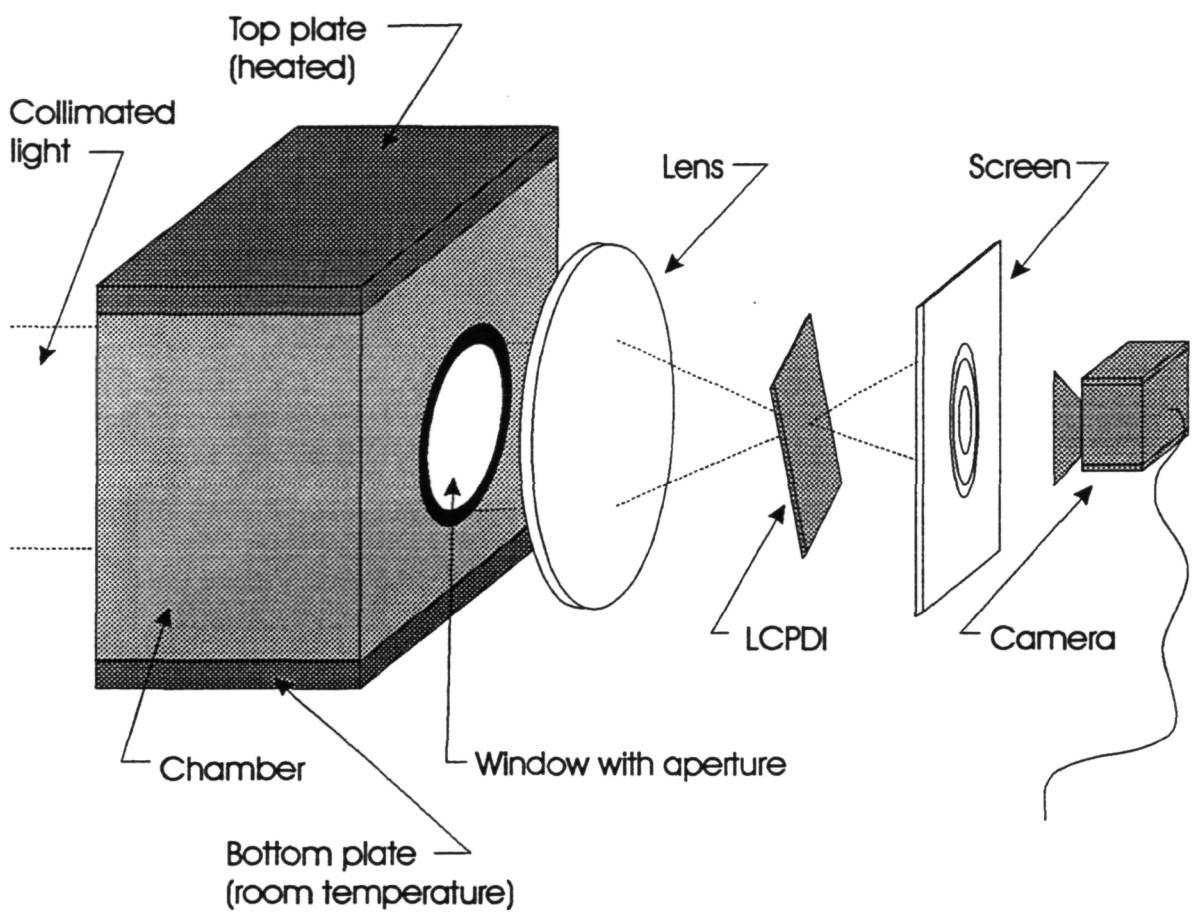


FIGURE 9.1, Experimental apparatus for temperature measurement.

The CCD array was part of a Sony XC-77 RS-170 camera. There were 768 x 493 active pixels, each pixel was 11.38 x 13.50 microns for an aspect ratio of 0.843.

9.2 Data acquisition

9.2.1 LCPDI

Images from the camera were digitized into a personal computer by an Epix 4Meg frame grabber. A programmable Hewlett-Packard HP 3325A function generator was used to generate the AC voltage for phase stepping. It was controlled by the computer via an IEEE-488 bus. Code was written to drive the function generator and to acquire and store the images. A delay of 7 seconds was inserted between the time that the voltage was changed and the image was acquired to ensure that the liquid crystals had reached a steady-state orientation. An additional 6 seconds was needed to write the images to the hard drive. The total time for acquiring five phase-stepped interferograms was therefore about 65 seconds.

To measure the thermal gradient across the test chamber, two wavefronts were measured. First, five phase-stepped interferograms were recorded to measure the wavefront passing through the chamber with the oil at room temperature (isothermal condition). Then the top and bottom chamber plates were set to the desired temperature and left there for about an hour to allow the oil to reach equilibrium. Five more phase-stepped interferograms were then recorded to measure the wavefront passing through the heated oil. The difference between these measured wavefronts was then used to determine the temperature distribution across the oil.

9.2.2 Thermocouple

To verify the LCPDI measurement, the oil temperature distribution was also measured with a thermocouple. The K-type thermocouple was mounted in a 0.8 millimeter diameter tube that was inserted through a small port in the top of the chamber. The tube was mounted on a traversing stage and scanned from the top to the bottom of the chamber. Temperature readings were taken every millimeter when the probe was within the window area, and every 5 millimeters when the probe was above and below the window. In addition, the temperature was measured when the probe was at the top and bottom edges of the window. The temperature was displayed on an electronic readout with a resolution of 0.1 °C. The calibrated thermocouple had an accuracy better than 0.05 °C, but because of the low resolution readout the measurement has an accuracy of only 0.1 °C.

9.3 Data processing

A binary mask was created to eliminate information from the interferograms outside the windows. One of the interferograms was histogram equalized, and then thresholded to produce the mask. Pixels whose value was above the threshold were set to one, and the rest were set to zero. Each interferogram was then multiplied by the mask. The ten raw, masked interferograms are shown in Figure 9.2. The five interferograms taken while the chamber was in the isothermal condition are shown in (a), and the interferograms shown in (b) were taken after the top plate was heated. The circular windows appear elliptical because the aspect ratio of the pixels was not unity. The aspect ratio was corrected as the final step in the data processing.

The interferograms were then normalized to compensate for intensity fluctuations caused by not only the rotation of the dye, but also by laser instabilities. The fourth method

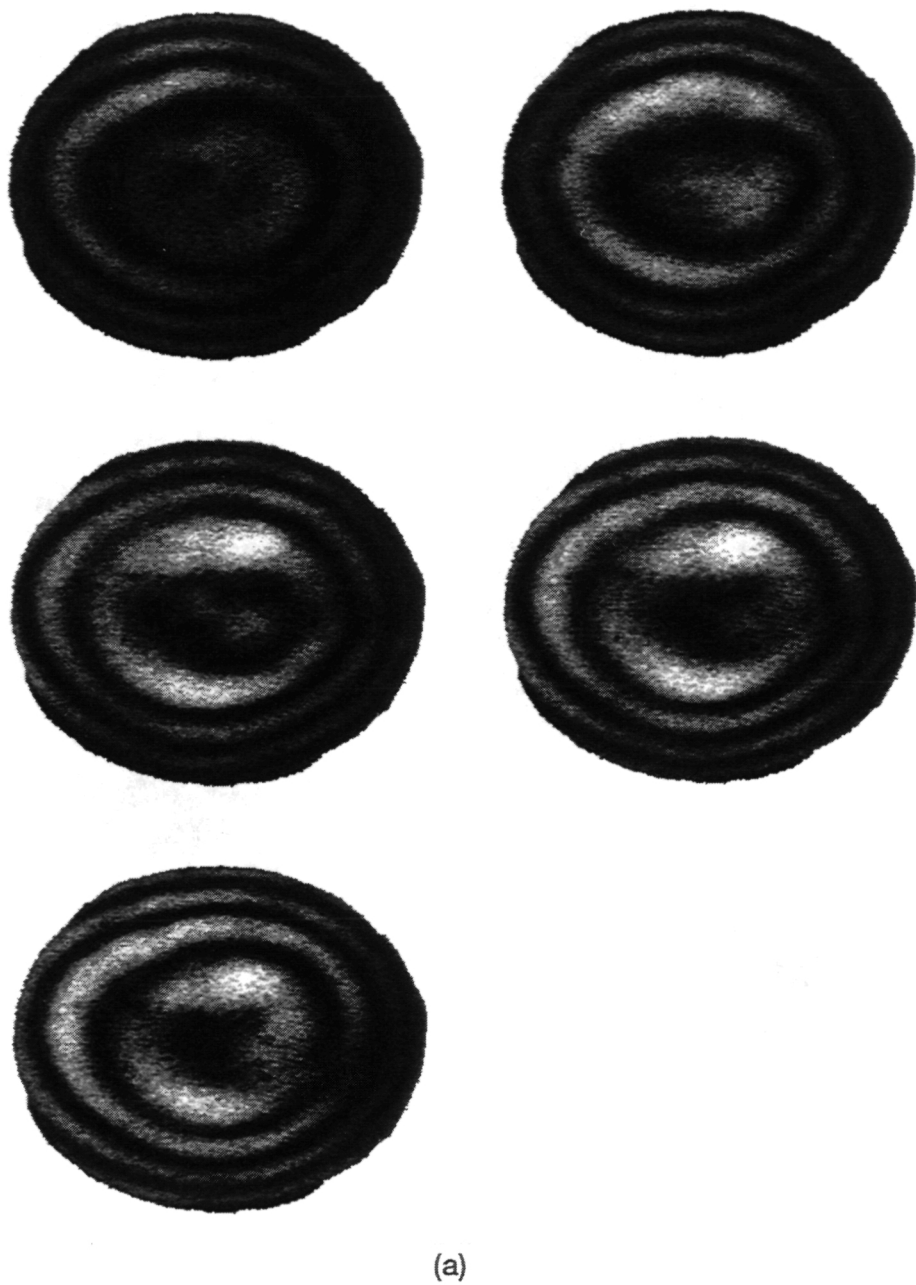


FIGURE 9.2, Raw, masked interferograms: (a) before and (b) after heat applied to top chamber plate.

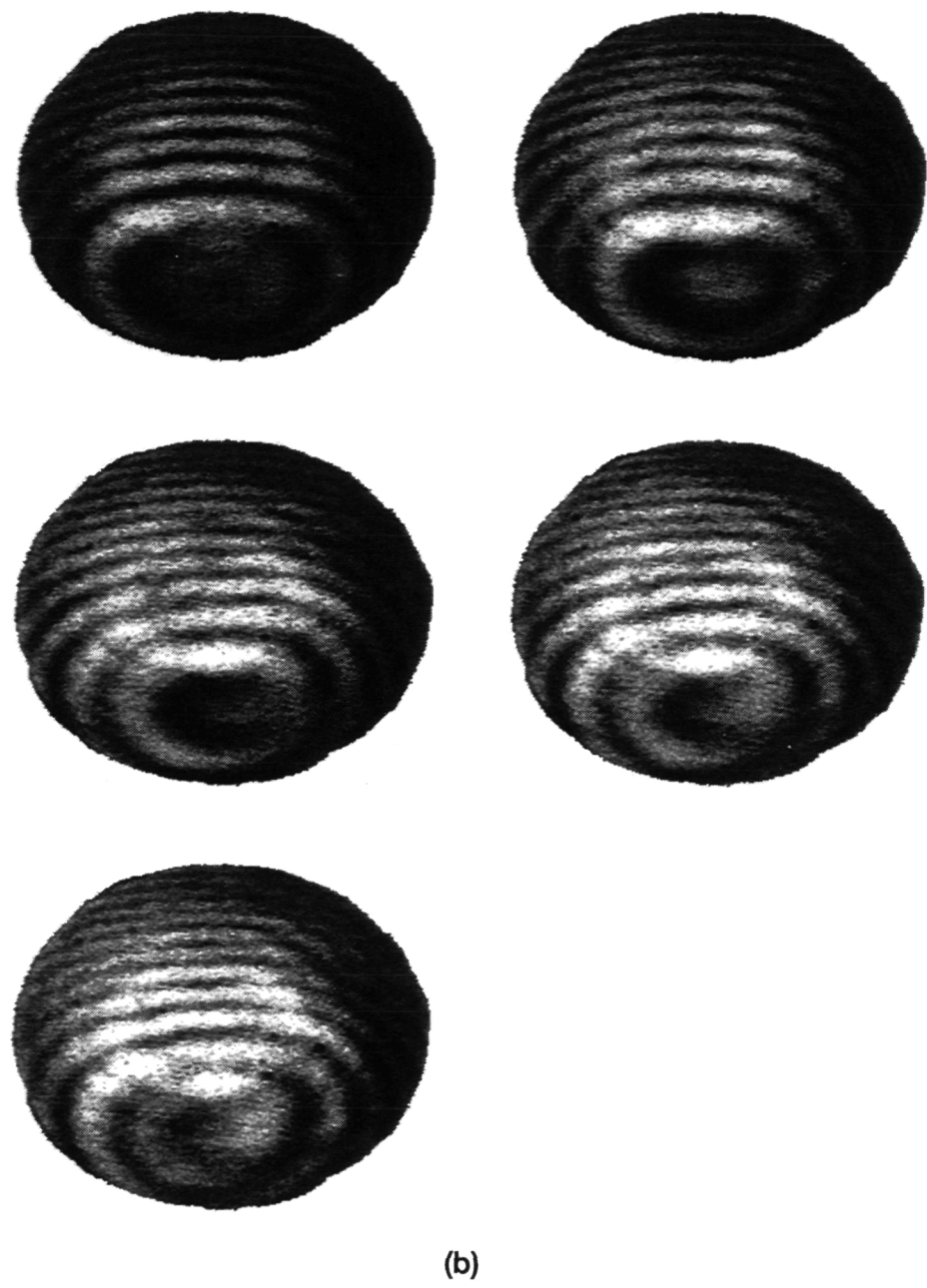


FIGURE 9.2 (continued), Raw, masked interferograms: (a) before and (b) after heat applied to top chamber plate.

described in Section 7.5.3, a polynomial fit to each interferogram, was used to obtain approximations for each object beam intensity distribution. A two-dimensional quadratic surface⁴⁰ was fit to each unmasked raw interferogram, and the value of each pixel in each interferogram was divided by the value of the corresponding pixel of its quadratic surface. The ten normalized, masked interferograms are shown in Figure 9.3.

Each set of five normalized interferograms was used in Hariharan's algorithm to compute the two phase maps. The modulo 2π phase maps were unwrapped, and the aspect ratio of the images was fixed by scaling the x-axis by the ratio of the width and height of the pixels. The original 768 x 493 pixel images were resampled to become 647 x 493 pixel images, because (768 pixels) (11.38 microns / 13.50 microns) = 647 pixels.

The unwrapped, scaled phase maps are shown as wire-mesh plots in Figure 9.4, before and after heat was applied to the chamber. The phase map representing the wavefront passing through the isothermal cell was subtracted from the wavefront measured in the presence of the thermal gradient. The difference is shown in Figure 9.5.

This phase difference occurs because the refractive index of the oil changed with temperature. To determine the temperature distribution that caused this phase difference, the phase difference can be converted to a refractive index distribution, which in turn can be converted to a temperature map. The following equations were used to perform these conversions:

$$\Delta n = \frac{\lambda}{360^\circ} \frac{\Delta\phi}{L} \quad (34)$$

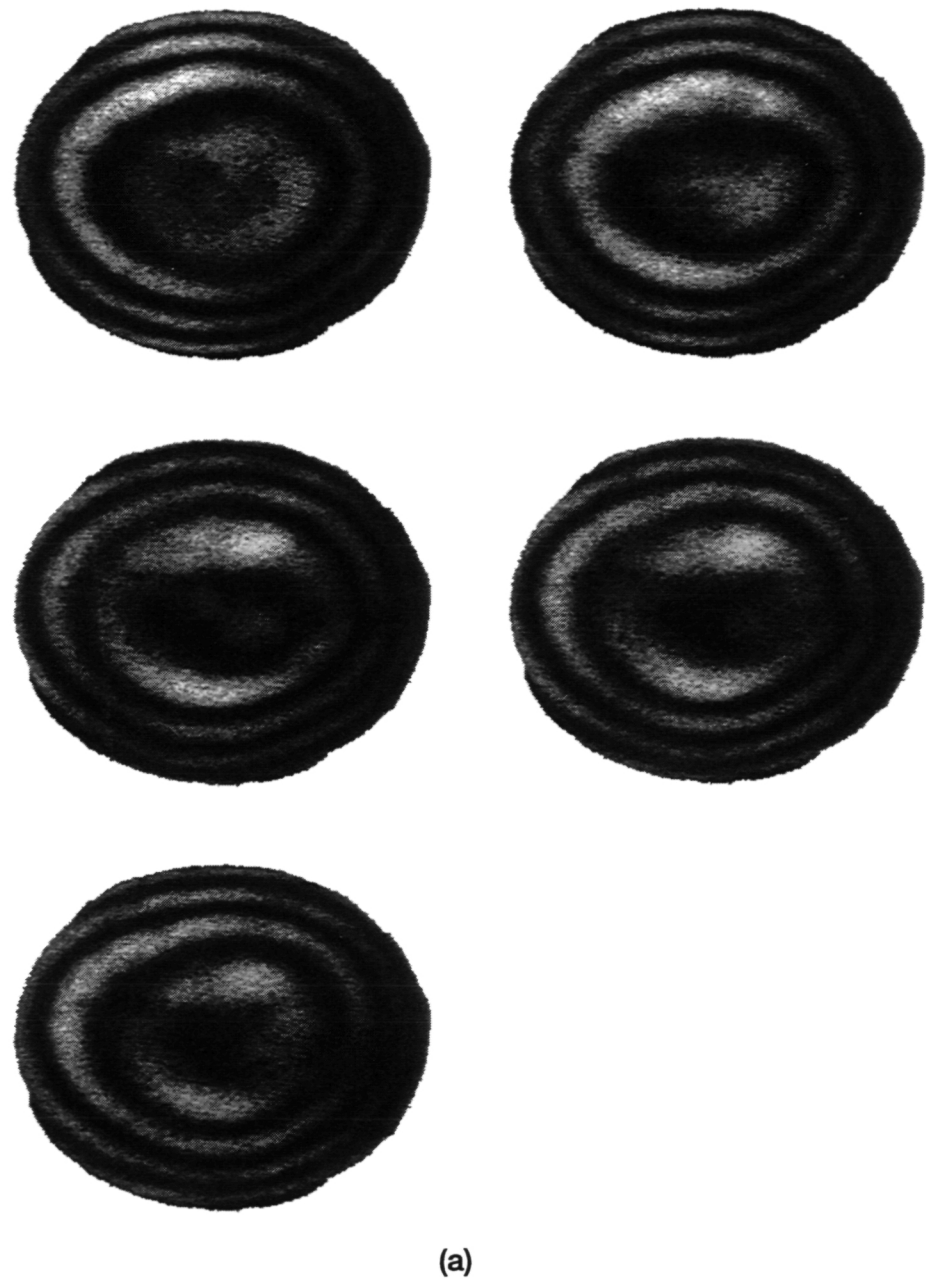


FIGURE 9.3, Normalized masked interferograms: (a) before and (b) after heat applied to top chamber plate.

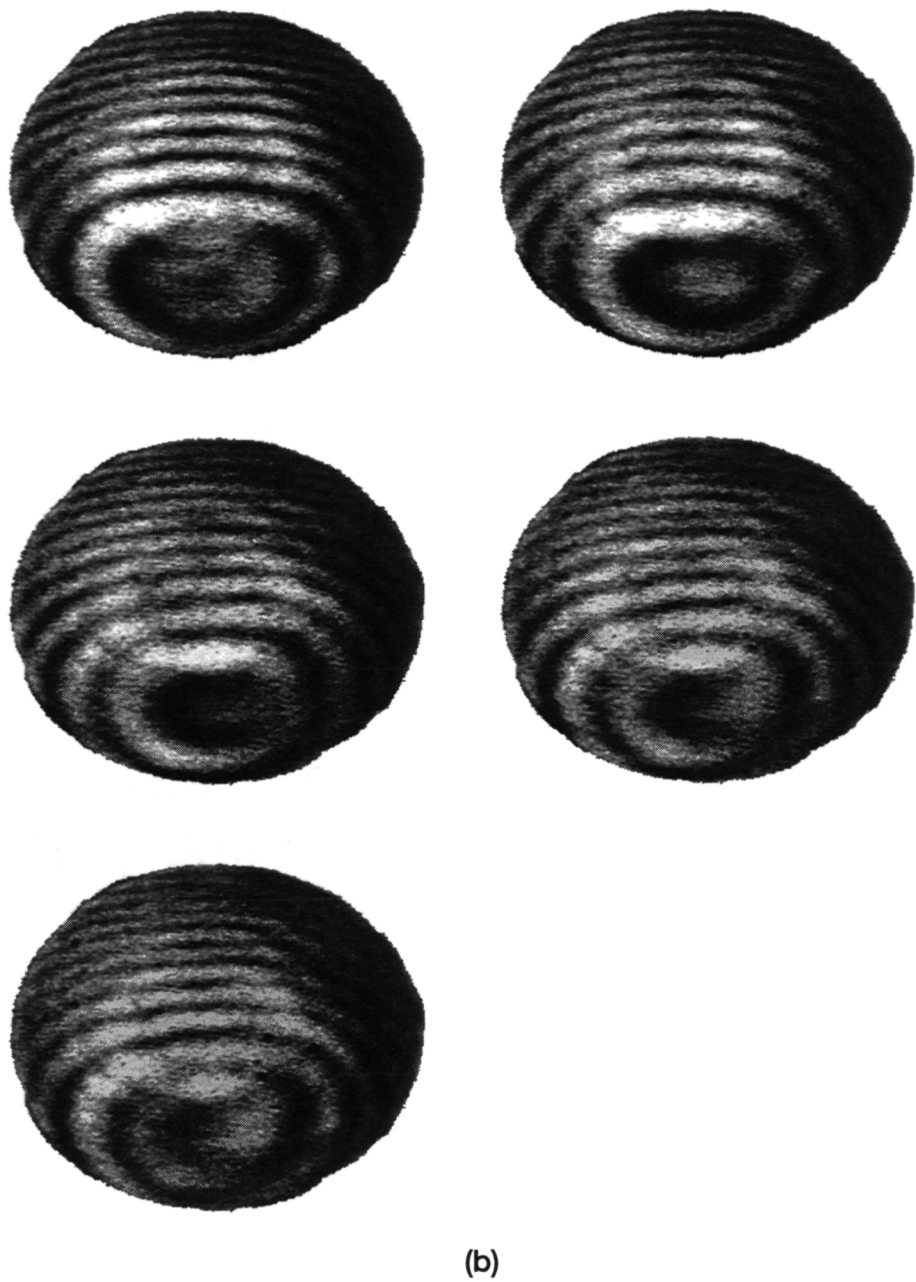


FIGURE 9.3 (continued), Normalized masked interferograms: (a) before and (b) after heat applied to top chamber plate.

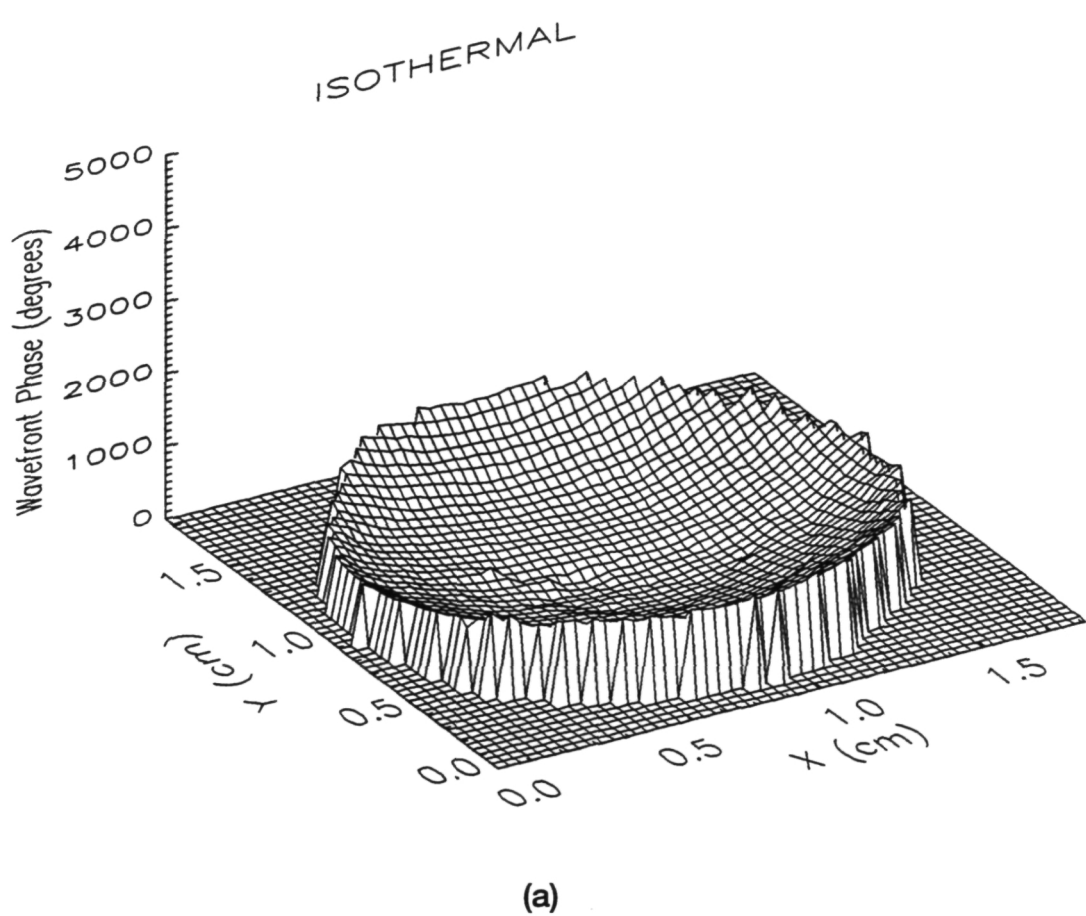


FIGURE 9.4, Wavefronts measured with the LCPDI with the top chamber plate at (a) 23.4 °C and (b) 25.4 °C .

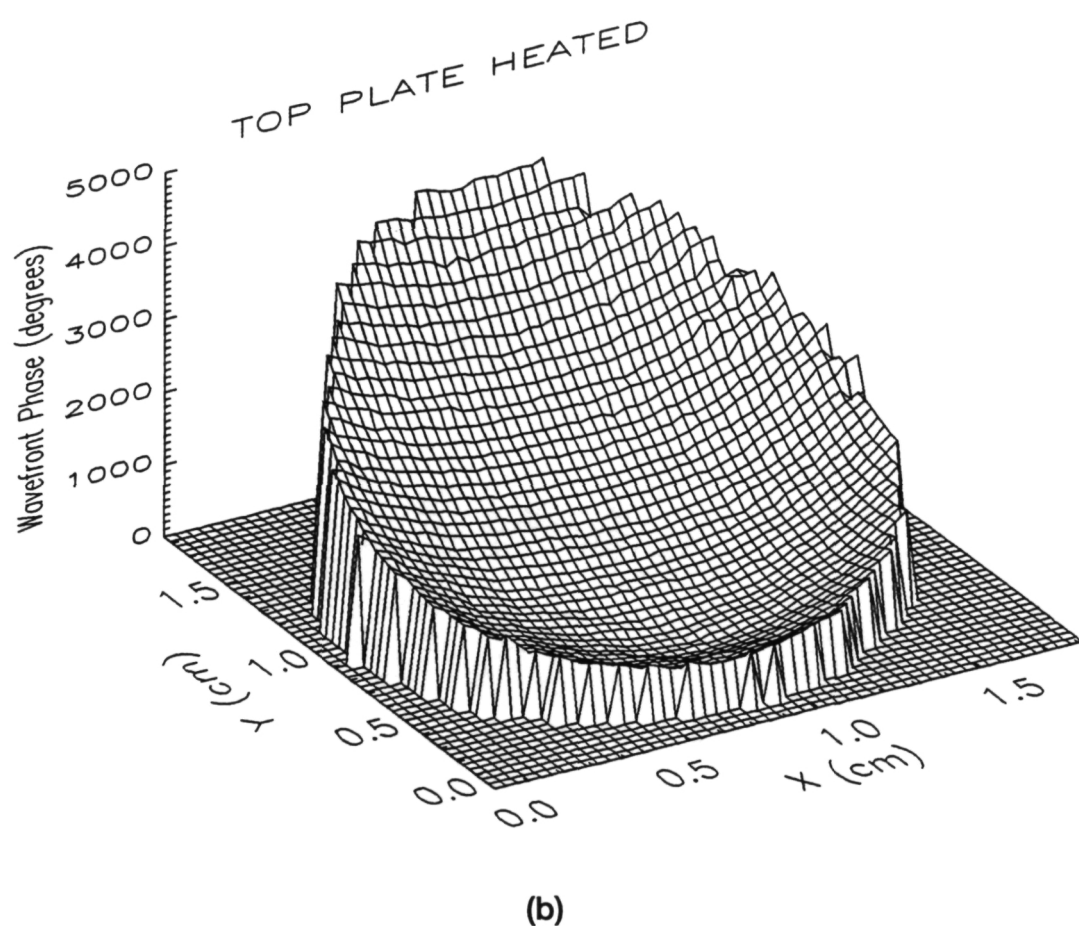


FIGURE 9.4 (continued), Wavefronts measured with the LCPDI with the top chamber plate at (a) 23.4 °C and (b) 25.4 °C .

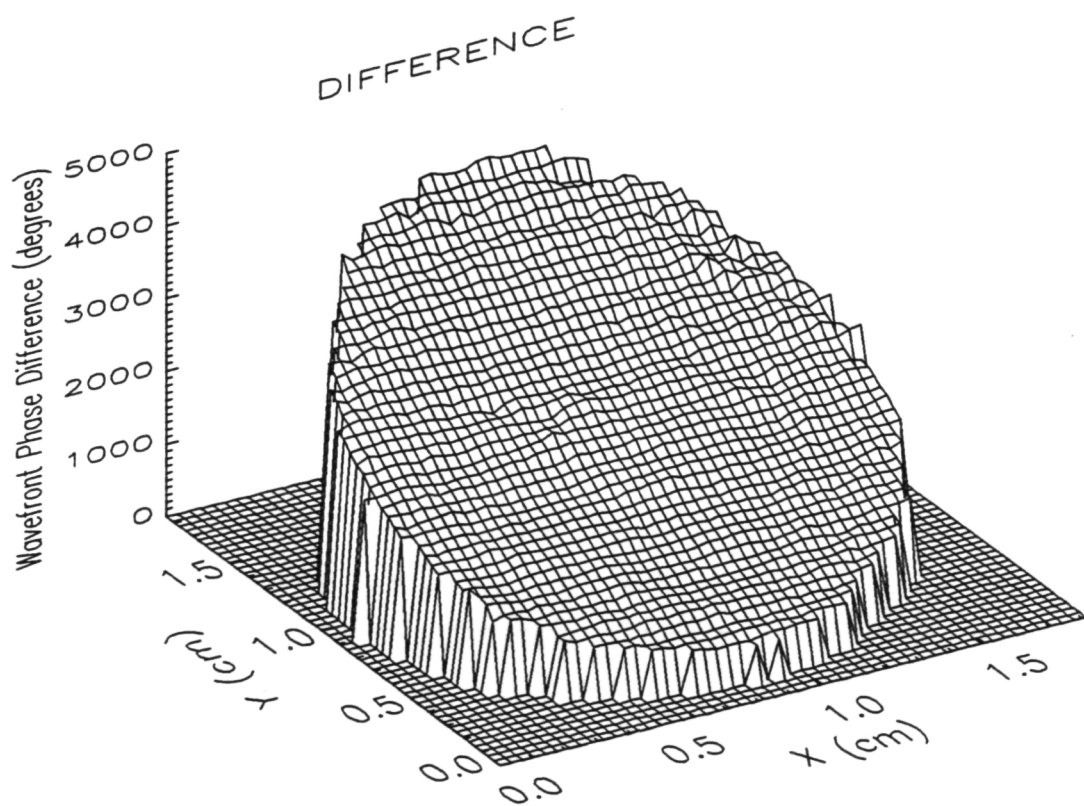


FIGURE 9.5, Difference between wavefronts measured with isothermal and heated oil chamber.

$$\frac{dn}{dT} = -\frac{3}{2} \frac{n(n^2 - 1)}{2n^2 + 1} \beta \quad (35)$$

$$\Delta T = \frac{\Delta n}{dn/dT} \quad (36)$$

where L in this case refers to the length of the oil chamber along the optic axis ($L = 43$ mm). Equation (35) is taken from Vest's book.⁴¹ The temperature is therefore proportional to the measured phase difference, where the constant of proportionality is:

$$-\frac{\lambda}{540L\beta} \frac{2n^2 + 1}{n(n^2 - 1)} \quad (37)$$

The isothermal wavefront, the wavefront measured after heating the top plate, and the difference between the two, converted to temperature, is shown in Figure 9.6.

Figure 9.7 shows an interferogram with the probe about half-way between the top and bottom of the chamber. A column is blanked out, indicating the line of LCPDI data corresponding to axis along which the thermocouple measurements were made. The relative temperature difference measured by the LCPDI was converted to an absolute temperature distribution by first subtracting the measured value of dT at the bottom of the window in the appropriate column from the entire LCPDI data set, forcing the temperature difference to zero at that point. The temperature measured at that point by the thermocouple was then added to the entire LCPDI data set. The LCPDI curve was then shifted by 0.03°C to obtain better agreement between the data sets. This shift is well within the $\pm 0.05^\circ\text{C}$ error bars of the thermocouple data.

The absolute temperature measured by the LCPDI along this column is plotted in Figure

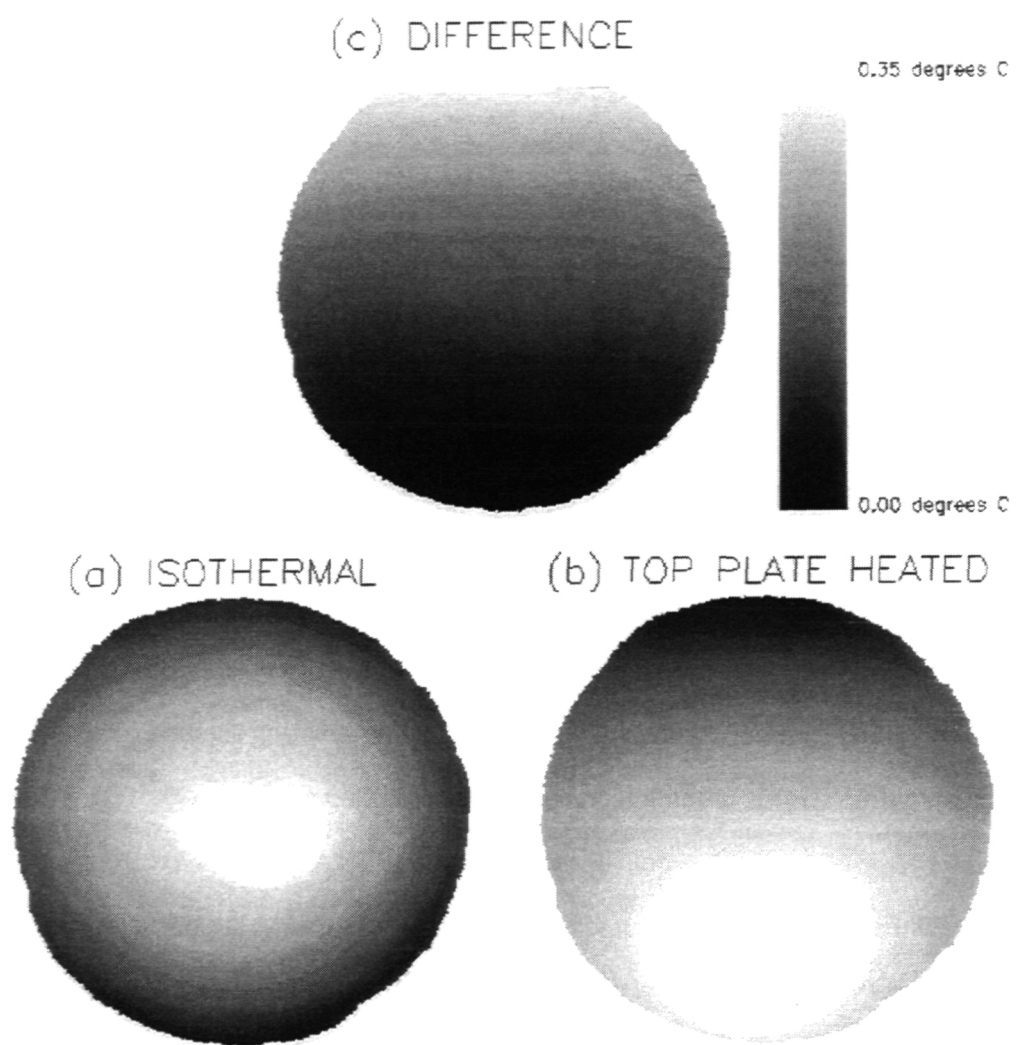


FIGURE 9.6, Temperature measurement data.

(a) Wavefront through isothermal chamber, (b) wavefront through heated chamber, (c) difference between the two.

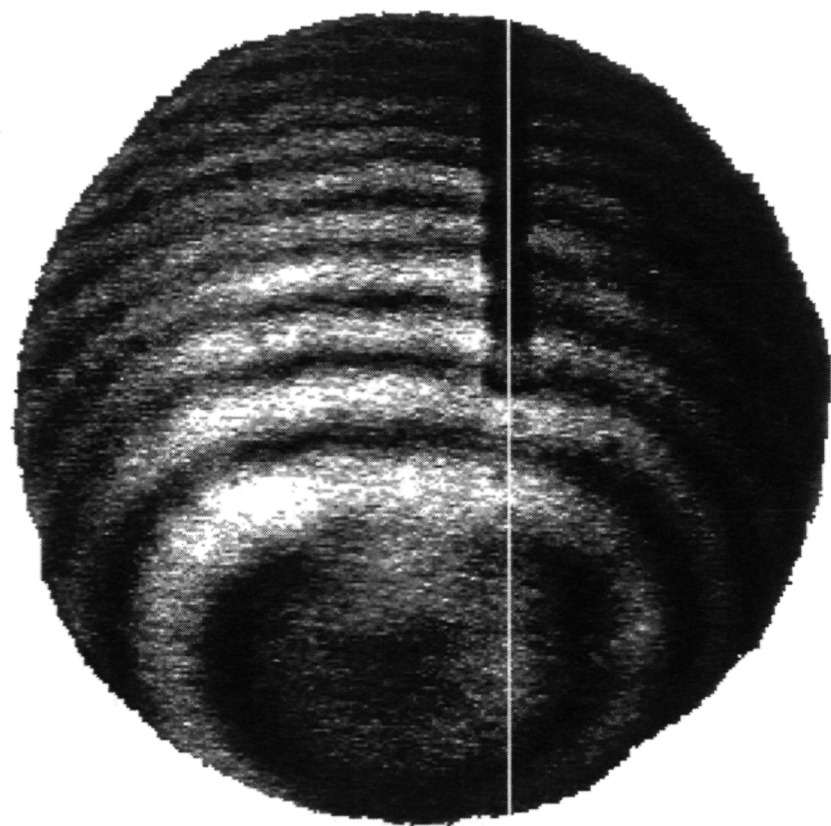


FIGURE 9.7, Interferogram with thermocouple probe inserted into chamber.

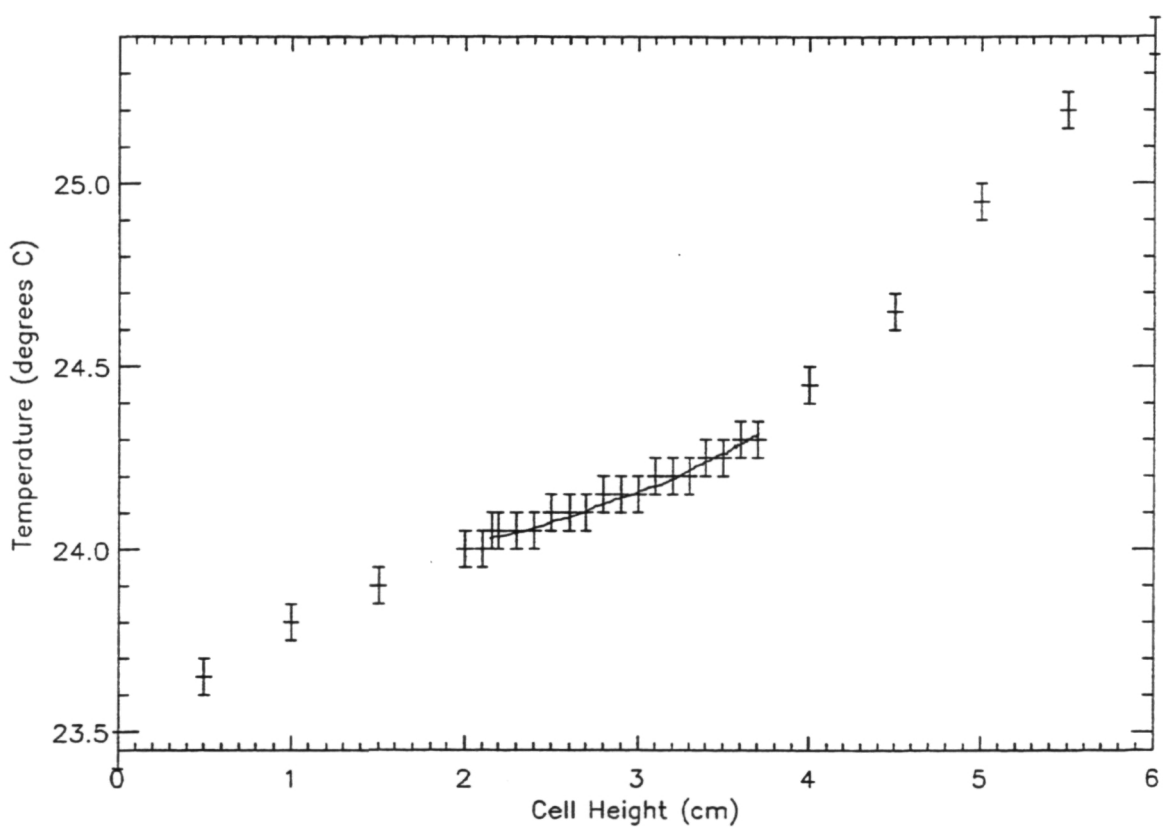


FIGURE 9.8. Plot of temperature across chamber, measured with LCPDI and traversing thermocouple.

9.8, together with the temperature measurements from the traversing thermocouple. As just described, the two curves were forced to intersect at the bottom of the window.

9.4 Results

The data shown in Figure 9.8 indicates excellent agreement between the LCPDI temperature measurement and the thermocouple measurements, certainly to within the 0.1 °C resolution of the thermocouple data.

The non-linear temperature distribution across the chamber is typical of what has been observed in similar fluid chambers in previous experiments. The thermal gradients are steeper at the top and bottom surfaces of the chamber because heat transfer occurs across the un-insulated walls.

The amount of error in this temperature distribution measured by the LCPDI can be determined by assuming that errors in each of the factors in Equation 36 are independent from each other. Using the propagation of errors method,

$$\left(\frac{\sigma_T}{T}\right)^2 = \left(\frac{\sigma_\lambda}{\lambda}\right)^2 + \left(\frac{\sigma_\phi}{\phi}\right)^2 + \left(\frac{\sigma_L}{L}\right)^2 + \left(\frac{\sigma_\beta}{\beta}\right)^2 + \left[\frac{2n^4 + 5n^2 - 1}{n^2(n^2 - 1)^2}\right]^2 \sigma_n^2 \quad (38)$$

If the uncertainty of the phase measurement is 1 degree, and the uncertainty of each of the other factors is 1%, the uncertainty in the measured temperature is 12.7%. The largest contributor to this uncertainty is the uncertainty in refractive index. If $\sigma n/n$ is 0.25% rather than 1%, the overall uncertainty drops to 3.5%.

This LCPDI technique has been shown to be effective for measuring a thermal gradient of about $0.2 \text{ }^{\circ}\text{C}/\text{cm}$, through a 43 millimeter thick volume of 50 centistokes oil. This makes the instrument useful for detecting small fluid variations. As the temperature gradient becomes stronger, the center of the focused spot on the LCPDI will deflect farther from the microsphere. A gradient at least four times as strong as the one demonstrated here should be measurable without difficulty, especially if the LCPDI plate is pre-shifted vertically so that the center of the isothermal interference pattern is shifted towards the cold side of the expected thermal gradient. Nominally linear gradients larger than about $1 \text{ }^{\circ}\text{C}/\text{cm}$ will not be measurable in this particular experiment for two reasons: first, the fringes will become too small for Nyquist detection, and second, the fringe contrast will be bad because the reference beam intensity will greatly decrease. The range can be extended, however, by reducing the thickness of the oil volume (L), choosing a fluid with a lower variation of refractive index with temperature, or using sub-Nyquist interferometry.¹²

10. CONCLUSION

The liquid crystal point diffraction interferometer combines the robust, common-path design of the PDI with a simple method of optical phase control. The result is a compact new instrument for the measurement of optical wavefronts that uses phase stepping interferometry for high data density and automatic data reduction.

The LCPDI was used to measure both a focus shift and a temperature distribution across a fluid. These demonstrations show that the instrument can accurately measure wavefront differences, particularly those caused by sensitive fluid temperature variations of interest to fluid scientists. The LCPDI is more accurate and provides more data density than anything currently used in the European or American microgravity programs. Because the LCPDI itself introduces aberrations into the interferograms, it is best used in applications where wavefront differences are of interest. The difference operation will automatically compensate for the induced aberrations. Nonetheless, the instrument has potential for testing optical elements such as lenses and mirrors provided either a reference optic is available, or the initial aberrations can be identified.

The LCPDI currently modulates both the intensity and phase of the object beam. The unwanted intensity modulation causes a periodic error in the measured wavefront phase. Normalization techniques were developed for reducing not only this error, but also errors caused by laser intensity fluctuations. This extends the use of phase stepping interferometry to lasers with varying intensity, such as laser diodes, gas lasers operated without closed-loop intensity control, and lasers coupled into optical fibers without the use of opto-isolators to prevent feedback.

Future work for the LCPDI includes improvements to the LCPDI itself, determining broader applications for it, and packaging it for robust use. Improvements to the LCPDI include finding a dye with symmetrical molecular structure whose attenuation will not vary with orientation, adding anti-reflection coatings to the glass substrates to eliminate the need for tilting the LCPDI, using fewer microspheres to allow easier alignment, and speeding up the phase stepping time using the transient nematic effect. An intriguing possibility is the use of the LCPDI with no explicit diffracting elements; the liquid crystal molecules will reorient themselves in response to a strong optical field as well as an electric field, and preliminary evidence suggests that the incident light can be configured in such a way that the strong central portion of the beam can maintain the liquid crystals in one orientation while the applied electric field can control the phase of the outer portion of the beam.

APPENDIX A:
LIST OF PUBLICATIONS

The following papers report on work discussed in this dissertation:

C.R. Mercer, K. Creath, "A phase-stepped point diffraction interferometer using liquid crystals," to be presented at *Interferometry VII: Techniques and analysis*, Proc. Soc. Photo-Opt. Instrum. Eng. (1995).

C.R. Mercer, K. Creath, "Liquid crystal point diffraction interferometer," to be submitted to App. Opt. (1995).

C.R. Mercer, N. Rashidnia, K. Creath, "High data density temperature measurement for quasi steady-state flows," submitted to Exp. Fluid. (1995).

C.R. Mercer, K. Creath, "Phase measurement using a liquid crystal point diffraction interferometer," in *Industrial Optical Sensors for Metrology and Inspection*, Proc. Soc. Photo-Opt. Instrum. Eng. **2349**, 95-99 (1994).

C.R. Mercer, K. Creath, "Defocus measurement using a liquid crystal point diffraction interferometer," OSA Opt. Fab. Test. Work. Tech. Dig. **13**, 293-296 (1994).

C.R. Mercer, K. Creath, "Liquid crystal point diffraction interferometer," Opt. Lett. **19**(12), 916-918 (1994).

APPENDIX B:
ILLUSTRATIONS, TABLES, AND GRAPHS

TABLE 1. Simulation Parameters

$\alpha = [0.25, 0.43, 0.51, 0.76, 1.00]$	$\phi_j = j\pi/2 + \pi/4$
$\sigma = 1.5$	$\sigma_y = 0.5$
$\bar{I}^{obj} = 74$	$\bar{I}^{ref} = 5$
$dc^{obj} = 15$	$dc^{ref} = 1$

APPENDIX C: DERIVATIONS

Derivations of the equations used for the Fourier analysis of the LCPDI in Section 5.1.2 are presented here.

The phase and amplitude transmission of a generalized PDI plate can be written as:

$$\tau(r) = [\tau_b + (1 - \tau_b) \text{cyl}(r/d)] \exp[i[\phi_b + (\phi_0 - \phi_b) \text{cyl}(r/d)]]$$

where d is the diameter of the central circular aperture, the transmittance and phase delay of the central aperture are 1 and ϕ_0 respectively, and the corresponding parameters for the background region outside the central aperture are τ_b and ϕ_b .

The Fourier transform of this circularly symmetric function can be found using the Hankel transform:

$$\mathcal{J}\{\tau(r)\}_{\rho=\frac{r}{\lambda f}} = T(\rho)_{\rho=\frac{r}{\lambda f}} = 2\pi \int_0^\infty t(r) J_0(2\pi\rho r) r dr$$

$$T(\rho) = 2\pi \int_0^\infty \tau_b \exp[i[\phi_b + (\phi_0 - \phi_b) \text{cyl}(r/d)]] J_0(2\pi\rho r) r dr + \\ 2\pi \int_0^{d/2} (1 - \tau_b) \exp[i[\phi_b + (\phi_0 - \phi_b)]] J_0(2\pi\rho r) r dr$$

$$T(\rho) = 2\pi \tau_b \exp(i\phi_b) \left\{ \int_0^{d/2} \exp[i(\phi_0 - \phi_b)] J_0(2\pi\rho r) r dr + \int_{d/2}^\infty J_0(2\pi\rho r) r dr \right\} + \\ 2\pi(1 - \tau_b) \exp(i\phi_0) \int_0^{d/2} J_0(2\pi\rho r) r dr$$

$$T(\rho) = 2\pi \exp(i\phi_0) [\tau_b + (1 - \tau_b)] \int_0^{d/2} J_0(2\pi\rho r) r dr + \\ 2\pi \tau_b \exp(i\phi_b) \left\{ \int_0^\infty J_0(2\pi\rho r) r dr - \int_{d/2}^\infty J_0(2\pi\rho r) r dr \right\}$$

$$T(\rho) = 2\pi \exp(i\phi_0) [1 - \tau_b \exp(i\phi_b)] \int_0^{d/2} J_0(2\pi\rho r) r dr + 2\pi \tau_b \exp(i\phi_b) \int_0^{\infty} J_0(2\pi\rho r) r dr$$

This expression can be solved by using the following two identities and a transformation of variables:

$$2\pi \int_0^{\infty} J_0(2\pi\rho r) r dr = \delta(\vec{\rho}) = \frac{\delta(\rho)}{\pi\rho} \quad \text{where } \rho = |\vec{\rho}|,$$

$$\int_0^u J_0(x) x dx = u J_1(u)$$

$$\text{let } x = 2\pi\rho r$$

$$\text{then } dx = 2\pi\rho dr$$

$$\int_0^{d/2} J_0(2\pi\rho r) r dr = \int_0^{\pi d\rho} J_0(x) \frac{x}{2\pi\rho} \frac{dx}{2\pi\rho}$$

$$\int_0^{d/2} J_0(2\pi\rho r) r dr = \frac{1}{(2\pi\rho)^2} \int_0^{\pi d\rho} J_0(x) x dx$$

$$\int_0^{d/2} J_0(2\pi\rho r) r dr = \frac{\pi d\rho}{(2\pi\rho)^2} J_1(\pi d\rho)$$

$$\int_0^{d/2} J_0(2\pi\rho r) r dr = \frac{1}{2\pi} \frac{2\pi}{1} \frac{\pi d\rho}{(2\pi\rho)^2} \frac{\pi d\rho}{2} \frac{2J_1(\pi d\rho)}{\pi d\rho}$$

$$\int_0^{d/2} J_0(2\pi\rho r) r dr = \frac{1}{2\pi} \frac{\pi d^2}{4} \frac{2J_1(\pi d\rho)}{\pi d\rho}$$

$$2\pi \int_0^{d/2} J_0(2\pi\rho r) r dr = \frac{\pi d^2}{4} \frac{2J_1(\pi d\rho)}{\pi d\rho}$$

The final result is therefore:

$$T(\rho) = [\exp(i\phi_0) - \tau_b \exp(i\phi_b)] \frac{\pi d^2}{4} \text{somb}(d\rho) + \tau_b \exp(i\phi_b) \frac{\delta(\rho)}{\pi\rho}$$

and evaluating the expression at $\rho = r/\lambda f$ yields:

$$T(r) = T(\rho)_{\rho=\frac{r}{\lambda f}} = [\exp(i\phi_0) - \tau_b \exp(i\phi_b)] \frac{\pi d^2}{4} \text{somb}\left(\frac{dr}{\lambda f}\right) + \tau_b \exp(i\phi_b) \frac{\delta\left(\frac{r}{\lambda f}\right)}{(\pi r / \lambda f)}.$$

This is Equation (14).

The optical field at the image plane is then found by convolving this expression with the original wavefront evaluated at the image plane:

$$u(r) = T(r) * u_i(r)$$

$$u(r) = [\exp(i\phi_0) - \tau_b \exp(i\phi_b)] \frac{\pi d^2}{4} \text{somb}\left(\frac{dr}{\lambda f}\right) * * \text{cyl}\left(\frac{r}{D}\right) \exp\left[\frac{2\pi i}{\lambda} W(r)\right] +$$

$$\tau_b \exp(i\phi_b) \frac{\lambda f \delta\left(\frac{r}{\lambda f}\right)}{\pi r} * * \text{cyl}\left(\frac{r}{D}\right) \exp\left[\frac{2\pi i}{\lambda} W(r)\right]$$

$$u(r) = \lambda f \left\{ \tau_b \exp(i\phi_b) \text{cyl}\left(\frac{r}{D}\right) \exp\left[\frac{2\pi i}{\lambda} W(r)\right] \right\} +$$

$$\lambda f \left\{ [\exp(i\phi_0) - \tau_b \exp(i\phi_b)] \frac{\pi d^2}{4 \lambda f} \text{somb}\left(\frac{dr}{\lambda f}\right) * * \text{cyl}\left(\frac{r}{D}\right) \exp\left[\frac{2\pi i}{\lambda} W(r)\right] \right\}$$

This final expression is proportional to Equation (15).

REFERENCES

- ¹V.P. Linnik, "Simple interferometer for the investigation of optical systems," Comp. Rend. Acad. Sci. URSS, **1**, 208-210 (1933).
- ²R.N. Smartt, J. Strong, "Point-diffraction interferometer," (Abstract only), J. Opt. Soc. Am. **62**, 737 (1972).
- ³R.N. Smartt, W. H. Steel, "Theory and application of point-diffraction interferometers," Japan. J. Appl. Phys. **14**, Suppl. 14-1, 351-357 (1975).
- ⁴R.J. Speer, M. Crisp, D. Turner, S. Mrowka, K. Tregidjo, "Grazing incidence interferometry: the use of the Linnik interferometer for testing image-forming reflection systems," Appl. Opt. **18**, 2003-2012, (1979).
- ⁵C. Koliopoulos, O. Kwon, R. Shagam, J.C. Wyant, C.R. Hayslett, "Infrared point-diffraction interferometer," Opt. Lett. **3**(3), 118-120 (1978).
- ⁶J.P. Marioge, B. Bonino, F. Bridou, P. Fournet, M. Mullot, "La fabrication et le controle de surface toriques," J. Opt. (Paris) **15**, 286-292 (1984).
- ⁷W. Harris, S. Mrowka, R.J. Speer, "Linnik interferometer: its use at short wavelengths," Appl. Opt. **21**(7), 1155 (1982).
- ⁸A.K. Aggarwal, S.K. Kaura, "Further applications of point diffraction interferometer," J. Opt. (Paris) **17**(3), 135-138 (1986).
- ⁹M. Giglio, E. Paganini, U. Perini, "A self-aligning point diffraction interferometer for fluid studies," in *Optical Components and Systems*, Proc. Soc. Photo-Opt. Instrum. Eng. **805**, 82-86 (1987).
- ¹⁰S. Musazzi, U. Perini, F. Trespidi, "Point diffraction interferometer for fluids study in microgravity environment," Exp. Therm. Fluid Sci. **6**, 49-55 (1993).
- ¹¹K. Creath, "Phase-Measurement Interferometry Techniques," in *Progress in Optics XXVI*, E. Wolf, ed., (Elsevier Science Publishers, New York, 1988), chap. 5.
- ¹²J.E. Greivenkamp, J.H. Bruning, "Phase Shifting Interferometry," in *Optical Shop Testing*, D. Malacara, ed., (John Wiley & Sons, New York, 1992), chap. 14.
- ¹³R.N. Smartt, "Special applications of the point-diffraction interferometer," in *Interferometry*, Proc. Soc. Photo-Opt. Instrum. Eng. **92**, 35-40 (1979).

REFERENCES – *Continued*

- ¹⁴G. Wang, Y. Zheng, A. Sun, S. Wu, Z. Wang, "Polarization pinhole interferometer," Opt. Lett. **16**, 1352-1354 (1991).
- ¹⁵W.E. James, P. Hariharan, "Line diffraction test," Appl. Opt. **25**(21), 3806-3807 (1986).
- ¹⁶K. Underwood, J.C. Wyant, C.L. Koliopoulos, "Self-referencing wavefront sensor," Proc. Soc. Photo-Opt. Instrum. Eng. **351**, 108-114 (1982).
- ¹⁷O.Y. Kwon, "Multichannel phase-shifted interferometer," Opt. Lett. **9**(2), 59-61 (1984).
- ¹⁸H. Kadono, N. Takai, T. Asakura, "New common-path phase shifting interferometer using a polarization technique," Appl. Opt. **26**(5), 898-904 (1987).
- ¹⁹J. Ojeda-Castaneda, *Optical Shop Testing*, 2nd ed., D. Malacara, ed., (John Wiley & Sons, New York, 1992), chap. 8.
- ²⁰J.W. Goodman, *Introduction to Fourier Optics*, (McGraw-Hill, New York, 1968).
- ²¹H. Kadono, M. Ogusu, S. Toyooka, "Phase shifting common path interferometer using a liquid-crystal phase modulator," Opt. Comm. **110**, 391-400 (1994).
- ²²R.C. Anderson, J.E. Milton, "Conversion of Schlieren systems to high speed interferometers," in *19th International Congress on High-Speed Photography and Photonics*, Proc. Soc. Photo-Opt. Instrum. Eng. **1358**, 992-1002 (1990).
- ²³F. Quercioli, G. Molesini, "Contrast reversal with a point-diffraction interferometer with a carrier frequency," Opt. Comm. **35**(3), 303-306 (1980).
- ²⁴V.P. Linnik, G.M. Bryanskaya, E.A. Sapotnitskaya, "An interferometer for studying the wavefront of a laser beam," Opt. Tech. **38**(11), 671-673 (1971).
- ²⁵W.L. Howes, "Large-aperture interferometer using local reference beam," NASA TP-2060 (1982).
- ²⁶K. Iwata, T. Nishikawa, "Profile measurement with a phase-shifting common-path polarization interferometer," in *Laser Interferometry: Quantitative Analysis of Interferograms - 3rd in a Series*, Proc. Soc. Photo-Opt. Instrum. Eng. **1162**, 389-394 (1990).

REFERENCES – *Continued*

- ²⁷E.G. Churin, A.G. Sedukhin, "Diffraction common-path interferometer," *Optoelectron. Instrum. Data Proc.* **3**, 71-74 (1994).
- ²⁸Z. Wanzhi, L. Zhenwu, "Optical testing using a point diffraction holographic interferometer," in *International Conference on Holography Applications*, Proc. Soc. Photo-Opt. Instrum. Eng. **673**, 289-291 (1986).
- ²⁹K. Creath, P. Hariharan, "Phase-shifting errors in interferometric tests with high-numerical-aperture reference surfaces," *Appl. Opt.* **33**(1) 24-25 (1994).
- ³⁰J.D. Gaskill, *Linear systems, Fourier transforms, and optics*, (John Wiley & Sons, New York, 1978).
- ³¹P.J. Collings, *Liquid crystals: nature's delicate phase of matter*, (Princeton University Press, Princeton NJ, 1990), pp. 111-112.
- ³²H. Kadono, S. Toyooka, Y. Iwaskai, "Speckle-shearing interferometry using a liquid-crystal cell as a phase modulator," *J. Opt. Soc. Am. A* **8**(12), 2001-2008 (1991).
- ³³N. Konforti, E. Marom, and S.-T. Wu, "Phase-only modulation with twisted nematic liquid-crystal spatial light modulators," *Opt. Lett.* **13**, 251-253 (1988).
- ³⁴S.-T. Wu, U. Efron, L.D. Hess, "Rotatory power and optical modulation of liquid crystals," in *Spatial Light Modulators and Applications*, Proc. Soc. Photo-Opt. Instrum. Eng. **465**, 66-73 (1984).
- ³⁵P. Hariharan, B. F. Oreb, and T. Eiju, "Digital phase-shifting interferometry: a simple error-compensating phase calculation algorithm," *Appl. Opt.* **26**(13), 2504-2506 (1987).
- ³⁶B.E.A. Saleh, M.C. Teich, *Photonics*, (John Wiley & Sons, New York 1991).
- ³⁷A.E. Perregaux, J.F. Stephany, E.C. Faucz, R.A. Hudson, V.J. Hull, A.I. LaKatos, R.A. Martel, R. Narang, B. Richter, "Transient nematic liquid crystal image bar for electrophotographic printers," *SID Digest* **28**, 360 (1987).
- ³⁸J. Amako and T. Sonehara, "Kinoform using an electrically controlled birefringent liquid-crystal spatial light modulator," *Appl. Opt.* **30**(32), 4622-4628 (1991).
- ³⁹G.H. Heilmeier, J.A. Castellano, L.A. Zanoni, "Guest-host interactions in nematic liquid crystals," *Molec. Cryst. Liq. Cryst.* **8**, 293-304 (1969).

REFERENCES -- *Continued*

⁴⁰IDL code from Johns Hopkins University / Applied Physics Laboratory, Copyright (C) 1990. Method is based on Forsythe, J. Soc. Indust. Appl. Math. 5, 74-88 (1957).

⁴¹C.M. Vest, *Holographic Interferometry*, (John Wiley & Sons, New York, 1979).

REPORT DOCUMENTATION PAGE			Form Approved OMB No. 0704-0188
Public reporting burden for this collection of information is estimated to average 1 hour per response, including the time for reviewing instructions, searching existing data sources, gathering and maintaining the data needed, and completing and reviewing the collection of information. Send comments regarding this burden estimate or any other aspect of this collection of information, including suggestions for reducing this burden, to Washington Headquarters Services, Directorate for Information Operations and Reports, 1215 Jefferson Davis Highway, Suite 1204, Arlington, VA 22202-4302, and to the Office of Management and Budget, Paperwork Reduction Project (0704-0188), Washington, DC 20503.			
1. AGENCY USE ONLY (Leave blank)	2. REPORT DATE	3. REPORT TYPE AND DATES COVERED	
	May 1995	Technical Memorandum	
4. TITLE AND SUBTITLE		5. FUNDING NUMBERS	
Liquid Crystal Point Diffraction Interferometer		WU-505-62-50	
6. AUTHOR(S)			
Carolyn R. Mercer			
7. PERFORMING ORGANIZATION NAME(S) AND ADDRESS(ES)		8. PERFORMING ORGANIZATION REPORT NUMBER	
National Aeronautics and Space Administration Lewis Research Center Cleveland, Ohio 44135-3191		E-9547	
9. SPONSORING/MONITORING AGENCY NAME(S) AND ADDRESS(ES)		10. SPONSORING/MONITORING AGENCY REPORT NUMBER	
National Aeronautics and Space Administration Washington, D.C. 20546-0001		NASA TM-106899	
11. SUPPLEMENTARY NOTES			
Responsible person, Carolyn R. Mercer, organization code 2520, (216) 433-3411. This report was submitted as a dissertation in partial fulfillment of the requirements for the degree Doctor of Philosophy to The University of Arizona, Tucson, Arizona, April 1995.			
12a. DISTRIBUTION/AVAILABILITY STATEMENT		12b. DISTRIBUTION CODE	
Unclassified - Unlimited Subject Category 35			
This publication is available from the NASA Center for Aerospace Information, (301) 621-0390.			
13. ABSTRACT (Maximum 200 words)			
<p>A new instrument, the liquid crystal point diffraction-interferometer (LCPDI), has been developed for the measurement of phase objects. This instrument maintains the compact, robust design of Linnik's point diffraction interferometer (PDI) and adds to it phase stepping capability for quantitative interferogram analysis. The result is a compact, simple to align, environmentally insensitive interferometer capable of accurately measuring optical wavefronts with very high data density and with automated data reduction. This dissertation describes the theory of both the PDI and liquid crystal phase control. The design considerations for the LCPDI are presented, including manufacturing considerations. The operation and performance of the LCPDI are discussed, including sections regarding alignment, calibration, and amplitude modulation effects. The LCPDI is then demonstrated using two phase objects: defocus difference wavefront, and a temperature distribution across a heated chamber filled with silicone oil. The measured results are compared to theoretical or independently measured results and show excellent agreement. A computer simulation of the LCPDI was performed to verify the source of observed periodic phase measurement error. The error stems from intensity variations caused by dye molecules rotating within the liquid crystal layer. Methods are discussed for reducing this error. Algorithms are presented which reduce this error; they are also useful for any phase-stepping interferometer that has unwanted intensity fluctuations, such as those caused by unregulated lasers.</p>			
14. SUBJECT TERMS			15. NUMBER OF PAGES
Interferometry; Phase measurement; Phase stepping; Temperature measurement; Optical testing			109
			16. PRICE CODE
			A06
17. SECURITY CLASSIFICATION OF REPORT	18. SECURITY CLASSIFICATION OF THIS PAGE	19. SECURITY CLASSIFICATION OF ABSTRACT	20. LIMITATION OF ABSTRACT
Unclassified	Unclassified	Unclassified	

National Aeronautics and
Space Administration
Lewis Research Center
21000 Brookpark Rd.
Cleveland, OH 44135-3191

Official Business
Penalty for Private Use \$300

POSTMASTER: If Undeliverable — Do Not Return